Contact Mechanics and Adhesion of Polymeric Soft Matter Particles in Aqueous Environment

Dissertation

zur Erlanung des akademischen Grades eines

Doctor rerum naturalium

(Dr. rer. nat.)

Vorgelegt dem Bereich

Mathematik und Naturwissenschaften

der Technischen Universität Dresden

**TECHNISCHE
UNIVERSITÄT
DRESDEN**

von

M.Sc. Maximilian Seuß

geboren am 10.10.1988 in Hof

Eingereicht am 20.09.2019

Verteidigt am 19.12.2019

Gutachter: Prof. Dr. Andreas Fery

Prof. Dr. Brigitte Voit

Angefertigt unter der Betreuung von Prof. Dr. Andreas Fery

Am Leibniz-Institut für Polymerforschung Dresden e.V.

Wer es einmal soweit gebracht hat,

daß er nicht mehr irrt,

der hat auch zu arbeiten aufgehört.

Max Planck

Table of Contents

Summary

Polymeric materials, as they grow more and more indispensable for everyday life, can be highly sophisticated and specialized products. Successful design and production of polymeric materials with desired properties require concurrent experimental and theoretical foundations. Starting from the earliest application of natural polymeric substances by the ancient Egyptians and the Mayas, the first fully synthetic polymers and the introduction of the term "polymerization" was way later in the 19th century. Subsequently, the industrial production and profound scientific understanding of these polymeric materials gradually emerged in the early 20th century. Further, science has proved that the fundamental behavior of polymeric materials differs drastically from "hard", inorganic matter, hence the creation of the term "soft matter". The division of modern soft matter research is not only investigating physico-chemical aspects but also reaches into the field of biology, due to the highly complex macromolecular structures of peptides and enzymes. Macromolecules usually are not present as isolated chains; instead they form networks of many, similar chains or as part of complex entities. Simple examples are rubber abrasions of car tires or complex structured animal and plant cells. In the majority of the cases, environmental conditions such as temperature or the presence of water play a decisive role. Rubber abrasion is typically increased at higher temperatures but reduces on wet roads. Regarding cells, the temperature influences many biochemical processes, while no cell can survive without water. Furthermore, the interaction between macromolecules changes with varying environments, which is a key focus in both fundamental research as well as for real-life applications. Based on this background, this thesis aims to provide more insights into the contact mechanical and adhesive properties of polymeric soft matter particles in aqueous solutions. At this moment, expanding the toolbox of strategies to tailor the function of such particles will aid the rational design of new functional materials.

In this dissertation, I will present an overview of the synthetic methodologies to prepare hydrogel particles with sub-millimeter in size, which are mainly used throughout this work. Hydrogels are a very versatile class of materials made up of crosslinked polymer networks which are swollen by water. The amount of water can be as high as 99.9 % based on weight but can vary due to external stimuli. In chapter II.1.1, conventional approaches to prepare colloidal hydrogel particles using the technique of precipitation polymerization are discussed. I also commence on novel reactor designs, which gain more and more attention over the past decades. One of the most attractive alternatives is the utilization of

droplet microfluidics to form surfactant-stabilized droplets continuously in an organic phase. (see chapter II.1.2) The multi-phased co-axial microfluidic channels can bring high versatility in terms of choice and distribution of reactive agents. Such flow profiles are generally challenging or even impossible to fulfill with the conventional methods mentioned above. In case the aqueous phase contains reactive monomers or macromers the droplet can be gelled afterward forming well-defined microparticles. Besides the preparation of hydrogels, their application in sensors and actuators is presented in chapter II.2. This is a research area in which hydrogels are not yet used commercially but offer great potential. Another topic promising great perspectives, however being currently not available at large scales are underwater adhesives. In chapter II.3, the focus is mainly on elaborating on the ideas inspired by nature, based on the remarkable skills of mussels, sandcastle worms, and others.

Besides the huge variety of materials, their properties and capacities need to be precisely determined and thoroughly analyzed. A further challenge is the experimental analysis of tiny micro- and nanoparticles since conventional engineering approaches are not applicable. Here atomic force microscopy (AFM) has been established as the method of choice. It can detect very small distance-dependent forces locally with high precision. Additionally, AFM measurements can be carried out in various environments. The function and multiple possibilities of AFM are summarized in chapter III.1. To describe contact mechanical behavior, also taking into account adhesive interactions, a comprehensive overview of theories is provided in chapter III.2. Beginning with the widely used Hertz model, neglecting adhesive contributions, then the first theories including attractive adhesion by Johnson, Kendall, and Roberts, as well as by Derjaguin, Muller and Toporov, later expanding to more advanced concepts.

In the framework of this thesis, a study was conducted dealing with a strategy to change the mechanical properties of microgel particles using inwards-interweaving self-assembly post-synthesis. This technique was invented by my cooperation partners of the Trau group, and they prepared all particles studied. Exemplarily, agarose microparticles were used to interweave a defined shell of complexed poly(allylamine) (PA) and poly(styrenesulfonic acid) (PSS) into such particles. Thereby, the shell thickness can be well-defined. Adjusting the concentration of PA and the incubation time, the filling of the particles can be readily controlled up to complete filling. By adding excessive PSS, the diffusion-controlled shell formation stops by complexation. The shell thickness of

individual particles was determined through fluorescence-labeled PA and confocal laser scanning microscopy. The mechanical properties of single particles were inferred by AFM with an attached colloidal probe (CP). Here, a non-linear increase of the elastic modulus (E-modulus) from 10 to 190 kPa was determined while the shell thickness increased from 10 to 24 μm. After adding a second shell, a further gain to 520 kPa on average can be realized.

Furthermore, a new concept was developed by Mr. Fery and me to change the surface mechanical properties of mircogel particles by applying a thermal trigger. Meanwhile, a particular focus was laid to maintain constant adhesive properties at every temperature. First, crosslinked poly(*N*-isopropyl acrylamide) (PNIPAM) particles are prepared by droplet microfluidics. These gelled particles are injected into a second microfluidic device and surrounded by an aqueous solution of uncrosslinked poly(acrylamide) (PAAM). At a second junction, droplets are formed via the cut-off effect of the continuous organic solvent. The droplets now contain the crosslinked PNIPAM core and a thin uncrosslinked PAAM liquid shell. After a short diffusion of PAAM polymers into the core they are crosslinked by UV-light. These experiments were performed by our cooperation partners of the Seiffert group. I applied temperature-controlled CP-AFM to obtain the resulting adhesive and mechanical properties of individual particles. Here, the core-shell particles behaved similarly to plain PNIPAM particles displaying the typical increase in E-modulus at temperatures above 34°C, however lower in magnitude. Further, no temperature effect on the interfacial interaction for these core-shell particles was detected.

While one focus of the study above was on constant adhesion, in the following section, a new synthetic approach for mussel inspired underwater adhesives, and their characterization is presented. Based on a peptide sequence of ten amino acids, which is found frequently in natural mussel foot proteins, a new polymerization route was developed by my cooperation partners of the Börner group. Possible reaction pathways were investigated with specifically designed model reaction and analyzed using mass spectroscopy and gel permeation chromatography. The resulting polymers were further characterized using high-performance liquid chromatography and SDS-page. Nanometer thick coatings of these synthetic polymers revealed an excellent persistence even against highly concentrated salt solutions measured by quartz crystal microbalance with dissipation experiments. My contribution was the investigation of the work of adhesion necessary to

detach a microparticle from such a coating by CP-AFM in an aqueous environment. Here, the newly developed synthetic polymer provided higher adhesive strength, up to 10.9 mJ m^{-2}, compared to comparable natural mussel foot proteins.

Zusammenfassung

Polymere Materialien, wie sie aus unserem heutigen Leben nicht mehr weg zu denken sind, sind hoch technisierte und spezialisierte Produkte. Ein funktionales Design und eine erfolgreiche Herstellung solcher polymeren Materialien benötigt dabei eine fortwährende experimentelle und theoretische Grundlage. Beginnend mit der frühzeitlichen Verwendung von polymeren Stoffen durch die alten Ägypter oder die Mayas, über die ersten voll synthetischen Polymere und der Einführung des Terminus „Polymerisation" im 19. Jahrhundert. Das tiefergreifende wissenschaftliche Verständnis über Polymere belegte dann fundamentale Verhaltensunterschiede im Vergleich zu „harter", anorganischer Materie, weswegen der Begriff der „weichen" Materie eingeführt wurde. Dabei beschränkt sich der Forschungsbereich der weichen Materie nicht nur auf die chemisch-physikalischen Aspekte, sondern reicht auch in die Biologie, mit den hochkomplexen makromolekularen Strukturen von Peptiden und Enzymen. Makromoleküle liegen typsicher Weise nicht als isolierte Ketten vor, sondern als Partikel oder Netzwerke aus vielen, gleichartigen Ketten. Einfache Beispiele sind der Gummiabrieb von Autoreifen, aber auch komplex strukturierte tierische und pflanzliche Zellen. In beiden Fällen spielen Umgebungsparameter, wie Temperatur und die Präsenz von Wasser, eine wichtige Rolle. So wird der Gummiabrieb typischerweise durch hohe Temperaturen begünstig, jedoch auf feuchten Straßen reduziert. Bei Zellen beeinflusst die Temperatur viele biochemische Prozesse, wohingegen keine Zelle ohne Wasser überleben kann. Darüber hinaus verändern sich die Wechselwirkungs-eigenschaften der Makromoleküle mit ihrer Umgebung, was ein zentraler Fokus sowohl in der Forschung als auch der Applikation ist. Basierend auf diesem Hintergrund soll diese Arbeit weitere Einblicke in die kontaktmechanischen und adhäsiven Eigenschaften von polymeren Partikeln aus weicher Materie in wässriger Umgebung liefern. Dabei sollen neue Strategien entwickelt und getestete werden um die Funktion solcher Partikel maßschneidern zu können und deren rationalen Designmöglichkeiten zu erweitern.

Da sich das Augenmerk dieser Arbeit auf Submillimeter große Partikel richtet, wird zunächst ein Literaturüberblick über die Herstellungsmöglichkeiten von solchen Hydrogel-partikeln gegeben. (siehe Kapitel II.1) Hydrogele sind eine sehr vielseitige Materialklasse gebildet aus einem verzweigten Polymernetzwerk, welches durch Wasser gequollen wird. Dabei kann der Gewichtsanteil an Wasser bis zu 99,9% erreichen, sich aber auch induziert durch die Umgebung verändern. Beginnend mit der klassischen Fällungspolymerisation in

Kapitel II.1.1 wird anschließend die besonders vielversprechende Variante der Tropfen-mikrofluidik vorgestellt. Diese kann kontinuierlich, Tensid stabilisiert Wassertropfen in µm Größe in einer Ölphase erzeugen. (siehe Kapitel II.1.2) Beinhaltet die wässrige Phase reaktive Mono- oder Makromere, kann der Tropfen nachträglich zu Größendefinierten Mikrogelpartikeln geliert werden. Neben der Erzeugung, befasst sich Kapitel II.2 mit der Applikation von Hydrogelen in Sensoren und Aktuatoren, ein Bereich in dem Hydrogel noch selten Großindustrielle verwendet werden. Ein anderes Gebiet, welches hohes Anwendungspotenzial verspricht sind Unterwasser Klebstoffe. Die Forschung und Entwicklung befasst dabei schwerpunktartig mit biologisch inspirierten Konzepten, in Anlehnung an die beindruckenden Fähigkeiten von Muscheln, des Sandburg-Wurms und anderen. (siehe Kapitel II.3)

Nebst den vielfältigen Möglichkeiten der Materialwahl, müssen auch deren Eigenschaften und Leistungsfähigkeit präzise bestimmt und solide analysiert werden. Eine weitere Herausforderung stellt eine solche experimentelle Analyse für extrem kleine Mikro- und Nanopartikel dar, da gängige, ingenieurwissenschaftliche Methoden nicht mehr anwendbar sind. Hierfür hat sich die Rasterkraftmikroskopie (engl. AFM) etabliert, welche sehr geringe, abstandsabhängige Kräfte lokal und hochaufgelöst detektieren kann und unter diversen Umgebungsparametern betrieben werden kann. Ein Überblick zur Funktionsweise und Möglichkeiten ist in Kapitel III.1 zusammengefasst. Zur Beschreibung des kontaktmechanischen Verhaltens, auch unter Berücksichtigung von adhäsiven Wechselwirkungen, bietet Kapitel III.2 einen umfassenden theoretischen Überblick. Von dem am weitesten verbreiteten Hertz Model, welches noch Adhäsion vernachlässigt, über die ersten Theorien inklusive attraktiver Kräfte von Johnson, Kendall und Roberts bis hin zu moderneren Beschreibungsansätzen.

Im Rahmen dieser Arbeit, wurde eine Studie durchgeführt, welche die Möglichkeiten der nachträglichen Elastizitätsveränderung von Mikrogelpartikeln mittels „nach Innen gerichteter, verwebender Selbstassemblierung" (engl. inwards-interweaving self-assembly) beleuchtet. Diese Technik wurde von meinen Kooperationspartnern aus der Gruppe von Herrn Trau entwickelt. Am Bespiel von Agarose Mikropartikeln, kann mittels dieser Technik eine definierte Schale aus Polyallylamin (PA) und Polystyrolsulfonsäure (PSS) in das Partikel verwoben werden. Die Schalendicke kann dabei kontrolliert variiert werden, bis hin zur vollständigen Ausfüllung des Partikels, in dem die Konzentration von PA und die Inkubationszeit angepasst werden. Durch Zugabe eines Überschusses an PSS

wird der diffusionsgesteuerte Schalenaufbau durch Komplexierung beendet. Die Schalendicke der individuellen Partikel wurde mittels Fluoreszenzmarkierung und konfokaler Laser Rastermikroskopie (engl. confocal laser scanning microscopy) ermittelt. Die mechanische Charakterisierung einzelner Partikel durch AFM und kolloidaler Sonde (engl. colloidal probe, CP) ergab eine nicht lineare Erhöhung des Elastizitätsmoduls (E-Modul) von 10 auf 190 kPa bei einem Schalendicken Zuwachs von 10 auf 24 µm. Durch eine zweite Schale, in der Ersten, konnte der E-Modul auf im Mittel 520 kPa gesteigert werden.

Weiterführend, wurde von mir und Herrn Fery ein neues Konzept entwickelt, um eine mechanische, oberflächliche Verhärtung von Mikrogelpartikel durch Temperaturveränderung zu induzieren mit einem Augenmerk, dass sich die Adhäsionseigenschaften nicht verändern. Zunächst wurden von meinen Kooperationspartnern aus der Gruppe von Herrn Seiffert vernetzte Poly-*N*-isopropylacrylamid (PNIPAM) Partikel mittels Tropfenmikrofluidik hergestellt. In einem zweiten Mikrofluidik Experiment wurde diese Partikel mit einer wässrigen Lösung von Polyacrylamid (PAAM, unvernetzt) umgeben bevor es zu einer Tropfenbildung in der organischen Phase kommt. Nach kurzer Diffusionszeit der PAAM Polymerketten in die Kernpartikel, wurde die PAAM Schale mittels UV-Licht quervernetzt. In temperaturkontrollierten CP-AFM Untersuchungen habe ich die resultierenden Adhäsions- und mechanischen Eigenschaften auf der Einzelpartikel Ebene bestimmt. Hierbei konnte bei den Kern-Schale Partikeln der für bloße PNIPAM Partikel typische E-Modul anstieg oberhalb von 34°C nachgewiesen werden, jedoch mit verminderten Absolutwerten. Eine begleitende Veränderung der adhäsiven Eigenschaften der Kern-Schale Partikel konnte dabei nicht beobachtet werden.

Lag ein Fokus der vorherigen Arbeit auf konstanten Wechselwirkungen, behandelt der dritte Teil der Ergebnisse, einen neuen Synthese Ansatz zur Herstellung Muschel inspirierter Unterwasser Adhäsiva und deren Charakterisierung. Basierend auf einer natürlichen Peptidsequenz, wurde eine enzymatische Polymerisationsroute von meinen Kooperationspartner aus der Börner Gruppe entwickelt. Der Reaktionsverlauf wurde durch neu designte Modelreaktion untersucht und mittels Massenspektroskopie und GPC analysiert, das resultierende Polymer zusätzlich mit HPLC und SDS-page. Nanometer dicke Beschichtungen dieser Muschel inspirierten Polymer wiesen eine sehr gute Beständigkeit gegen hoch konzentrierten Salzlösung in QCM-D Experimenten auf. Die Adhäsionsarbeit, welche nötig ist um eine Mikropartikel von diesen in wässeriger Lösung zu entfernen, wurde von mir

mittels CP-AFM bestimmt. Nach meiner Erweiterung einer bekannten Adhäsionstheorie, konnten für das synthetische Polymer höhere Werte als für vergleichbare Natürliche von bis zu 10.9 mJ m^{-2} bestimmt werden.

List of Publications

1. H. M. Pan, **M. Seuss**, M. P. Neubauer, D. W. Trau, A. Fery; *Tuning the Mechanical Properties of Hydrogel Core-Shell Particles by Inwards Interweaving Self-Assembly*, ACS Applied Materials & Interfaces, **2016**, 8, 1493-1500

2. **M. Seuss**, W. Schmolke, A. Drechsler, A. Fery, S. Seiffert, *Core-Shell Microgels with Switchable Elasticity at Constant Interfacial Interaction*, ACS Applied Materials & Interfaces, **2016**, 8, 16317 – 16327

3. J. Horsch, P. Wilke, M. Pretzler, **M. Seuss**, I. Melnyk, D. Remmler, A. Fery, A. Rompel, H. G. Börner, *Polymerizing like the mussels do: Toward synthetic mussel-foot proteins and resistant glues*, Angewandte Chemie International Edtion, **2018**, 130, 15954-15958

Further publications:

1. M. Poehlmann, D. Grishenkov, S. V. V. N. Kothapalli, J. Härmark, H. Herbert, A. Philipp, R. Hoeller, **M. Seuss**, C. Kuttner, S. Margheritelli, G. Paradossi, A. Fery, *On the interplay of shell structure with low- and high-frequency mechanics of multifunctional magnetic microbubbles*, Soft Matter, **2014**, 10, 214

2. L. Peng, S. Jiang, **M. Seuss**, A. Fery, G. Lang, T. Scheibel, S. Agarwal, *Two-in-One Composite Fibers With Side-by-Side Arrangement of Silk Fibroin and Poly(L-lactide) by Electrospinning*, Macromolecular Materials and Engineering, **2016**, 301, 48-55

3. M. Stöter, S. Gödrich, P. Feicht, S. Rosenfeldt, H. Thurn, J. W. Neubauer, **M. Seuss**, P. Lindner, H. Kalo, M. Möller, A. Fery, S. Förster, G. Papastavrou, J. Breu, *Controlled Exfoliation of Layered Silicate Heterostructures into Bilayers and Their Conversion into Giant Janus Platelets*, Angewandte Chemie International Edition, **2016**, 55, 7398 - 7402

4. T. Heida, J. W. Neubauer, **M. Seuss**, N. Hauck, J. Thiele, A. Fery, *Mechanically Defined Microgels by Droplet Microfluidics*, Macromolecular Chemistry and Physics, **2017**, 218, 1600418

5. P. Feicht, R. Siegel, H. Thurn, J. W. Neubauer, **M. Seuss**, T. Szabó, A. V. Talyzin, C. E. Halbig, S. Eigler, D. A. Kunz, A. Fery, G. Papastavrou, J.

Senker, J Breu, *Systematic evaluation of different types of graphene oxide in respect to variations in their in-plane modulus*, Carbon, **2017**, 114, 700-705

6. A. M. Steiner, M. Mayer, **M. Seuss**, S. Nikolov, K. D. Harris, A. Alexeev, C. Kuttner, T. A. F. König, A. Fery, *Macroscopic Strain-Induced Transition from Quasi-infinite Gold Nanoparticle Chains to Defined Plasmonic Oligomers*, ACS Nano, **2017**, 11, 8871 – 8880

7. **M. Seuss**, A. Fery, *AFM-Force-Curve-Analyzer-IgorPRO*, 10.5281/zenodo.1208549 , **2018**

8. J. W. Neubauer, N. Hauck, M. J. Männel, **M. Seuss**, A. Fery, J. Thiele, *Mechanoresponsive Hydrogel Particles as a Platform for Three-Dimensional Force Sensing*, ACS Applied Materials & Interfaces, **2019**, 11, 26307-26313

Glossary

ν	Poisson's Ratio
AA	acrylic acid
AFM	atomic force microscope/-scopy
APS	ammonium persulfate
BIS	N,N'-methylenebis(acrylamide)
Ca	capillary number
CCD	charge-coupled device
CLSM	confocal laser scanning microscopy
COS	Carpick, Ogletree, Salmeron
CP-AFM	colloidal probe – atomic force microscopy
CP	colloidal probe
DMMIAAm	N-(2-(3,4-dimethyl-2,5-dioxo-2,5-dihydro-1H-pyrrol-1-yl)ethyl)acrylamide
DMSO	dimethyl sulfoxide
DMT	Derjaguin, Muller, Toporov
DOPA	3,4-dihydroxyphenylalanine
DSS	disuccinimidyl suberate
DVB	divinyl benzene
E	elastic modulus
ESI	electron-spray ionization
ESI-LC-MS/MS	electron-spray ionization liquid chromatography mass spectrometry
F	force; vertical load force
F-D	force – deformation curves
FEM	finite element methodes
FITC	fluorescein isothiocyanate
GPC	gel permeation chromatography
HPLC	high-performance liquid chromatography

HRMS	high-resolution mass spectroscopy
InvOLS	inverse optical lever sensitivity
JKR	Johnson-Kendall-Roberts
KPS	potassium persulfate
LbL	layer-by-layer
LCST	lower critical solution temperature
MALDI-TOF-MS	matrix-assisted-laser desorption/ionization time of flight mass spectroscopy
mfp	mussel foot protein
NIPAM/NiPAAm	N-isopropyl arclyamide
NMR	nuclear magnetic resonance
PA	poly(allylamine)
PAA	poly(acrylic acid)
pAAm	poly(acryl amide)
PAH	poly(allylamine hydrochloride)
PBS	phosphate-buffered saline
PDADMAC	poly(dimethyl diallyl ammonium chloride)
PDMS	poly(dimethyl siloxane)
PEI	poly(ethylene imine)
PGA	poly(glycolic acid)
PLL	poly(L-lysine)
PMMA	poly(methyl methacrylate)
pNiPAAm/PNIPAM	poly(N-isopropyl acrylamide)
PPO	polyphenol oxidase
PSS	poly(styrene sulfonate)
PSSA	Poly(4-styrenesulfonic acid)
PVA	poly(vinyl alcohol)
PVCL	poly(N-vinylcaprolactam)

R,r	radius
QCM-D	quartz crystal microbalance dissipation
QI	quantitative imaging
QNM	quantitative Nanomechanical
$Ru(bpy)_3^{2+}$	ruthenium(II) tris(2,2'-bipyridine)
SDS	sodium dodecyl sulfate
SEM	scanning electron microscopy
SFA	surface force apparatus
Span 80	sorbitan monooleate
STM	scanning tunneling microscope
T	temperature
TEM	transmission electron microscopy
TEMED	N,N,N',N'-tetramethyl ethylene diamine
TMS	trimethylsilane
TRiTC	tetramethylrhodamine isothiocyanate
TXS	thioxanthone-2,7-disulfonate
UV	ultra violet
We	Weber number

List of Figures

I. Introduction

I.1. Motivation

"The real point of honor for a scientist is not to be always right. It is to dare to propose new ideas, and then to check them."[1] An inspiring quote from Pierre-Gilles de Gennes addressing young researches to ask questions, which may appear to be out of the box, but inherently path the way for something new. Living up this quote himself, he raised plenty of questions in the area of polymer physics and is considered one of the founding fathers of soft matter physics. Soft matter refers to materials with structural features much larger than atoms, organized on the mesoscopic length scale, but smaller than the overall size of the content.[2] These arrangements are formed by relatively weak interactions, giving rise to unique response behavior towards thermal fluctuations, external stimuli, and slow responses with long relaxation times. Many materials represent these aspects surrounding us in everyday life. Ranging from granular matter and liquid crystals over surfactants, foams, and emulsions to gels and polymers in general, but also including many biological materials.[3] With these sheer endless examples of soft matter materials one can find in nature or are manmade, I asked myself: what is the role of contact mechanics and adhesion for polymeric soft matter microparticles in aqueous environments?

First of all, thinking about mechanical properties, the word *soft* can be misleading. Polymeric working materials can be extremely tough. They are used, for example as window frames and roofing tiles withstanding immense forces without breaking. Of course, there are also soft, flexible, compliant representatives like household rubbers or contact lenses. This elastic variability of soft matter materials ranging from some Pa to GPa in elastic modulus renders them extremely adjustable for highly specific tasks in life and nature. Their counterpart, crystalline inorganic materials, are equally vital in many aspects but their flexibility in elastic properties is typically limited to the range from low GPa to 100s of GPa.[4] This is raising the question, which strategies are available to tune the elastic properties to match specific application requirements?

Secondly, size, shape, and structure always affect physical response properties in general. From the mechanical point of view, they dictate the net forces the object can withstand. One can easily break a wooden toothpick with one hand but not a trunk. However, the smaller the object is the bigger its surface area to volume ratio gets. This

benefits exchange processes between the object and its surroundings by diffusion of solvent or cargo but also the transport of heat. Further, the morphology can introduce more features to a material. From homogeneous, isotropic spheres to anisotropic rods or disks. Moreover, further to inclusions of other materials in a core-shell arrangement or with distinct, two-sided separation in Janus-like objects. Can we tailor the object's size and morphology to support the intended mechanical properties and introduce more function on the micro- and nano-scale?

Next, all properties are, of course, inherent to materials, but they are as well critically affected by their surrounding medium. Besides fundamental, molecular studies typically performed in vacuum, most practical investigations are conducted in air or water. Water is likely the most exciting molecule on earth since it is essential for life in general but also of industrial interest as reaction solvent, carrier medium or for cooling purposes. In the context of soft matter materials, water will always affect the surface properties, but additionally, it can be a good solvent for many polymeric substances. Objects constituting of crosslinked polymers and water are referred to as hydrogels with water contents of up to 99.9 % by weight[5], which are in turn responsive to changes in the environmental conditions. Is it possible to introduce adaptive features by intelligent selection of responsive polymers in areas of interest?

Finally, most applications do not only focus on isolated objects floating around in water but rather on how they interact with other objects and interfaces. While physics can describe the magnitude of different interaction potentials, adhesive properties are an ever-present issue once contact has been established. For fixation purposes, it is desirable to maintain durable and robust adhesion while for self-cleaning coatings on windows one aims for increased repellence of water and dust. While electrostatic interactions typically dominate repellence, adhesion can be furthermore promoted by physical bonds like hydrogen bonds, entanglements, depletion forces, and others. How can we prevent unfavorable adhesion or promote it even under complicated environmental conditions?

By raising these four questions at the end of the sections above I want to "dare to propose new ideas" in the field of polymeric soft matter microparticles "and then to check on them" regarding their influence on mechanical and adhesion properties.

I.2.   Objective of the Thesis

The research area of polymeric soft matter and especially of hydrogel materials is a very well established one also starting to spread in the field of biology from the 1960s on.[6, 7] Till now, there are countless variations of hydrogels addressing biocompatibility, permeability, swellability, sizes and shapes, network architectures, response behavior, and more.[5, 8] In many cases it is convenient to prepare and test new materials at the macroscopic scale for the ease of analytics but as well since the application demands it. On the contrary, this requires an increased amount of content, is less sensitive to local changes and analytics as well as function is typically accompanied by very long equilibration and response times.

One motivation of this thesis is to circumvent these issues by focusing on micrometer-sized objects while they maintain convenience for the investigations of contact mechanical and adhesion properties compared to nanoparticles. With such dimensions, they can be imaged by optical microscopy techniques, as will be demonstrated by bright field illumination, fluorescence, and confocal laser scanning microscopy on the single-particle level in chapters V and VI. Besides plain visualization, changes of the whole particles or compartments of them can be followed in situ. Unfortunately, the small size disqualifies standard macroscopic techniques for mechanical (tensile test) and adhesion investigations (peeling test). However, the capabilities of modern atomic force microscopes (AFM) provide the possibility of applying and detecting small forces precisely and locally determining both mechanics and interactions simultaneously, as theoretically explained in chapter III.1 and used in all presented new studies. Quantification of these properties, especially on the material level, can be rather tedious since size and shape affect the measurements and need to be accounted for in post-processing. Depending on the material and the experimental conditions, various contact mechanical theories may be suitable. The most important ones are presented in chapter III.2. However, they are not comprehensive. Hence I developed a new theoretical model for multiple adhesive failure events, as detailed in chapter VII.2.3.

The second object of this thesis is to extend the spectrum of pathways to affect the mechanical properties of polymeric soft matter particles. In situations where the mechanical resilience of materials needs to be adjusted, classical approaches involve the change of polymeric network structure by varying the number of covalent crosslinks during preparation. While the overall amount of crosslinking agents is precisely controllable its

homogeneous incorporation in every particle is almost impossible. Another and potentially more flexible approach involves precise post modification of existing particles by physical crosslinkers. Here, my cooperation partners showed with the so-called inwards-interweaving self-assembly technique that it is possible to manufacture highly center symmetric core-shell agarose beads. While they explored in earlier studies the flexibility of this approach and the diffusion related effects of the shell build-up, the adjacent mechanical consequences are tested within this thesis. Thereby, the questions of possible strategies to tune the elastic properties of polymeric soft matter particles as well as tailoring the morphology to introduce more functionality are addressed. (see chapter V)

To additionally include the last two questions of adaptive response behavior and controlled adhesion, a yet different strategy can be followed by incorporating active moieties within the object, which are triggered by a stimulus. A general approach involves responsive polymers that change their solvent interaction and eventually their degree of swelling. The later has, obviously, a direct influence on the mechanical response behavior and both, solvent interaction and swelling degree, typically affect the adhesive interaction properties. One objective of this thesis is to define a way for decoupling both phenomena. Decoupling should aid the variability of such materials in a rational and designable manner. Our concept aims at shielding the adhesive changes of the active part by encapsulation with chemically similar but non-responsive material. Provided there is a mechanical connection between core and shell, the elastic properties of the shell material can be affected even up to the very surface. This concept was employed, tested, and verified on micrometer-sized hydrogel particles, all presented in chapter VI.

While controllable adhesion in aqueous media is of importance for many applications, there is also a big desire for high performance underwater adhesive formulations. Binding strategies applied for common glues typically rely on dry environments while curing. Such cured splices can be very stable in aqueous media. However, it is not applicable to every situation, e.g. in deep-sea research, shipping, medical wound dressing, or surgery. Inspired by the impressive capabilities of mussels to adhere to various types of surfaces, especially under complex environmental conditions, a broad research interest developed in understanding, replicating and adapting the underlying processes. Focusing on the fourth question of promoting adhesion, our contribution here lies in developing a simplified synthetical approach to produce the underlying adhesives proteins while using building blocks and synthesis routes theoretically available for the

mussels themselves. Therefore, my cooperation partner of the Börner group established an enzyme-mediated polymerization reaction of macromonomers, constituting of a decapeptide sequence of amino acids also present in natural mussels. The complete discussion on the polymerization pathways and results, the coating capabilities, and adhesive properties of these artificial mussel glues under various conditions are given in chapter VII.

I.3.   References

[1] P.-G. de Gennes, *Science et Vie Junior* **2007**, 13.

[2] S. R. Nagel, *Reviews of Modern Physics* **2017**, *89*, 025002.

[3] J. van der Gucht, *Frontiers in Physics* **2018**, *6*.

[4] M. de Jong, W. Chen, T. Angsten, A. Jain, R. Notestine, A. Gamst, M. Sluiter, C. Krishna
    Ande, S. van der Zwaag, J. J. Plata, C. Toher, S. Curtarolo, G. Ceder, K. A. Persson,
    M. Asta, *Scientific Data* **2015**, *2*, 150009.

[5] M. J. Majcher, T. Hoare, *Functional Biopolymers* **2018**, 1.

[6] O. Wichterle, D. Lím, *Nature* **1960**, *185*, 117.

[7] S. J. Buwalda, K. W. M. Boere, P. J. Dijkstra, J. Feijen, T. Vermonden, W. E. Hennink,
    Journal of Controlled Release **2014**, *190*, 254.

[8] M. Karg, A. Pich, T. Hellweg, T. Hoare, L. A. Lyon, J. J. Crassous, D. Suzuki, R. A.
    Gumerov, S. Schneider, I. I. Potemkin, W. Richtering, *Langmuir* **2019**, *35*, 6231.

II. Status of the Field

II.1. Hydrogel Preparation Techniques on the Micro- and Nanoscale

Over the years, classical polymer chemistry methods were further developed to fulfill material demands but also new reaction schemes from organic and biochemistry were introduced to hydrogel preparation. A hydrogel is defined as a "non-fluid colloidal network or polymer network that is expanded throughout its whole volume by" water.[9] This chapter first reviews the syntheses methods used to prepare nano and microgel particles with a certain weighting to connected applications. Secondly, a focus is placed on droplet-based microfluidics with its great potential in fundamental as well as applied research.

II.1.1. Synthetic Methods for Nano- & Micro Gels

Preparing hydrogel particles with sizes in the nano to micrometer range the classical approach is to use precipitation polymerization. Here the monomer is well soluble in the present solvent, but the resulting polymer is solvophobic and precipitates.[10] Alternatively, a second precipitation solvent is added at some point to induce the polymer precipitation. The molecular weight and particle size are adjustable by variation of the monomer to initiator ratio as well as by adding amphiphilic dispersant.[11] Besides the inherent self-crosslinking in free radical polymerization, additional crosslinking molecules are often added to adjust the degree of network knots in the final gel.[12]

One of the most popular colloidal hydrogels synthesized by precipitation polymerization is PNIPAM. In the original publication, NIPAM is solely mixed with *N,N'*-methylenebis(acrylamide) (BIS) and the thermos-initiator potassium persulfate (KPS) in water.[13] In their study, Majcher and Hoare explored the influence of monomer, comonomer (acrylamide) and initiator concentration as well as reaction temperature on the polymerization. KPS is typically activated at around 70°C, which also facilitates the precipitation of the growing PNIPAM macromolecules since the lower critical solution temperature (LCST) is lower than the reaction temperature. The resulting hydrogel particles were in the size range of 1 μm in the dried state, but they did not further investigate size dependencies.[13] In a recent project, Virtanen et al. proceeded to aim at scaling law dependency to predict the particle volume. They found that the dry particle volume scales with the initial monomer concentration by the power of 5/3 multiplied with the initiator concentration by the power of -4/3. This scaling law was experimentally supported in an
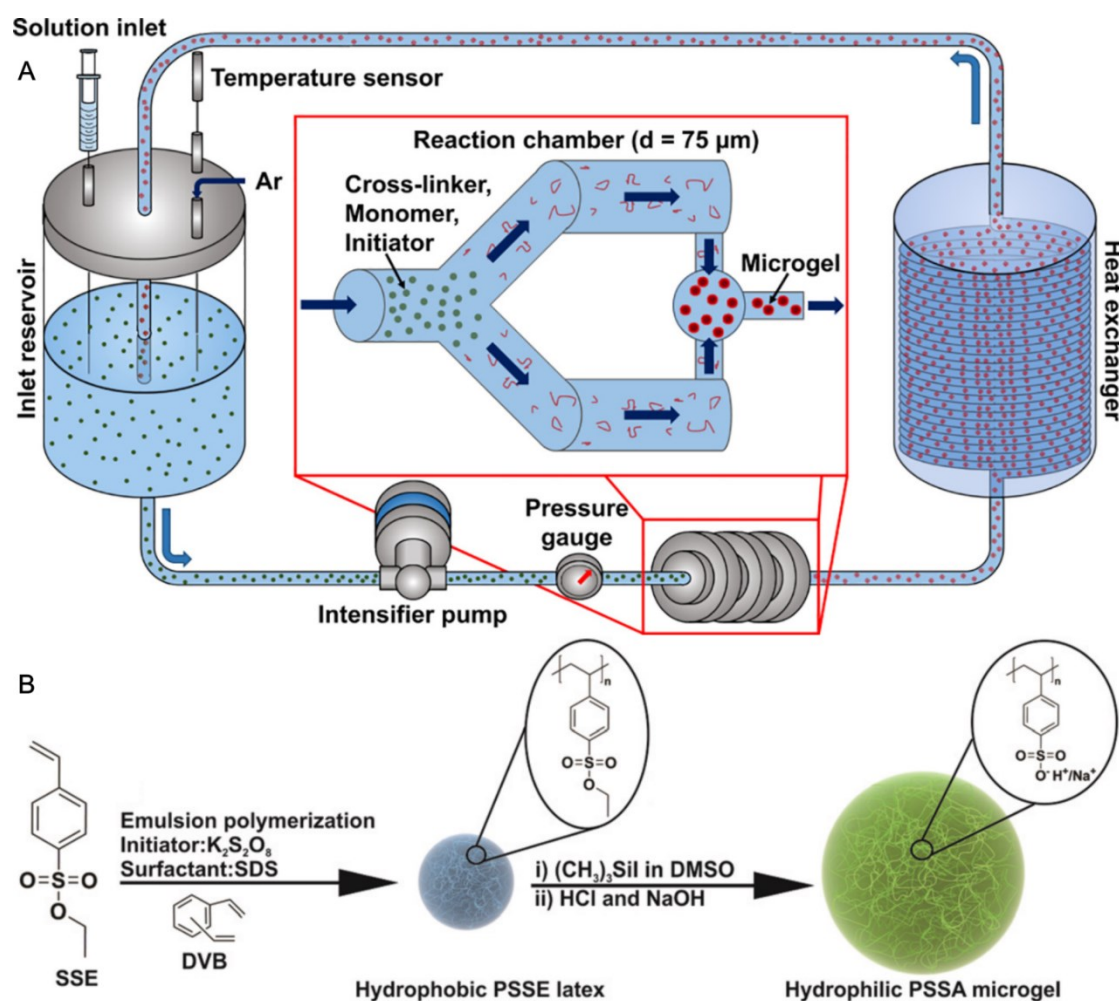
Figure 1 A) Experimental setup of the confined impinging jet reactor for the precipitation polymerization of PVCL microgels. Reprinted with permission.[14] Copyright 2018 Elsevier. B) Synthesis rout of PSSA microgels by first crosslinking ethyl ester protected PSSA in emulsion polymerization followed by deprotection, charging, and swelling. Reprinted with permission.[15] Copyright 2015 Royal Society of Chemistry.

extensive series of syntheses resulting in particles with hydrodynamic radii in between 60 and 180 nm.[12]

Nanogel particles are also an interesting prospect as carrier systems for biomedical applications using their responsive behavior to selectively release their load or drugs.[14, 16, 17] Here particle sizes of 100 nm or even below 50 nm are desirable but also potentially toxic chemicals, as certain surfactants, should be avoided or thoroughly cleaned. Addressing these issues, Kather et al. presented a new surfactant-free synthesis strategy producing almost monodisperse poly(*N*-vinylcaprolactam) (PVCL) particles as small as 45 nm.[14] They employed a so-called confined impinging jet reactor, depicted in Figure 1 A, which exerts up to 1200 bar pressure to the monomer/crosslinker solution in the reaction chamber and cycles the reaction solution after heat exchange through the reactor multiple times. The high pressure leads to increased Reynolds numbers (38000), shear rates

(8.5 ms^{-1}), and a better intermixing of the reactants compared to classical stirring reactors. The authors argue, that this suppresses aggregation of growing polymer chains and the formation of smaller precursor particles at the beginning of the reaction which finally results in small, monodisperse and temperature response PVCL nanogels.[14]

The presented approach of precipitation polymerization is of course not feasible anymore if the resulting polymer or polymer network is well soluble in the reaction solvent. Some amounts of respective monomers, e.g., weak polyelectrolyte forming acrylic acid, can be incorporated as comonomers in microgels.[18] To access microgel particles form permanently charged monomers is more complicated and for such materials, emulsion polymerization is a well-suited technique. Here the surfactant stabilized emulsion droplets serve as the particle templates.[10] By adjusting the surfactant concentration the particle size is tunable while the ratio of crosslinker to initiator to monomer is independent of that. Tiwari et al. applied emulsion polymerization to achieve homo microgel particles of poly(styrene sulfonic acid) (pSSA), which is a highly charged strong polyelectrolyte.[15] A synthesis scheme is depicted in Figure 1 B. They polymerized the ethyl ester protected styrene sulfonic acid with potassium peroxodisulfate (initiator), divinyl benzene (DVB, crosslinker) and sodium dodecyl sulfate (SDS, surfactant). The sulfonic acid groups were deprotected by employing iodotrimethylsilane and subsequent acidic hydrolysis. The particle size could be varied between 55 nm (2 mM SDS) and 90 nm (0.1 mM SDS) while the particle size stays constant while only changing the DVB amount.[15]

II.1.2. Droplet-based Microfluidic

The term microfluidic refers in general to study and application of liquids (but also gas) in channels with sizes in the micrometer range. For details about preparation, designs, limitations and handling the reader is referred to these and other reviews about this topic.[19-21] The adjacent handling of small volumes of liquid down to the fL scale impairs a relative dominance of inertial forces over viscous one - the ratio of both is defined as Reynolds number- significant surface force effects, and more efficient mass-heat transfer compared to macroscopic fluids. Designing the microchannel track with different junctions, barriers, and valves the flow pattern can be manipulated and adjusted to a specific task. Examples include sorting of small, dissolved objects within the gradient flow pattern of a straight channel by inertia forces and their subsequent lateral off branching in small channels.[22] Furthermore, microfluidic can aid analytics of diffusion-limited processes where intermediate conditions are accessible by the distance along the channel length[23] or in

mechanical analysis of cells by their shape changes while being squeezed through a smaller diameter microchannel.[24]

The subcategory droplet microfluidics generates and manipulates small, discrete droplets of two or more immiscible fluid phases. The dispersed droplets are typically stabilized in the continuous phase by surfactants which are not necessary for the droplet formation but essential for reliable transport prohibiting droplet coalescence and phase separation.[25] Droplet formation, without additional external trigger, is classically achieved either by co-flow, cross-flow, or flow focusing as depicted in Figure 2. In co-flow, both fluids flow in parallel while the disperse phase is until some point separated (in Figure 2 A by a capillary) from the continuous phase. When in contact, the interplay between viscous, inertia, and interfacial forces determine droplet formation or jetting. The top two images in Figure 2 A show a regime dominated by interfacial forces rather than by viscous forces – the ratio of viscous to interfacial forces is called capillary number Ca – and droplets form close to the capillary. Increasing the velocity of the continuous phase increases the viscous drag on the disperse phase, i.e. Ca increases, a jet is formed, thins out until interfacial forces induce droplet formation. In case the velocity of the disperse fluid is higher inertia forces dominate over interfacial forces – the ratio is referred to as Weber number We – it is called the wide jetting regime as depicted in the bottom image of Figure 2A.[26]

In a T-junction, the two phases flow at a 90° angle, as depicted in Figure 2 B, and droplet formation in such a cross-flow pattern is found to be dependent on the Ca number. At low Ca, i.e. low water flow velocities, the disperse fluid blocks the junction, the pressure increases, and a droplet is formed directly at the intersection. (see left inset in the plot of Figure 2 B) Increasing Ca the shears forces prevent the blocking of the junction by dragging the disperse fluid further in the channel. A neck is formed and finally the droplet breaks up, as depicted in the upper right inset of the graph in Figure 2 B.[19, 30] In the third regime, the flow velocity of the continuous phase is much higher than the disperse flow which leads to parallel flow after the junction, as depicted in the lower right inset of Figure 2 B's graph. Further down the channel, the jetting gets instable and droplets separate.[19]

The third principle of droplet formation is flow-focusing, the coaxial flow of both fluids through a constriction leading to shear-focusing of the disperse phase and an eventual droplet pinch-off. In this setup four distinct regimes are achievable: "geometry-controlled breakup", thread formation, jetting and dripping as depicted on the right hand of Figure 2 C clockwise starting on the top left. Similar to the cross-flow setup, the regimes are
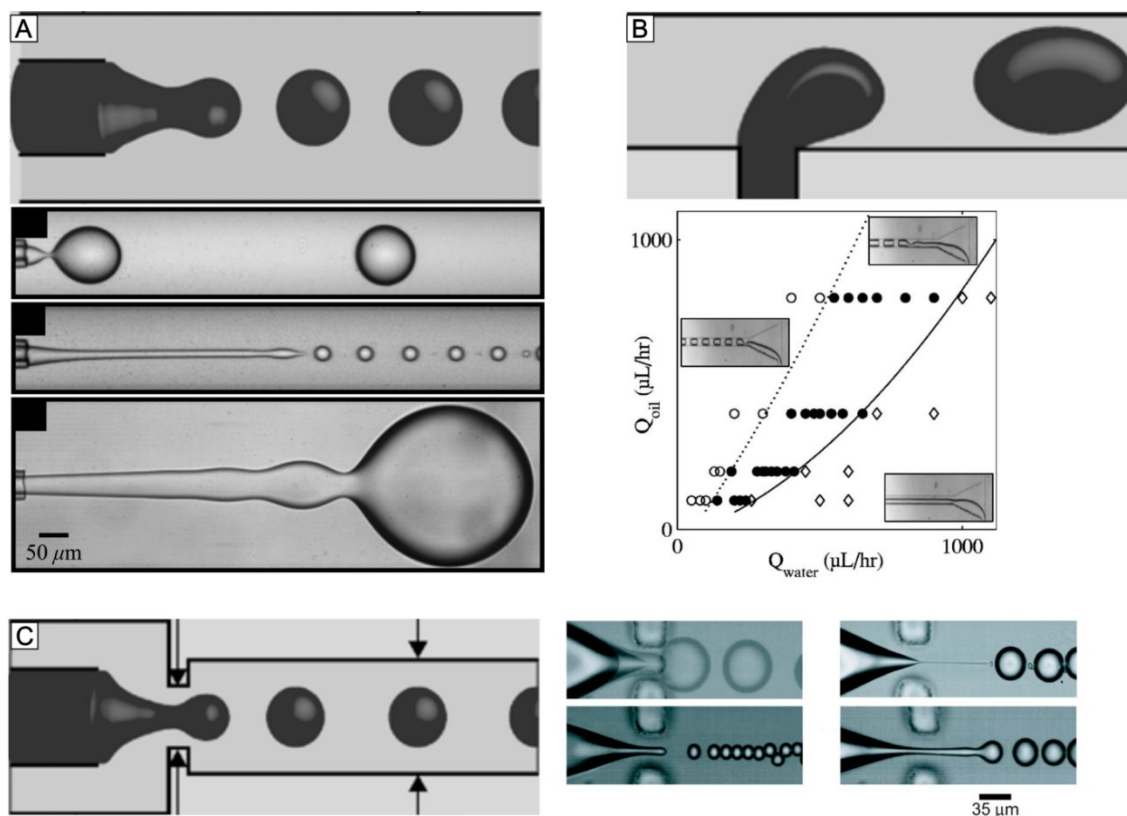
Figure 2 A) Top micrograph shows co-flow preparation of colored microdroplets. The top figure is not to scale. Three images below represent the dripping, narrow jetting, and wide jetting regime in co-flow. Reprinted with permission.[26] Copyright 2007 American Physical Society. B) Top micrograph displays an example of cross-flow in a T-junction. The graph below depicts a flow pattern diagram relating the liquid's flow velocities with droplet formation at the junction (open circles), without droplet formation in parallel flow (open diamonds) and with droplet formation after parallel flow (closed circles). Reprinted with permission.[27] Copyright 2005 American Physical Society. C) Left micrograph shows an example of droplet formation with flow focusing in a bottleneck. The four images on the right side show clockwise (starting at 10) the geometry controlled breakup, the thread formation, the jetting, and the dripping regime. Reprinted with permission.[28] Copyright 2006 AIP Publishing. Top figures in A, B, and C are reprinted with permission.[29] Copyright 2007 IOP Publishing.

connected through the *Ca* number beginning with a geometry-controlled breakup at low values. Increasing *Ca* reduces the size of "disperse phase finger" resulting in dripping or at even higher *Ca* in jetting. The thread formation is a special intermediate scenario between geometry-controlled and dripping where, in the presence of specific surfactant concentration, a thin thread of disperse fluid is preceding the creation of big geometry-controlled droplet.[28]

To synthesize monodisperse and reproducible hydrogel microparticles with this technique the disperse phase is water-based and contains the hydrogel precursor, either monomers or uncrosslinked polymers, and curing agents, such as polymerization initiators, crosslinkers or reactive side groups. Intrinsically, there is no limitation of transferring established bulk synthesis protocols to droplet-based microfluidics. However, an issue arising with chemical reactions in microfluidic droplets can be insufficient mixing. To

overcome diffusion-controlled mixing active[31] as well as passive mixers[32], a famous representative is a meander like channel[33], can be incorporated in the channel structure. Additionally, the choice of a suitable combination of the continuous phase, typically hydrocarbon or fluorocarbon oils, and the surfactant is important during preparation but also their removal to avoid contaminations in applications.[25]

II.2.   Hydrogels in Sensors and Actuators

The functionality and responsiveness of different hydrogel systems described above were characterized by physico-chemical methods. This chapter now focuses on the application of stimuli-responsive hydrogels as reacting elements in sensors and as acting or regulating elements in actuators.[19]

II.2.1. Sensors

For applications of hydrogels in a sensor system, the crucial part is the transduction of a response to a detectable and recordable signal. In many cases, the swelling degree is not observed directly due to its poor accessibility. Instead, its effect on other components of the sensor is monitored.

A well-known sensor design in electronic engineering is the 'bending-plate-based sensor'. When a thin piezoresistive plate - fixed on all edges - gets bent its electrical resistance changes and can be recorded in a Wheatstone bridge configuration. By either confining a hydrogel below or directly attaching it to the plate a change of swelling due to an analyte solution will deflect the plate and the response is transduced to an electrical signal.[34, 35]

One of the first reports realizing a hydrogel-based bending-plate sensor chip was published by Gerlach and coworkers.[34, 35] They experimented with two different sensor concepts to design a pH and an alcohol sensor. For the pH sensor, they used a poly(vinyl alcohol)/poly(acrylic acid) hydrogel with a weight ratio of 4:1, which was further deposited on the backside of the piezoresistive plate resulting in a hydrogel layer with a thickness of 5 to 50 μm. The responsiveness of the blend originates from the pH-dependent dissociation of the acid groups below the pK_a (= 4.7) which creates an osmotic pressure difference between the hydrogel and the solvent. This causes an influx of solvent and counterions towards the dissociated groups, which results in a swelling of the hydrogel and subsequent

stress to the piezoresistive plate. At values above the pK_a, further increase of the swelling degree is attributed to the electrostatic repulsion of the charged polymer segments. In a pH sweep from pH 1 to 4.5, they reported a response time of about 2 min for 6 μm and up to 80 min for 50 μm layer thickness. In their second approach towards a chemical sensor, they confined a cut poly(N-isopropyl acrylamide) foil in the sensor chip. Upon addition of 20 vol.% of ethanol, the volume phase transition temperature of PNIPAM is shifted below room temperature, and the adjacent deswelling was recorded in the bending-plate signal until equilibrium was reached after about 60min.

In 2018, a similar alcohol sensor concept was introduced by Erfkamp et al. providing a full-range sensitivity from 0 to 100 % alcohol.[36] In their work, they incorporated the stimuli responsiveness of poly(acrylamide) gels towards methanol, ethanol, iso-propanol, and ethylene glycol in the chips sensing element. The different mono-alcohols caused only minor differences in the swelling behavior of PAAM gel as compared to the 50 % overall change in swelling degree. Through systematical variation of the monomer's volume or molar percentage of crosslinker in the pre-gel solution, they were able to adjust the hydrogel's sensitivity, particularly in the range of 20 to 60% alcohol content. Here, the sensitivity increases as the crosslinking density decreases. Meaning, lowering the physical and chemical crosslinking density, i.e. less crosslinker or lower initial monomer concentration, can increase the sensitivity of the hydrogel system. The response time is also significantly improved to around 20 min, as compared to the other sensor described above, despite that the PAAM gel is larger.

Minimizing the response times in this type of hydrogel sensors is one of the main focuses of the ongoing research with the aim of market maturity. The most time-consuming process is the diffusion-limited equilibration of the swelling degree for macroscopic hydrogels. To overcome this limitation, Deng et al. presented a force compensated hydrogel sensor design which benefited from a constant swelling degree of the sensing hydrogel, i.e., the swelling kinetics of the sensing gel became less significant.[37] In their approach, the force compensation was achieved by a thermoresponsive PNIPAM layer on the other side of the piezoresistive plate, as depicted in Figure 3 A. Any change in the solvent condition of the sensing gel – here pH-responsive PAA/PVA gel – was detected in the same manner as above except the signal is processed in a PI-controller regulating the solvent temperature of the PNIPAM layer via a Peltier element. When properly managed, the swelling pressure of both hydrogels will stay balanced, their swelling degree constant and the sensor signal
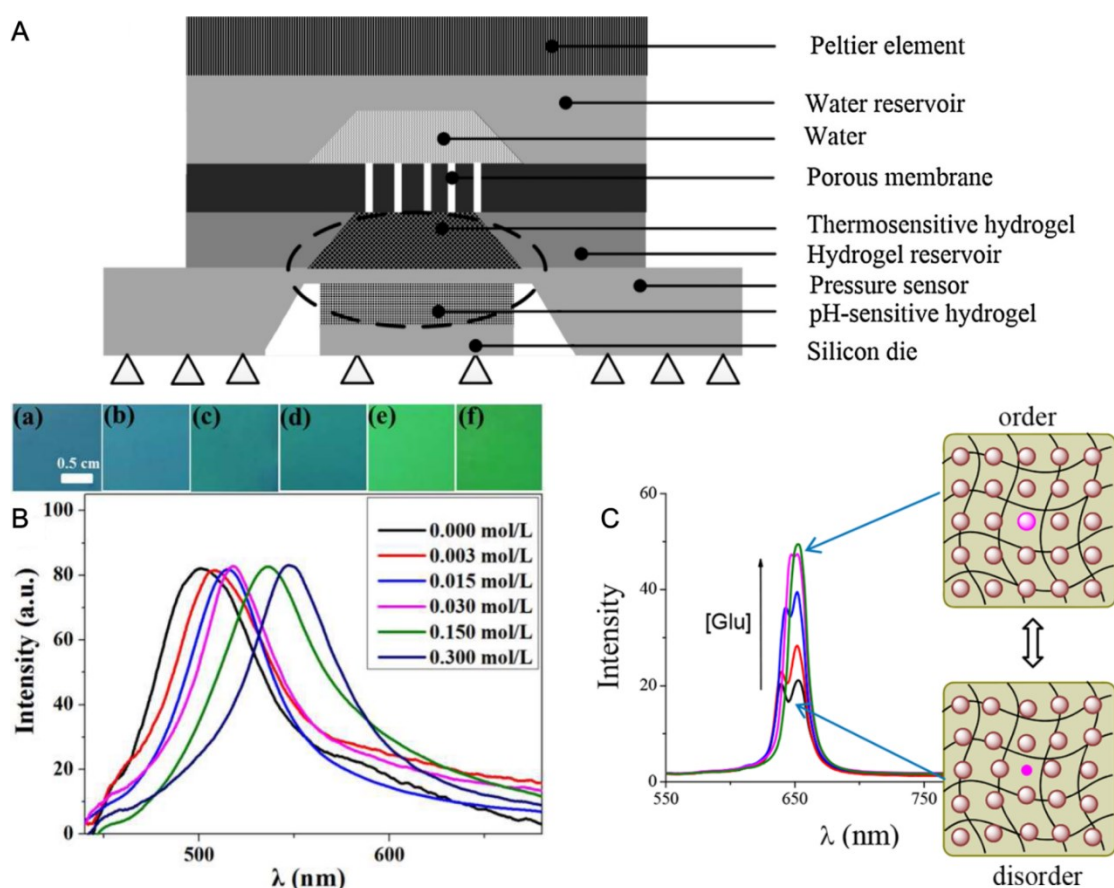
Figure 3 A) Force compensated hydrogel-based pH sensor design. Reprinted with permission.[37] Copyright 2018 Elsevier. B) 6 Photographs of PAAM macrogels with varying concentrations of formaldehyde showing a photonic response. Below, corresponding reflection spectra of the photonic hydrogels. Reprinted with permission.[38] Copyright 2018 ACS. C) Reflection spectra of the microgel colloidal crystal in the macroscopic hydrogel matrix with varying glucose concentration. The photonic response of the colloidal crystal is schematically depicted on the left. Reprinted with permission.[39] Copyright 2018 ACS.

is transferred from the voltage generated by the bending plate to the temperature of the Peltier element. As a result, they showed a response time reduction of ~ 15 min or ~ 30% when the sensor is working in force compensation mode.[37]

Besides the chip-based piezoresistive sensors, hydrogels or hydrogel composites are used in various approaches involving alternative detection techniques. Macroscopic PAAM gels incorporated with 1D photonic iron oxide nanoparticle chains can be used to optically detect aldehyde concentrations.[38] Free amine groups of PAAM react with aldehydes, which increases the polarity of the respective monomer unit. The associated swelling of the gel extends the spacing of the photonic nanoparticles, which is detectable via bare eyes as color change or by a spectral shift in UV-vis spectra, depicted in Figure 3 B.[38] Also relying on photonic effects, Jia et al. introduced an all hydrogel glucose sensor.[39] They fixed a colloidal crystal made of PNIPAM microgels and doped with p(NIPAM-co-AA) microgels of equal size in a macroscopic PAAM matrix. Upon chemical

modification of AA to (3-Aminophenyl) boronic acid sulfate, the dopant microgels deswell but become sensitive to glucose. In the deswollen state, without glucose, the dopant microgels represent photonic defects in the colloidal crystal reducing the Bragg peak intensity, schematically depicted with additional experimental data shown in Figure 3 C. With increasing glucose concentration, the colloidal crystal is continuously and reversibly rebuilt while the Bragg peak intensity rises.[39]

II.2.2. Actuators & Miscellaneous

Actuation through hydrogel expansion and contraction is of interest when movement, transport, or blockade is required.[40] Movement can be achieved most simply by placing an object close to or directly linking it to a responsive hydrogel. More complex actuation like bending or twisting can be forced by bringing two hydrogels with different swellability or one responsive hydrogel attached to an inert material. For example, controlled bending can be introduced by ionoprinting, which is the local incorporation of multivalent ions in a charged hydrogel, and thereby increasing the local crosslinking density and mechanics.[44] Swelling of the hydrogel will force the bending to occur alongside the patterned interface, as depicted in Figure 4 D, resulting in a controllable hydrogel roll-up or even sophisticated gripper arms, as known from robotic hands, can be achieved.[44]

Twisting motion can be accomplished in a bilayer hydrogel system, in which oriented mechanical reinforcement is present but shifted by 90° for the two layers. This was achieved experimentally by Erb et al. by aligning magnetic aluminum oxide plates in a rotating magnetic field before crosslinking the PNIPAM matrix.[43] Then, strips cut out from the bilayer unparalleled to the orientation of either layer showed twisting motion upon heating due to counter-acting mechanical stresses (Figure 4 C). The resulting geometry depended on various parameters, especially on the thicknesses of the single layers and the cutting angle.[43]

Transport as referred here, is another kind of motion when compared to the previously described motion, i.e., not only switching from position A to B but also propagating from B to C and D and so on. This can be realized by utilizing oscillatory chemical reactions, which ultimately affect the physical properties of a hydrogel.[42] A gradient hydrogel made from a copolymer of NIPAM, covalently bonded ruthenium(II) tris(2,2'-bipyridine) ($Ru(bpy)_3^{2+}$) as a catalyst and 2-acrylamide-2-methylpropane sulfonic acid as a lubricant was prepared into a sheet. Due to a higher concentration of $Ru(bpy)_3^{2+}$
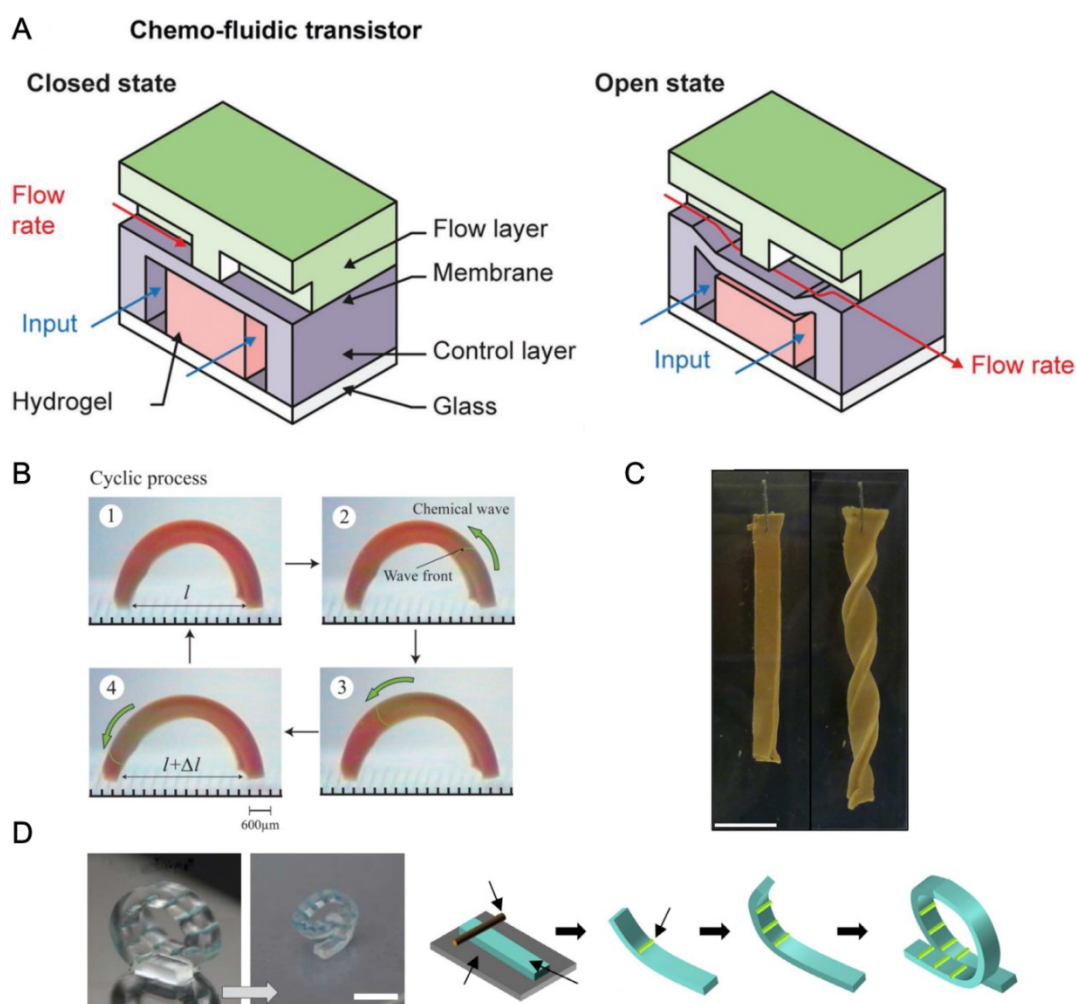
Figure 4 A) Device principle of the chemofluidic membrane. Reprinted with permission.[41] Copyright 2017, Wiley-VCH. B) Images of the repeated bending-stretching motion of the gel strip due to a chemical wave. Reprinted with permission.[42] Copyright 2007, Wiley-VCH. C) Synthetic chiral seedpods constructed by oriented magnetic platelets in gelatin as prepared (left) and fully hydrated (right). All scale bars are 1cm. Reprinted with permission.[43] Copyright 2013, Nature. D) Gel strip with induced stress by ionoprinted lines with a copper wire anode is used to fold the strip in 3D. Scale bar is 5 mm. Reprinted with permission.[44] Copyright 2013 Nature.

on one side, the swelling of the sheet was anisotropic, and the sheet bent preferentially towards this side. The continuous motion was introduced by the Belouzov-Zhabotinsky reaction[45, 46], which causes the catalyst-enriched side to oscillatory swell and contract. Since this reaction cycle was, to some extent, self-regulating, the oscillatory reaction exhibited a wave-like appearance, which was shorter than the dimensions of the hydrogels (Figure 4 B). This led to directed changes in swelling degree of the hydrogel sheet and resulted in a movement speed of 170 μm min^{-1}.[42]

Hydrogel actuators are also used in flow control of microfluidic devices. By adjusting their swelling degree, hydrogel units can block or open the fluidic channel and

serve as a valve. The switching can be either controlled off-chip, e.g., by adjusting the temperature at the hydrogel position,[47] or on-chip, by responsiveness to the solvent composition (pH, salt or non-solvent concentration) to form chemo-mechanical valves.[48] Based on such chemo-mechanical valves, transistor-like microfluidic components were designed as shown in Figure 4 A, which allows active selection and switching between different fluid streams on-chip.[41] With that, the microfluidic analogs of the AND, OR and NOT gates typically known from electronic circuit boards can be realized. On the other hand, more complex designs are also available including sequential logic analogs like the RS flip-flop enabling information storing capacity or a chemofluidic oscillator which periodically switches between two channel outputs.[41]

II.3.   Bioinspired Wet Adhesives

Bioinspired materials have become more and more intensively studied in the past decades since nature has developed elegant solutions to tackle various challenges, which later have become of great interest in the field of engineering and real-life applications. Examples found in nature include certain animals, like chameleons, certain beetles, and zebrafish, which are able to change or adapt their color in response to an external stimulus for camouflage.[49] Fu et al. also achieved autonomous color-changing materials by changing the photonic bandgap of an inverse opal structure in a hydrogel matrix through the beating rhythm of incorporated cardiomyocytes, shown in Figure 5 C.[52]

Another source of inspiration is the amazing capability of geckos to walk on almost all kinds of surfaces, regardless of walls and ceilings. The high and reversible adhesion of gecko pads was found to emerge from the hierarchically arranged fibrils with fine structures down to the nanometer range. This ensures that the geckos can easily adapt to various kinds of surface conditions. The unique structure leads to a maximized contact area, and the adhesion between surfaces is largely promoted through contact splitting of van der Waals and capillary forces. Inspired by the concepts of gecko adhesion, the creation of artificial surfaces with similar behavior is an attractive area of research, which would allow the realization of special glue-like systems or new ways of motion on slanted and even more complex surfaces.[53]

However, the unique adhesion abilities of geckos fail underwater or in very wet conditions.[54] To overcome this limitation, nature also supplies a strong countermeasure for wet adhesion. One great example is the mussels adhering to ship hulls under various
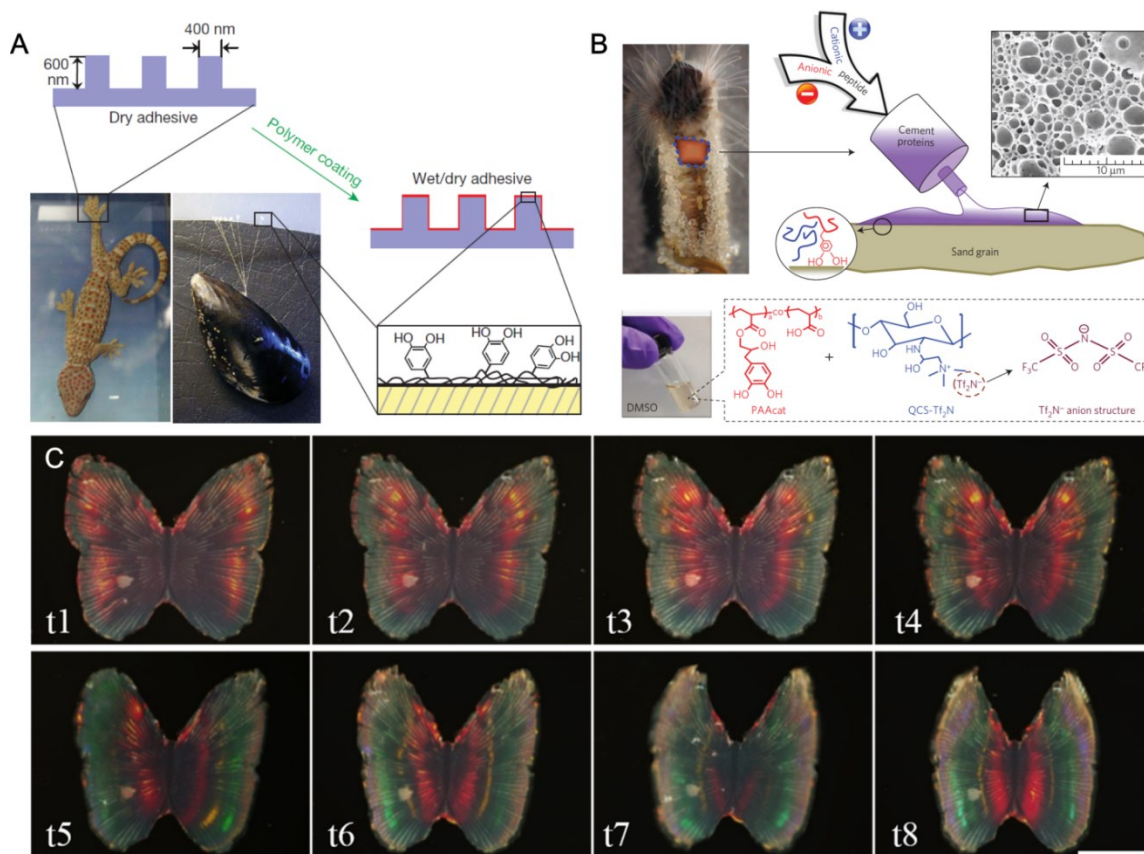
Figure 5 A) The hierarchical structure of the gecko foot is mimicked in micropillar array made of PDMS introducing dry adhesive properties (top left). The mussel inspired wet adhesion is achieved by coating with p(DMA-coMEA). Reprinted with permission.[50] Copyright 2007 Nature. B) The building organ of the sandcastle worm is highlighted (blue dashed lines, upper right). It produces polyanionic and polycationic proteins which constitute the adhesion and microarchitecture of the cement, schematically shown in the upper left. The thereby inspired synthetic components for the adhesive are shown in the lower part. Reprinted with permission.[51] Copyright 2016 Nature. C) Optical microscope images of the structural color variation process of a butterfly morphology structural color hydrogel during one myocardial cycle. Scale bar 2 mm. Reprinted with permission.[52] Copyright 2018 AAAS.

seawater conditions. While analyzing the plaque of mussel byssus a high concentration of 3,4-dihydroxyphenylalanine (DOPA) was found, which is considered to be one of the most important components for high underwater adhesion.[55-57] Many different strategies were explored to mimic the mussel adhesion towards high adhesive surfaces. The following sections will present a few highlights in detail.

A study by Lee and coworkers in 2007 developed an approach combining the concepts of gecko and mussels adhesion into one surface, to create a reversible wet/dry adhesive.[50] They modeled the hierarchical structure of gecko feet by a nanofabricated pillared surface with - 600 nm in height, 400 nm in width – using elastic poly(dimethyl siloxane). This surface was then dip-coated with a synthetic polymer of poly(dopamine methacrylamide-co-methoxyehtyl acrylate), which mimics the adhesion behavior of mussel proteins. The resulting adhesive performance was tested with a tipless triangular cantilever

through selectively contacting a discrete number of pillars in air and water. The best performance was observed for the coated surface in air with 120 nN adhesive force per pillar, which is three times higher as compared to the uncoated surface. With ~85 nN force of adhesion per pillar, the absolute adhesion of the coated surface is slightly reduced in water. Still, this performance is almost 15 times higher as compared to the plain gecko surface in aqueous solution.[50]

Although promising, the synthesis of materials that can fully resemble the underwater adhesion of the mussel foot protein is challenging. An approach to abstract and reduce the complexity of synthesis is to design low molecular weight zwitterionic surfactants, which was reported by Ahn et al.[58] Following the stoichiometric composition of mfp-5 with almost equal parts of cationic, catecholic and non-charged nucleic acids, also including a slightly smaller anionic part, they created a surfactant bearing a phosphate anion, a quaternary ammonium cation, a catechol end-group and a second hydrocarbon tail with varying length. Above the critical surfactant concentration, coacervate bilayer aggregates are formed. In surface force apparatus (SFA) measurements, ~20 mJ m^{-2} adhesion energy was observed for surfactants bearing hydrophobic butyl tail. Adhesion energies were maximized when two decyl (C10) tailed bilayers on two mica surfaces were brought into contact for 12 h in the presence of the oxidant periodate. The authors then postulated a bilayer crosslinking of two catechol groups could explain the more than doubled adhesion energy of up to ~50 mJ m^{-2}.[58]

The ability of sandcastle worms to construct their tubular homes and even bigger boulder-like concretions is another source of inspiration from nature conveyed to researchers.[59] To better understand the mechanism, five different glue proteins used by the sandcastle worm *Phragmatopoma californica* (Pc) were isolated. All of them containing a high percentage (~50 mol%) of chargeable amino acids. Additionally, 9.8 mol% DOPA was found in Pc1 and 7.3 mol% in Pc2.[60, 61] Albeit in-depth binding mechanism is still under debate, it is established that the worm secretes two distinct sets of oppositely charged polyelectrolytes (peptides) adjacent with other preloads in micrometer-sized modules. They undergo complex coacervation, also known in colloidal science[62], forming a fluid in fluid intermediate presumably triggered by the pH change in seawater. Finally, it was assumed that it primes in foam-like structures due to the enzyme-catalyzed oxidative crosslinking of DOPA units within the peptides. To achieve wet interfacial adhesion, the protein mixture secreted by the worm includes phosphates, primary amines,

quanidinium, aromatic heterocyclic amines, and catechols and are all associated with promoting adhesion.[60]

Adapting the gluing processes found with sandcastle worms, Zhao et al. successfully fabricated an ejectable artificial wet adhesive.[51] Their resin is formulated in dimethyl sulfoxide with a mixture of poly(acrylic acid) (PAA), a weak polyanion that is modified with 30 mol% of DOPA and quaternized chitosan, a strong polycation. Due to the dielectric constant of DMSO, the acidic groups in PAA are not dissociated. However, when this mixture is ejected into water, DMSO is exchanged in the extruded area. As a result, PAA will be charged and the polyelectrolytes will undergo complex coacervation, as described above. Again, DOPA is assumed to promote the interfacial adhesion, in the order of 2 mJ m^{-2} determined by SFA, while strong electrostatic interactions within the material provide stability, with the ability to withstand a 30 bar water jet after 1h of curing.[51]

II.4.   References

[9] J. V. Alemán, A. V. Chadwick, J. He, M. Hess, K. Horie, R. G. Jones, P. Kratochvíl, I. Meisel, I. Mita, G. Moad, S. Penczek, R. F. T. Stepto, "Definitions of terms relating to the structure and processing of sols, gels, networks, and inorganic-organic hybrid materials (IUPAC Recommendations 2007)", in *Pure and Applied Chemistry*, 2007, p. 79/1801.

[10] H. Elias, "Makromoleküle–Chemische Strukturen und Synthesen", 6. edition, Wiley-VCH Verlag, Weinheim, Weinheim, 2001346.

[11] M. D. Lechner, K. Gehrke, E. H. Nordmeier, U. Guhr, "*Makromolekulare Chemie"*, 5. edition, Springer, 2003.

[12] O. Virtanen, M. Brugnoni, M. Kather, A. Pich, W. Richtering, *Polymer Chemistry* **2016**, *7*, 5123.

[13] R. H. Pelton, P. Chibante, *Colloids and Surfaces* **1986**, *20*, 247.

[14] M. Kather, F. Ritter, A. Pich, *Chemical Engineering Journal* **2018**, *344*, 375.

[15] R. Tiwari, A. Walther, *Polymer Chemistry* **2015**, *6*, 5550.

[16] A. Melle, A. Balaceanu, M. Kather, Y. Wu, E. Gau, W. Sun, X. Huang, X. Shi, M. Karperien, A. Pich, *Journal of Materials Chemistry B* **2016**, *4*, 5127.

[17] A. C. Brown, S. E. Stabenfeldt, B. Ahn, R. T. Hannan, K. S. Dhada, E. S. Herman, V. Stefanelli, N. Guzzetta, A. Alexeev, W. A. Lam, L. A. Lyon, T. H. Barker, *Nature Materials* **2014**, *13*, 1108.

[18] Q. Zhang, L. Zha, J. Ma, B. Liang, *Journal of Colloid and Interface Science* **2009**, *330*, 330.

[19] L. Shang, Y. Cheng, Y. Zhao, *Chemical Reviews* **2017**, *117*, 7964.

[20] R. Seemann, M. Brinkmann, T. Pfohl, S. Herminghaus, *Reports on progress in physics* **2011**, *75*, 016601.

[21] J. Zhang, S. Yan, D. Yuan, G. Alici, N.-T. Nguyen, M. Ebrahimi Warkiani, W. Li, *Lab on a Chip* **2016**, *16*, 10.

[22] S. C. Hur, T. Z. Brinckerhoff, C. M. Walthers, J. C. Y. Dunn, D. Di Carlo, *PLOS ONE* **2012**, *7*, e46550.

[23] S. With, M. Trebbin, C. B. A. Bartz, C. Neuber, M. Dulle, S. Yu, S. V. Roth, H.-W. Schmidt, S. Förster, *Langmuir* **2014**, *30*, 12494.

[24] O. Otto, P. Rosendahl, A. Mietke, S. Golfier, C. Herold, D. Klaue, S. Girardo, S. Pagliara, A. Ekpenyong, A. Jacobi, *Nature methods* **2015**, *12*, 199.

[25] T. Heida, J. W. Neubauer, M. Seuss, N. Hauck, J. Thiele, A. Fery, *Macromolecular Chemistry and Physics* **2017**, *218*, 1600418.

[26] A. S. Utada, A. Fernandez-Nieves, H. A. Stone, D. A. Weitz, *Physical Review Letters* **2007**, *99*, 094502.

[27] P. Guillot, A. Colin, *Physical Review E* **2005**, *72*, 066301.

[28] S. L. Anna, H. C. Mayer, *Physics of Fluids* **2006**, *18*, 121512.

[29] G. F. Christopher, S. L. Anna, *Journal of Physics D: Applied Physics* **2007**, *40*, R319.

[30] M. De Menech, P. Garstecki, F. Jousse, H. A. Stone, *Journal of Fluid Mechanics* **2008**, *595*, 141.

[31] S.-Y. Teh, R. Lin, L.-H. Hung, A. P. Lee, *Lab on a Chip* **2008**, *8*, 198.

[32] S. Hardt, K. Drese, V. Hessel, F. Schönfeld, "Passive micro mixers for applications in the micro reactor and μTAS field", in *ASME 2004 2nd International Conference on Microchannels and Minichannels*, American Society of Mechanical Engineers, 200445.

[33] H. Song, J. D. Tice, R. F. Ismagilov, *Angewandte Chemie International Edition* **2003**, *42*, 768.

[34] G. Gerlach, M. Guenther, G. Suchaneck, J. Sorber, K. F. Arndt, A. Richter, *Macromolecular Symposia* **2004**, *210*, 403.

[35] G. Gerlach, M. Guenther, J. Sorber, G. Suchaneck, K.-F. Arndt, A. Richter, *Sensors and Actuators B: Chemical* **2005**, *111*, 555.

[36] J. Erfkamp, M. Guenther, G. Gerlach, *Journal of Sensors and Sensor Systems* **2018**, *7*, 219.

[37] K. Deng, C. Bellmann, Y. Fu, M. Rohn, M. Guenther, G. Gerlach, *Sensors and Actuators B: Chemical* **2018**, *255*, 3495.

[38] X. Jia, T. Zhang, J. Wang, K. Wang, H. Tan, Y. Hu, L. Zhang, J. Zhu, *Langmuir* **2018**, *34*, 3987.

[39] S. Jia, Z. Tang, Y. Guan, Y. Zhang, *ACS Applied Materials & Interfaces* **2018**, *10*, 14254.

[40] L. Ionov, *Materials Today* **2014**, *17*, 494.

[41] P. Frank, D. Gräfe, C. Probst, S. Haefner, M. Elstner, D. Appelhans, D. Kohlheyer, B. Voit, A. Richter, *Advanced Functional Materials* **2017**, *27*, 1700430.

[42] S. Maeda, Y. Hara, T. Sakai, R. Yoshida, S. Hashimoto, *Advanced Materials* **2007**, *19*, 3480.

[43] R. M. Erb, J. S. Sander, R. Grisch, A. R. Studart, *Nature Communications* **2013**, *4*, 1712.

[44] E. Palleau, D. Morales, M. D. Dickey, O. D. Velev, *Nature Communications* **2013**, *4*, 2257.

[45] F. Schneider, *Angewandte Chemie* **1986**, *98*, 941.

[46] A. N. Zaikin, A. M. Zhabotinsky, *Nature* **1970**, *225*, 535.

[47] K. Ito, S. Sakuma, Y. Yokoyama, F. Arai, *ROBOMECH Journal* **2014**, *1*, 5.

[48] K. F. Arndt, D. Kuckling, A. Richter, *Polymers for Advanced Technologies* **2000**, *11*, 496.

[49] G. Isapour, M. Lattuada, *Advanced Materials* **2018**, *30*, 1707069.

[50] H. Lee, B. P. Lee, P. B. Messersmith, *Nature* **2007**, *448*, 338.

[51] Q. Zhao, D. W. Lee, B. K. Ahn, S. Seo, Y. Kaufman, J. N. Israelachvili, J. H. Waite, *Nature Materials* **2016**, *15*, 407.

[52] F. Fu, L. Shang, Z. Chen, Y. Yu, Y. Zhao, *Science Robotics* **2018**, *3*.

[53] L. F. Boesel, C. Greiner, E. Arzt, A. del Campo, *Advanced Materials* **2010**, *22*, 2125.

[54] G. Huber, H. Mantz, R. Spolenak, K. Mecke, K. Jacobs, S. N. Gorb, E. Arzt, *Proceedings of the National Academy of Sciences of the United States of America* **2005**, *102*, 16293.

[55] J. H. Waite, *Annals of the New York Academy of Science* **1999**, 875, 301.

[56] M. Yu, J. Hwang, T. J. Deming, *Journal of the American Chemical Society* **1999**, *121*, 5825.

[57] B. P. Lee, P. B. Messersmith, J. N. Israelachvili, J. H. Waite, *Annual Review of Materials Research* **2011**, *41*, 99.

[58] B. K. Ahn, S. Das, R. Linstadt, Y. Kaufman, N. R. Martinez-Rodriguez, R. Mirshafian, E. Kesselman, Y. Talmon, B. H. Lipshutz, J. N. Israelachvili, J. H. Waite, *Nature Communications* **2015**, *6*.

[59] H. Zhao, C. Sun, R. J. Stewart, J. H. Waite, *Journal of Biological Chemistry* **2005**, *280*, 42938.

[60] C. S. Wang, R. J. Stewart, *Biomacromolecules* **2013**, *14*, 1607.

[61] C. S. Wang, R. J. Stewart, *The Journal of Experimental Biology* **2012**, *215*, 351.

[62] E. Spruijt, "*Strength, structure and stability of polyelectrolyte complex coacervates*", PhD thesis, Wageningen University, The Netherlands, **2012**.

III. Theoretical Background

After introducing the broad interest in science and everyday life for hydrogel-based materials and adhesives and giving an overview of current techniques and topics discussed in the literature, this chapter collects the working principle of an atomic force microscope as well as the theoretical concepts in the field of contact mechanics.

III.1. Atomic Force Microscopy

Investigating matter and effects on their fundamental length scales down to the single-molecule level is for many years the focus of theoretical and applied scientists. Beginning with optical microscopes introduced in the 17th century[63], higher and higher magnifications were desired to dig deeper. In the early 20th century, a leap in resolution was achieved by surpassing the resolution limit of light using electrons. Transmission and scanning electron microscopy, both concepts developed in the 1930s, are essential tools in nowadays academic and industrial research providing high-resolution images.[64-66]

About 50 years later Gerd Binning and coworkers introduced the scanning tunneling microscope (STM), measuring the tunneling voltage between a sharp tungsten tip and platinum surface with controlled separation distances of around 1 nm. They reported possible imaging resolutions of 0.2 to 0.5 nm vertical and 1 nm laterally.[67] Only four years later, Binning and Rohrer received the Nobel prize for physics and, even more importantly, for soft matter science, Binning designed the atomic force microscope (AFM). With that, he circumvented the necessity of electrical conductance of the sample surface, allowing physical contact with the sample and the possibility of measuring interaction forces down to pico Newtons. The "atomistic" interactions are converted to a signal first by deflection of an AFM cantilever spring which in turn was recorded through the change of the tunneling voltage between AFM cantilever and an STM tip in close proximity.[68]

The device complexity in commercial AFM was reduced through the implementation of the optical lever technique, simplifications in the controlling software and overall handling, establishing it as a widely applied characterization tool in physics and polymer chemistry. The following chapters provide a selected overview of applications of the AFM in the field of recording interaction forces. First, imaging methods are reviewed with a brief excurse to "all-in-one" imaging. Secondly, a particular focus is laid on theoretical considerations for extracting interaction properties from force spectroscopy

mode, including practical examples. Further, the benefits of colloidal probes for soft matter investigations are highlighted as well as the unique capabilities of AFM to operate in various environmental conditions.

Note here, that after working extensively with AFM for nine years I consider myself as an expert on the topic, which is why the following sub-chapters are written from my experienced view point. I only highlight certain high quality review articles, which sum up the measurement concepts and provide the reader with secondary literature.

III.1.1. Topology and Advanced Imaging

The majority of studies applying AFM use the device to record topography images with dimensions of some square micrometer to visualize features down to the nanometer scale. To do so, the tip of the cantilever, with a typical radius of curvature around 10 nm, is scanned over the surface by two piezoelectric actuators for in-plane movement while the separation and vertical distance are controlled by a third piezo. Some devices use a single tube piezo actuator, managing all three directions simultaneously. From such a scan, a virtual image is reconstructed in which the actual height of the scanned surface is represented in a false-color image. Measuring real 3D images is the benefit of AFM compared to standard electron microscopy images displaying mainly electron density contrast.

The two classical AFM imaging modes are *contact mode* and *tapping mode* ™ – also called *intermitting contact mode*. In contact mode, the tip is brought in constant, physical contact with the surface and scanned either at a constant height, e.i. constant piezo extension, or at constant cantilever deflection. In the latter, changes in topography are first detected by an unintended variation of the cantilever deflection. This variation is compensated by changes in the vertical piezo extension, which is controlled through a feedback loop. The sample height information is recorded as the changes the piezo has to perform in order to keep a constant cantilever deflection. In constant height mode, there is no feedback, and relative changes in height are directly measured by the cantilever. Both methods are nowadays only used in individual cases of soft matter research since they are prone to probe and sample wear due to friction and low imaging speed. However, applications include sub-nanometer resolution imaging or avoidance of artifacts from fast dynamic movement of the cantilever. Tapping mode ™ imaging became the standard since it reduces wear dramatically and allows for fast image recording for most sample surfaces.
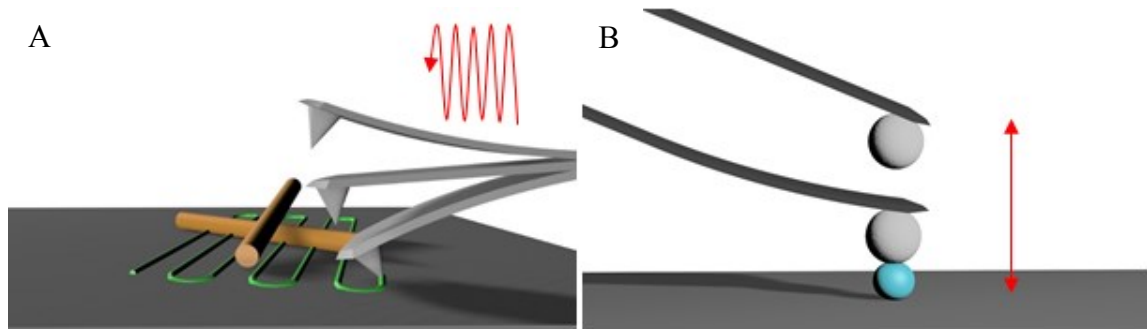
Figure 6   A) Schematic representation of an oscillating cantilever with a sharp tip. The scanning motion is indicated by the green lines in the substrate to image the two cylinders lying on the substrate. B) Schematic depiction of a colloidal probe cantilever making a one-dimensional ramp movement to record a force-distance curve on the blue spherical particle.

Here, the cantilever is oscillated vertically by the piezo close to its resonance frequency and therefore touching the sample only for a short interval. A brief contact, however, is enough to damp the oscillation amplitude as compared to free movement in air which is used as a feedback input.[69] While scanning the vibrating cantilever, a change in height directly affects the damping, which is regulated in the feedback by adjusting the amplitude center. Figure 6 A shows a schematic depiction of the tapping mode™ scanning. From that, height maps can be reconstructed similar to the constant deflection mode. Additionally, the phase difference between externally applied oscillation and recorded cantilever oscillation provides further qualitative insight. For multiple component samples, a contrast in the phase-channel indicates variation inelastic or adhesion properties; however, quantitative information is complicated to infer and more possible contributions are hard to distinguish here.

To also access mechanical and adhesion information, new imaging modes were developed and become more and more popular. These "all-in-one" methods are, for example, provided by Bruker© named PeakForce® "Quantitative Nanomechanical" (QNM®) imaging or by JPK© called "Quantitative Imaging" (QI®). Both are in a sense advancements of the so-called force-volume technique collecting vertical force-distance curves in a lateral grid, which will be explained in detail in the next chapter. Moving the cantilever in a vertical, sinusoidal "heartbeat" fashion (QNM®) or in "saw-tooth" like trajectory (QI®) with frequencies in kHz range hundreds of thousands of force-distance curves are recorded and online evaluated. The preset algorithm extracts the maximum adhesion forces between tip and sample and calculates the elastic modulus based on Derjaguin, Muller, Toporov (DMT) (see chapter III.2.3) at every pixel. This additional

information can give valuable insight into the sample's characteristic which is extremely hard to capture with different techniques.

However, from my personal experience over the years, this online created information needs to be interpreted with a lot of care. While the adhesion channel is, in my opinion, less prone to erroneous values, especially the E module values can very easily lead to wrong conclusions. For instance, the algorithm evaluates every curve the same way regardless of artifacts being present or not. Further, changes in tip radius, transitions between DMT and Johnson, Kendall, Roberts theory (JKR) (see chapter III.2.4), variations in contact area due to different shapes of the indenter and other parameters of uncertainty are not considered. Therefore, elastic information from these techniques may serve for qualitative interpretations, but high-quality absolute values should be derived from careful, individual analysis and modeling of the single measurements.

III.1.2. Force- and Interaction Spectroscopy

The already above-mentioned force-distance measurements represent the fundamental working principle of an atomic force microscope and its essentials, limitations, and theoretical background are summarized in this chapter. The very basic of an AFM is to record separation or distance-dependent changes in interactions force between probe, attached at the free end of a cantilever, and sample. Therefore, the probe separation is varied by a piezo element in the vertical direction by moving the complete cantilever, schematically depicted in Figure 6 B. Meanwhile, a change in interaction force causes the cantilever to bend. This, in turn, is monitored with high precision using the optical lever technique by reflecting a laser beam from the backside of the cantilever onto a quarter segmented photodiode. A variation in interactions force alters the laser position on the detector which is measured as a voltage difference between the upper and lower half. Summarizing, the raw data of the experiment are the piezo position and the corresponding voltage signal of the photodetector.

These raw data need to be converted to physical quantities as force versus separation or deformation, allowing for interpretation and modeling. First, the correlation between changes of the detector voltage (ΔV) and cantilever bending should be linear in a correct setup. The constant of proportionality, the inverse optical lever sensitivity ($InvOLS$), can be determined by ramping the probe against an undeformable surface. While in contact, every movement of the piezo directly causes the cantilever to bend by the same distance allowing conversion from voltage to real space deflection. This deflection is related to an

acting force according to Hook's law with the cantilever spring constant k is the proportionality coefficient, see equation 1.

$$F = InvOLS \cdot \Delta V \cdot k \tag{1}$$

The spring constant of every cantilever needs to be determined individually, e.g., from beam theory or the so-called thermal noise method since its thickness of around 2 μm is technically very difficult to control in the manufacturing process.[70] The other raw information, the piezo movement Z_P, is initially movement in arbitrary space. Through the definition of a reference point, it is converted to coordinates relative to the sample. Possible reference points are the onset of repulsive interactions, e.i. the point of initial contact $Z_{0,D}$ for compliant surfaces, or the constant compliance regime. Here further approaching only leads to cantilever deflection and the absolute zero in separation $Z_{0,S}$ of probe and sample can be defined. Also, the bare cantilever deflection at every position is overlaying the response of the sample and is therefore subtracted leaving only the material response. Consequently, the deformation D is defined by equation 2 and the separation S is defined by equation 3.

$$D = Z - Z_{0,D} - InvOLS \cdot V(Z) \tag{2}$$

$$S = Z - Z_{0,S} - InvOLS \cdot V(Z) \tag{3}$$

Here assuming that Z increases with extending piezo and therefor shrinking distance between probe and surface. While $Z_{0,S}$ is rather easy to identify, the reference point for deformation is especially difficult to pinpoint for soft materials and if surface forces are present.[71]

Typical force-distance curves involve six distinct regimes that will be shortly introduced in the order of appearance in measurement and depicted in Figure 7. At the start the cantilever is far away from a surface and is moved through the measurement medium where no directed interaction forces should be present. In this baseline regime, no changes in force with respect to movement are present which is also used to calibrate the detected voltage signal. Before initiating contact, long-range interactions may be present leading to a first deflection of the cantilever depending on the nature, e.i. repulsive or attractive. After contacting, both short and long-range interactions can be acting while the short-range elastic forces become dominating at higher deformations. Reaching the predefined setpoint of deflection the movement direction is reversed, stored elastic energy is released, and visco-elastic effects may shift the trajectory of the force-distance curve.
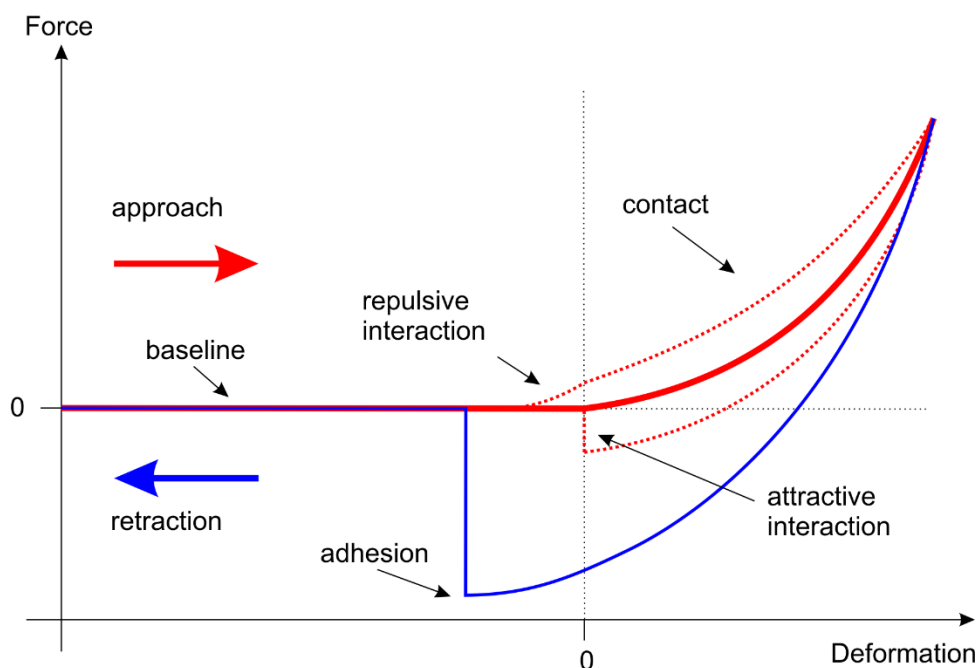
Figure 7   Schematic force-deformation curve highlighting possible differences while approaching (red) and including adhesive interactions while retracting (blue) the probe from a sample.

In case adhesive interaction forces arestrong enough, a fifth regime is entered where the cantilever remains in contact with the sample, and it starts to pull. At a distinct negative deflection of the cantilever the pulling force overcomes the maximal adhesion force, and the cantilever snaps out-off contact back to the original baseline.

III.1.3. Advantages of Colloidal Probe Force Spectroscopy

All interaction properties detectable by AFM are as mentioned distance-dependent. Therefore the shape and the size of the probing tip play a crucial role in the net forces measurable at a given distance. Standard AFM probes involve a conical sharp tip probe with tip radii below 15 nm and opening half angles in the area of 15°. This geometry benefits the lateral resolution of measurements – images and force-distance curves – since force contributions away from the apex become rapidly negligible due to the separation. However, when investigating weak interaction forces or highly compliant objects, the net forces acting on a sharp tip can be become extremely small and therefore coming close to the resolutions limit of an AFM. Further, the actual exact geometry of such tips is complicated to determine and especially the apex is very fragile.

If the lateral resolution is of less importance, these drawbacks can be hurdled by substituting the sharp tip with a spherical microparticle called colloidal probe. With its typical radius between 2 and 30 µm, the interaction area is increased significantly, resulting in higher net forces. Further, a sphere is one of the easiest shapes to describe analytically

reducing the complexity of the modeling equations to a minimum. The most prominent equation in this context is the Derjaguin approximation stating that the force $F_{Derjaguin}$ acting between a rigid sphere and rigid plane is proportional to the interaction potential $V_{Derjaguin}$ between to flat surfaces at the same separation distance δ

$$F_{Derjaguin}(\delta) = 2\pi R V_{Derjaguin}(\delta) \qquad (4)$$

The colloidal probe also brings benefits for the mechanical analytics of compliant materials, such as gels or polymer samples, since stress peaks in the contact area and possible piercing effects of a sharp tip can be avoided.

III.1.4. Unique Capabilities of Environmental Management

A further significant advantage of the AFM in contrast to the scanning electron microscopy (SEM) or transmission electron microscopy (TEM) is its capability to work in various environmental conditions and is not limited to high vacuum situations. Experiments in liquid media can be performed with relatively little additional effort opening the road for biological investigations with living cells, for material chemists investigating swollen samples, e.g., gels or polymer brushes. Further, one is not limited to pure water as a solvent, but one can add further compounds to change, e.g. ionic strength, pH, solvent (e.g. H_2O/ethanol) and gas (e.g., relative humidity) composition, or trigger molecules. Additionally, liquids can be used to reduce or eliminate AFM imaging artifacts of high energy surfaces in air. Furthermore, external physical parameters can be changed without affecting the measuring technique like temperature, applying magnetic and electric fields, shining light or external mechanical force.

III.2. Contact Mechanics and Adhesive Interactions

Understanding and describing contacting objects is a huge theme in physics and engineering. The phrase *contact mechanics* can be used as a headline to different research fields: first to mention tribology, the science of interacting surfaces in relative motion, focusing on frictional behavior, lubrication, and wear effects. Secondly, fracture mechanics, the study of crack propagation in materials, which may ultimately cause device failure. And finally, the study of elasticity, plasticity, and adhesiveness of materials providing essential input to engineers developing new devices and structures.

Since this thesis is mainly focusing on the last of the three topics, this chapter reviews the three *classical* contact theories, their later merge into a unified theory, and more recent approaches to improve their significance to very soft microparticles.

III.2.1. "Ueber die Berührung fester elastischer Körper" – The Hertz-Model

In 1881 Heinrich Hertz published one of the groundbreaking papers in the field of contact mechanics, which was and still is today the basis for new, more elaborate theories.[72] The authorized English translation can be found in the following reference.[73] The motivation of his work was to find mathematical descriptions for the contact of two touching bodies regarding: the size of the contact area; the shape of the contact area; the distribution of vertical pressure within the contact area; the deformation of the bodies caused by a given pressure; the maximum pressure the bodies can withstand without permanent deformation. These, of course, are very general questions that can depend on a vast number of external and internal material properties. Therefore, he restricted his considerations to completely elastic, isotropic, smooth objects where no lateral or adhesive forces are taken into account. These material and measurement criteria are the well-accepted checklist in nowadays research and are relatively easy to verify. Other assumptions he made during the development of his theory are very complicated to control experimentally or are sometimes ignored. To mention here the most important, in the author's opinion, are:

- The contact area is extremely tiny compared to the overall size of the objects, i.e. the objects are infinite compared to the contact area.
- The pressure and deformation outside of the contact area are infinitely small and negligible.
- In infinity, but still within the objects, there is no displacement of matter, i.e. no deformation.
- The overall applied pressure is exclusively located in the contact area.

In the elaboration of this theory, the contact area of both bodies in x and y direction, while the macroscopic shape is unspecified, is assumed to be described by a homogeneous quadratic function relative to the initial point of contact. The overall potential *P* satisfying all assumptions in the general case is found to be:

$$P = \frac{3p}{16\pi} \int_{u}^{\infty} \left(1 - \frac{x^2}{a^2 + \lambda} - \frac{y^2}{b^2 + \lambda} - \frac{z^2}{\lambda}\right) \frac{d\lambda}{\sqrt{(a^2 + \lambda)(b^2 + \lambda)\lambda}}. \tag{5}$$

Here p is the total pressure, a and b are the semi-axes of the ecliptic contact area in x and y-direction, λ is the integration substitute for u, which is the positive root of the following equation:

$$\frac{x^2}{a^2 + u} + \frac{y^2}{b^2 + u} + \frac{z^2}{u} = 1 \tag{6}$$

To note here, there is a typo in the English version showing x_2 instead of x^2.[72, 73] It follows that the deformation of both bodies δ is:

$$\delta = \frac{3p}{8\pi} \frac{\vartheta_1 + \vartheta_2}{a} \int_0^\infty \frac{dz}{\sqrt{(1 + k^2 z^2)(1 + z^2)}} \tag{7}$$

with $= \frac{a}{b}$, the ratio of the two semi-axes, and $\vartheta_i = \frac{2(1+\theta)}{K(1+2\theta)}$ the combined mechanical properties of the i-the body in the Kirchhoff notation.[74]

These equations simplify when considering two spheres in contact, as schematically depicted in Figure 8, since equation 6 becomes:
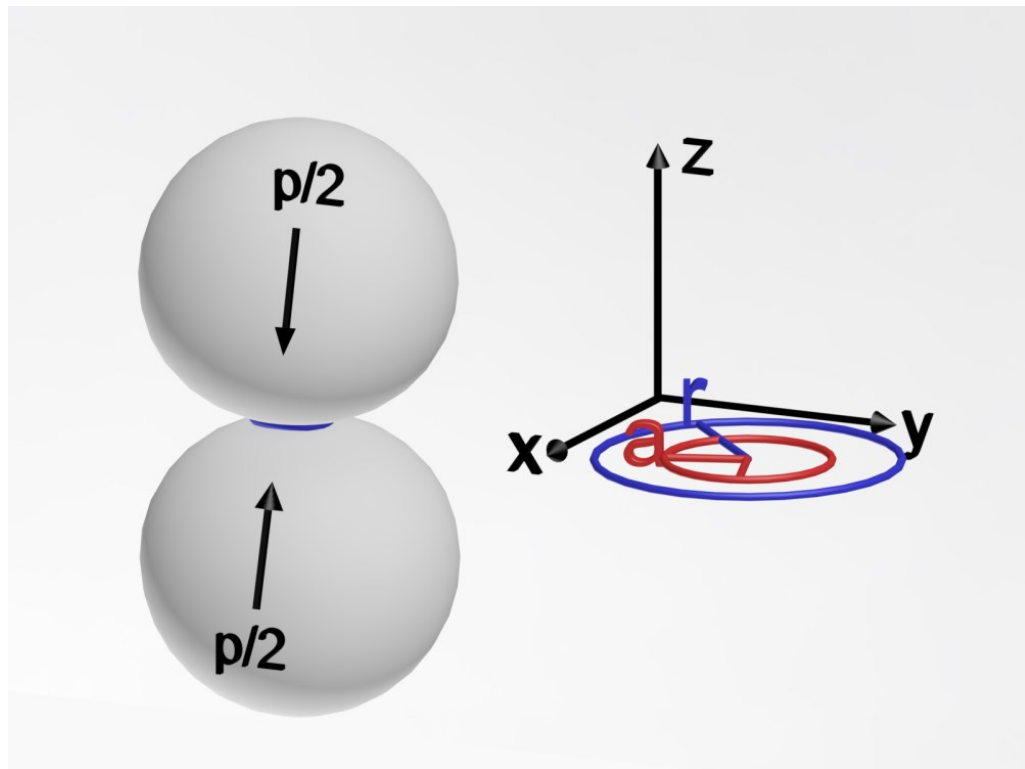
Figure 8   Schematic depiction of two spheres in contact due to external pressure p with a coordination system to show the specific directions used in the equations and the scheme of the contact area with radius r and the subsections with the semi-axes a which are integrated in equation 10

$$\frac{r^2}{a^2 + u} + \frac{z^2}{u} = 1; \quad x^2 + y^2 = r^2 \tag{8);(9}$$

$$P_{sph.} = \frac{3p}{16\pi} \int_u^\infty \frac{1 - \frac{r^2}{a^2 + u} - \frac{z^2}{u}}{(a^2 + u)\sqrt{u}} \, du \tag{10}$$

$$\delta_{sph.} = \frac{3p(\vartheta_1 + \vartheta_2)}{16 a_{cont.}} \tag{11}$$

$$a_{cont.} = \sqrt[3]{\frac{3p(\vartheta_1 + \vartheta_2)}{16(\rho_1 + \rho_2)}} \tag{12}$$

Here ρ_i denotes the reciprocal radius of the i-the sphere. Since this Kirchhoff notation is nowadays less frequently used, they can be transformed with

$$\vartheta_i = \frac{2(1 + \theta)}{K(1 + 2\theta)} = \frac{4}{E} \cdot \left(1 - \frac{\theta^2}{(1 + 2\theta)^2}\right); \quad v = \frac{\theta}{1 + 2\theta} \tag{13);(14}$$

to the now used relations involving the elastic modulus E and the Poisson's ratio v.

This gives the well-known Hertzian equations for two spheres in elastic contact:

$$a_{cont.} = \sqrt[3]{\frac{pR_{eff.}}{E_{tot}}}; \quad \delta = \frac{a^2_{cont.}}{R_{eff.}} = \sqrt[3]{\frac{p^2}{R_{eff.}E^2_{tot}}} \tag{15);(16}$$

$$\frac{1}{E_{tot}} = \frac{3}{4}\left(\frac{1 - v_1^2}{E_1} + \frac{1 - v_2^2}{E_2}\right); \quad \frac{1}{R_{eff.}} = \frac{1}{R_1} + \frac{1}{R_2} \tag{17);(18}$$

Besides the above mention checklist for Hertzian contact, the power-law dependence of $p \propto \delta^{1.5}$ is a final check for the experimental data to validate the applicability of the Hertz Model.

III.2.2. Surface Energy and the Contact of Elastic Solids – The Johnson-Kendall-Roberts Model

The Hertzian model was well accepted, but around 70 years later, contact experiments were conducted for which the current model failed to explain the results. In their dissertations, Roberts observed for two smooth rubber spheres[75] and Kendall for two glass spheres[76] that at low external loads the contact area is significantly bigger than predicted by the Hertz theory and finite at zero load. They attributed this to additionally acting surface forces causing an adhesive interaction between the two surfaces. Together

with Johnson, also a coworker at the University of Cambridge at the time of their Ph.D. dissertations, they developed their famous own contact mechanics model.[77]

Their theory bases on the known Hertzian model, which they extended in an energy equilibrium consideration by adhesives surface interactions. Their assumption is, that the total energy U_T of two smooth spheres in contact, schematically depicted in Figure 9 A & D, is the sum of mechanical energy U_M, elastically stored energy U_E and surface energy U_S. To determine U_E, we first assume non-adhesive contact under an external load P_0 with the resulting deformation and contact radius according to chapter III.2.1 and depicted as situation A in Figure 9. "Switching on" adhesive interactions between the two bodies, the contact radius increases to a_1 resulting in situation B in Figure 9. Corresponding to this, an apparent Hertzian load force P_1 and deformation δ_1 can be attributed. Here, the stored elastic energy in the system is:

$$U_{E,1} = \int_0^{P_1} \delta_1 \, dP = \int_0^{P_1} \frac{2}{3} \frac{P^{2/3}}{K^{2/3}R^{1/3}} dP = \frac{2}{5} \frac{P_1^{5/3}}{K^{2/3}R^{1/3}} \tag{19}$$

This apparent load P_1 is, however, higher than the actual applied load P_0. Therefore, the external load is reduced while the contact radius a_1 is maintained constant, which can also be interpreted as a reduction of deformation in a flat punch like geometry. Here, the load-deformation relation is given by

$$\delta = \frac{2}{3Ka_1} P \tag{20}$$

resulting in a change of elastic energy $U_{E,2}$ of

$$U_{E,2} = \int_{P_0}^{P_1} \frac{2}{3Ka_1} P \, dP = \frac{1}{3K^{2/3}R^{1/3}} \left(\frac{P_1^2 - P_0^2}{P_1^{1/3}} \right) \tag{21}$$

$$U_E = U_1 - U_2 = \frac{1}{3K^{2/3}R^{1/3}} \left(\frac{1}{5} P_1^{5/3} + P_1^{-1/3} P_0^2 \right) \tag{22}$$

with the total elastic energy U_E. This energy is balanced by the potential mechanical energy U_M which is calculated as

$$U_M = -P_0 \delta_2 = -P_0 \left(\delta_1 - \frac{2}{3Ka_1}(P_1 - P_0) \right) = \frac{-P_0}{K^{2/3}R^{1/3}} \left(\frac{1}{3} P_1^{2/3} + \frac{2}{3} P_0 P_1^{-1/3} \right) \tag{23}$$
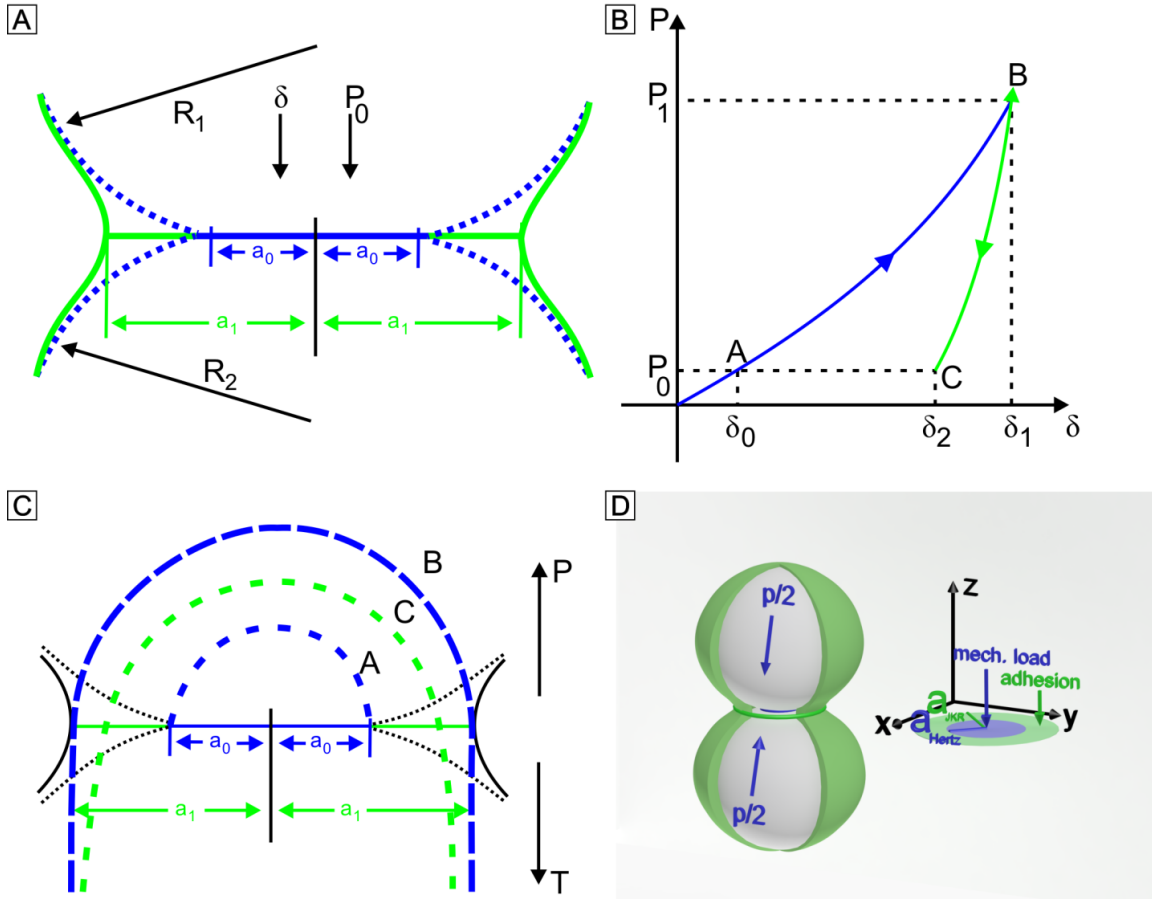
Figure 9 Schematic view on the contact between two elastic spheres with adhesion (contact radius a_1) and without adhesion (contact radius a_0). A) Cross-sectional view of two spheres (radius R_1 and R_2) under external load P_0 deforming the bodies by δ. Blue parts depict Hertzian contact and green part JKR contact. B) External load P versus deformation δ dependency of how the JKR-theory is derived. C) Similar scheme as in A) with the stress distributions A, B, and C according to the situations in B). Subfigures A) to C) are adapted from original publication with permission.[77] D) Schematic 3D of the JKR contact situation.

Introducing the surface energy $U_S = -\pi\gamma a_1^2 = -\pi\gamma(RP_1/K)^{2/3}$ leaves the total energy of the system U_T to be

$$U_T = \frac{1}{3K^{2/3}R^{1/3}}\left[\frac{1}{5}P_1^{2/3} - P_0^2 P_1^{-1/3} - P_0 P_1^{2/3}\right] - \pi\gamma(RP_1/K)^{2/3} \tag{24}$$

In equilibrium the total energy is constant and therefore the overall acting force is

$$P_1 = P_0 + 3\gamma\pi R + \sqrt{[6\gamma\pi RP_0 + (3\gamma\pi R)^2]} \tag{25}$$

Further, the JKR theory assumes that the Hertzian contact radius equation is still valid and with the modified acting force the contact radius is given by

$$a^3 = \frac{R}{K}\left(P_0 + 3\gamma\pi R + \sqrt{[6\gamma\pi RP_0 + (3\gamma\pi R)^2]}\right) \tag{26}$$

The theory is self-consistent since zero interfacial energy will result in the Hertz equations, which are neglecting adhesion. From the considerations made before deriving

the JKR theory, its relevance and applicability are of great interest for contact problems involving a high contact radius at low external loads since then the contribution of the surface energy term in the energy balance is dominating. Typical examples are contacts of soft material (low K) with a high radius of curvature or high surface energy surfaces.

III.2.3. Effect of Contact Deformations on the Adhesion of Particles – The Derjaguin-Muller-Toporov Theory

The second contact mechanics theory including adhesion with high impact in the scientific world was first introduced by Derjaguin, Muller, and Toporov in 1974.[78] Although its intensive use, there is still an ongoing debate about its accuracy, boundary conditions of validity and theoretical inconsistencies within the theory.[79] Due to that and since the theory itself only plays a minor role within this thesis, this chapter only gives a brief overview of the conceptual picture and the derived equations.

The DMT theory bases on the picture of small – without explicit size specification -, curved particles interacting and coming into contact with a flat, undeformable surface. The key difference to the JKR theory described in chapter III.2.2 is, that the adhesive interaction outside, but close to the contact area, is considered to contribute to the overall force, rather than the surface energy within the contact area. In the fifth and final iteration of their theory in 1983, they applied the distance-dependent Lennard-Jones interaction potential V_{L-J} to describe the forces acting in the vicinity, close to the contact area, as schematically shown in Figure 10.[80] These interactions give rise to an additional force contribution in the contact situation, which can be determined with the well-known Derjaguin approximation

$$F_{outside}(H) = 2\pi R V_{L-J}(H) \tag{27}$$

linking, in general, the interaction force of sphere-plane geometry to the interaction potential of two planes with the same separation H.[81] Note here, that the Derjaguin approximation of 1934 only treats separated undeformed surfaces. Without an actual deformation δ, the separation mathematically is equal to negative deformation $H = -\delta$ at a given point in 3D.[82] This translates to

$$F_{pull-out}(H = 0) = -2\pi R V_0 = -F_{adhesion} \tag{28}$$

an external pulling force at the point of zero separation is required to balance the attractive adhesive force, favoring the contact of both surfaces, while separating the particle from the surface.[78, 80]
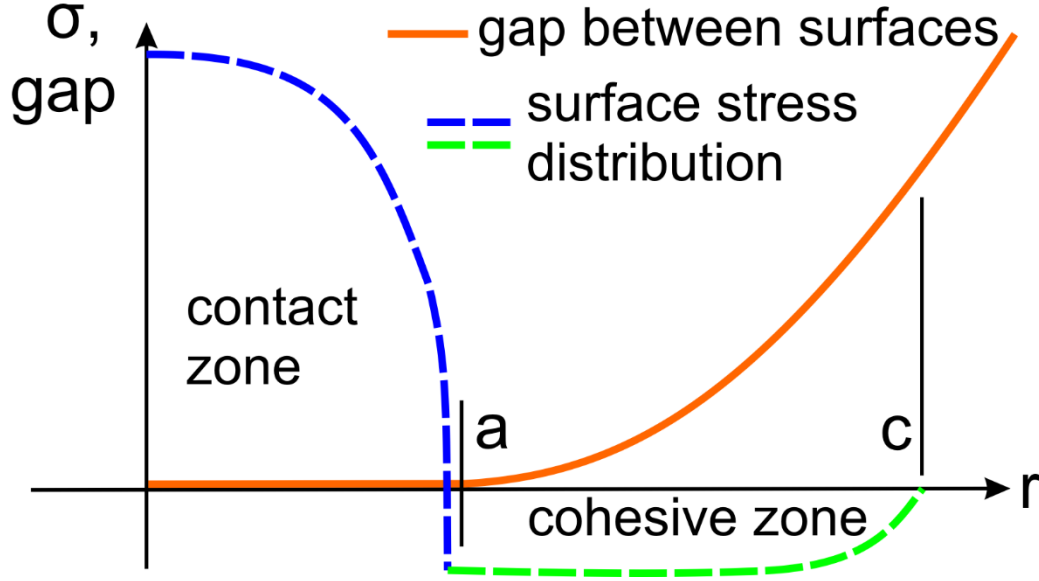
Figure 10   Schematic depiction of the contact geometry discussed in the DMT theory. In the contact zone ($r \leq a$) the gap or separation H is zero and the contact stresses (blue dashed line) follow the Hertzian theory. Outside the contact zone, there is a distinct, cohesive zone ($a \leq r \leq c$), in which attractive forces between particle and surface are causing an additional stress field (green dashed line) depending on the gap size. Recreated in analogy to [82].

The deformation of the particle inside the contact area and the according compressive stress profile are assumed not to change in the presence of the additional interaction potential, so Hertzian equations are still valid, i.e. $\delta_{Hertz}(a) = \delta_{DMT}(a)$ with contact radius *a*. But the overall acting force $F_{DMT}(a)$ is the sum of the externally applied load force *F(a)* plus the adhesion force acting outside the contact area $F_{ext}(a)$.[82] This finally results in:

$$\delta_{DMT}(a) = \delta_{Hertz}(a) = \frac{a_{total}^2}{R} \tag{29}$$

$$a_{total}(F_{total}) = a_{Hertz}(F_{appl.load} + F_{adhesion}) = \sqrt[3]{\frac{R}{E_{tot}}(F_{appl.load} + 2\pi R\gamma)} \tag{30}$$

III.2.4. Validity, Boundary Conditions and Transition of JKR and DMT Theory

Both the JKR and the DMT theory include attractive interactions to the contact deformation problem but take two contrary approaches. However, both base on the Hertzian description of contact mechanics and both transition back to the Hertzian equation when the energy of adhesion is zero. Due to their differing assumptions while deriving, it

depends on the experiment or application problem at hand which theory should be consulted.

First of all for both theories, the area over which the adhesion forces are acting must be sufficiently big so that any influence at all is present. In the case of DMT, it is assumed that attractive, adhesive stresses do not contribute to any deformation.[80, 82] Accordingly, the contact stresses within the contact zone have to be much higher than the adhesive stress in the cohesive zone. (see Figure 10) A transition criterion for the necessary interaction distance $\delta_{interaction}$ can be defined from the DMT equations to[82]

$$\delta_{interaction} \gg \left(\frac{\pi^2 \gamma^2 R}{K^2}\right)^{1/3} \tag{31}$$

Equation 31 may also be rewritten in the picture of Figure 10 so that $c \gg a$. Since both, the gap between sphere and plane as well as the used Lennard-Jones interaction potential, are exponential in nature the right-hand side of equation 31 needs to be sufficiently small for DMT to be valid. Therefore, DMT should be considered for contact conditions with small contact radii, existing but rather low adhesion and highly incompliant, stiff materials.

A similar argument can be made for JKR theory: considering the situation of balancing compressive and tensile stress at zero load, combined with the flat punch interaction range δ_{fp} in JKR while peeling the two surfaces apart. Including the energy balancing approach from JKR aiming for energy minimization in the system we end up with:[82]

$$\delta_{fp} \approx \left(\frac{\pi \gamma^2 R}{K^2}\right)^{1/3} \tag{32}$$

Equation 32 again reflects the balancing idea, that the product of work of adhesion and contact size should match the mechanical properties. Additionally, with the picture of a neck forming, it is easy to imagine that this situation is unlikely to arise with two very uncompliant materials in contact, e.i. metal-metal contact. This leads to the common guideline that JKR theory should be considered for soft materials with higher contact radii and moderate to high adhesion to match the assumptions of the theory.[71, 82]

Comparing the mentioned points and conditions in the two paragraphs above, it is evident that both approaches are describing fundamentally different contact mechanical situations, although they were aiming at a general integration of adhesion in contact mechanics. To aid experimentalist in their choice of the right theory and to establish a

criterion of applicability, Tabor suggested a new parameter or indicator λ by evaluating the ratio of both interaction length δ_{fp} and $\delta_{interaction}$:

$$\lambda \equiv \frac{\delta_{fp}}{\delta_{interaction}} \cong \frac{\delta_{fp}\sigma_0}{\gamma} \cong \frac{\sigma_0}{\left(\frac{\gamma K^2}{\pi R}\right)^{1/3}} \tag{33}$$

By either measuring or educated estimating λ it allows for distinguishing between DMT and JKR, with high values of λ pointing at JKR and small values at DMT. However, this still leaves the void for medium values of λ since both theories should be seen as discrete boundary cases on the λ scale.

In the early 1990s, a new theoretical approach was presented by Maugis aiming at a general picture of contact stresses, deformation and adhesive interactions including also the till now unspecified medium λ conditions.[83] His approach merges ideas from crack mechanics under pressure and the Dugdale approach of constant vertical stresses over a certain distances, including an energy release rate. Since the detailed derivation is long and quite complex (around 120 equation on 27 pages) I will focus on the relevant equations. The force-deformation under adhesive influence can be described according to Maugis by a set of parametric equations[71]:

$$\bar{\delta} = \bar{A}^2 - \frac{4}{3}\lambda\bar{A}\sqrt{m_M^2 - 1}, \quad \bar{F} = \bar{A}^3 - \lambda\bar{A}^2\left(\sqrt{m_M^2 - 1} + m_M^2 \arctan\sqrt{m_M^2 - 1}\right), \tag{34}$$

$$\bar{A} = \frac{a}{\sqrt[3]{\pi\gamma R^2/E_{tot}}}, \qquad \bar{F} = \frac{F}{\pi\gamma R}, \qquad \bar{\delta} = \frac{\delta}{\sqrt[3]{\pi^2\gamma^2 R/E_{tot}^2}}, \tag{35}$$

$$\frac{\lambda\bar{A}^2}{2}\left[\sqrt{m_M^2 - 1} + (m_M^2 - 2)\arctan\sqrt{m_M^2 - 1}\right] \tag{36}$$

$$+ \frac{4\lambda^2\bar{A}^2}{3}\left(1 - m_{M+}\sqrt{m_M^2 - 1}\arctan\sqrt{m_M^2 - 1}\right) = 1$$

In this bunch of equation, all variables have the same meaning as before, but the Tabor parameter λ was modified or specified so that $\sigma_0 = 2.06\gamma/D_0$, with "$D_0$ being a typical atomic dimension" and "m_M being the ratio between the contact radius a and the annular region, where the adhesion is taken into account".[71] As already suggested by Tabor, also Maugis equation converge to DMT ($\lambda\to0$), to JKR ($\lambda\to\infty$) and Hertz ($\gamma\to0$). With his calculation, Maugis showed that JKR and DMT are not fundamentally different but somewhat the limiting cases within one universal theory. One drawback of equations 34 -

36 is that they directly depend on each other and therefore are only analytically solvable. This renders them rather unhandy to describe force – distance/-deformations experiments.

III.2.5. A General Equation for Fitting Contact Area vs. Load Measurements – Carpick, Ogletree, Salmeron

The difficulties mentioned above to apply the Maugis equations to experimental force-deformation data, for example, recorded by atomic force microscopy, was circumvented by Carpick, Ogletree, and Salmeron (COS) by introducing an approximation to Maugis theory.[84] They noticed that a simple transition equation between DMT and JKR according to Maugis theory can be derived only involving the contact radius a, the contact radius at zero load a_0 and the force of adhesion F_{adh}. The respective equations for JKR and DMT are:

$$F_{adh,JKR} = -\frac{3}{2}\pi\gamma R \qquad\qquad F_{adh,DMT} = -2\pi\gamma R \qquad (37)$$

$$a_{0,JKR} = \left(\frac{6\pi\gamma R^2}{E_{tot}}\right)^{1/3} \qquad\qquad a_{0,DMT} = \left(\frac{2\pi\gamma R^2}{E_{tot}}\right)^{1/3} \qquad (38)$$

$$\frac{a}{a_{0,JKR}} = \left(\frac{1+\sqrt{1-F/F_{adh,JKR}}}{2}\right)^{2/3} \qquad \frac{a}{a_{0,DMT}} = \left(1-F/F_{adh,DMT}\right)^{1/3} \qquad (39)$$

With a close look at the equations 39 a transition parameter α varying from 0 to 1 can be introduced resulting in the general equation:

$$\frac{a}{a_{0,\alpha}} = \left(\frac{\alpha+\sqrt{1-F/F_{adh,\alpha}}}{1+\alpha}\right)^{2/3} \qquad (40)$$

While this simple equation can describe an arbitrary force – deformation, or in this notation a contact radius, measurement it does not yet give access to the involved mechanics or adhesion. However, COS found in numerical simulations that there is a direct correlation between their α and λ which can be fitted according to:

$$\lambda = -0.924\ln(1-1.02\alpha) \qquad (41)$$

$$\overline{F_{adh}}(\lambda) = -\frac{7}{4}+\frac{(4.04\lambda^{1.4}-1)}{4(4.04\lambda^{1.4}+1)} \qquad (42)$$

$$\overline{a_0}(\lambda) = 1.54+0.279\left(\frac{2.28\lambda^{1.3}-1}{2.28\lambda^{1.3}+1}\right) \qquad (43)$$
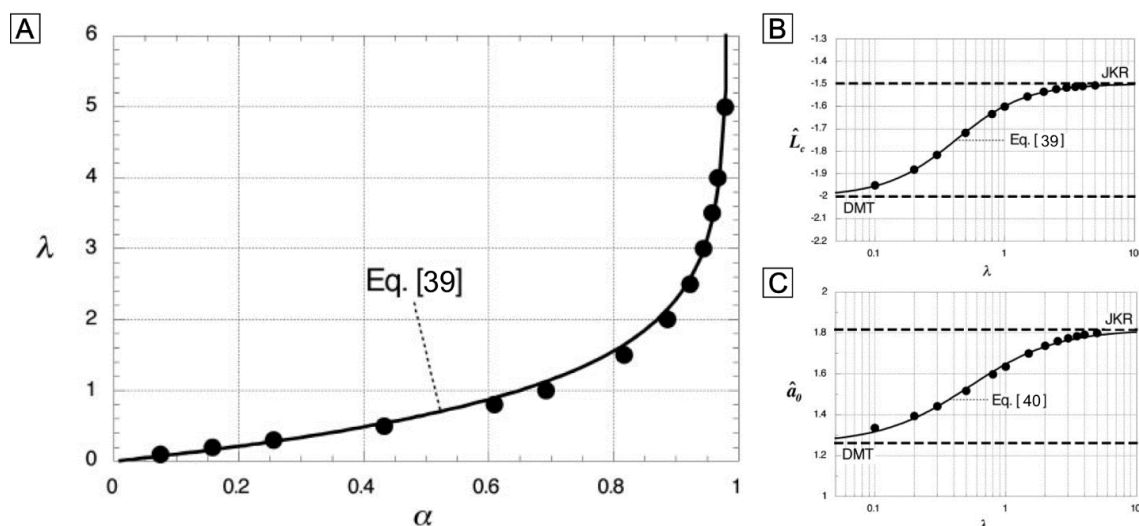
Figure 11   Numerical calculations for the dependencies of A) λ and α, B) $\widehat{L_c}$ (abbreviation in the original paper) here $\overline{F_{adh}}$ and λ, C) $\overline{a_0}$ and λ with their least error fits following the equations stated in the insets. Reprinted with permission.[84]. Copyright 1999 Academic Press (Elsevier).

Furthermore, the dependencies of the Maugis normalized force and the contact radius, as introduced in equation35, with the Tabor/Maugis parameter, can be fitted by with reasonable accuracy (within 1%) with equations 42 and43.[84] Figure 11 depicts the results from numerical simulations and the applied fits following equations 41 to43. Fitting the results of measurement with equation 40 for $\alpha - F_{adh,\alpha}$ and $a_{0,\alpha}$ might be constraint to experimental observable values – then enables determination of work of adhesion first using equation 41, then 42 and finally 35 for $\bar{F}$. Knowing γ and applying equation 43(43 gives the elastic modulus according to equation 35 for $\bar{A}$.[84] Overall, the COS model represents an easily implementable concept for practical purposes omitting complex analytical simulations.

III.2.6. A novel contact model for AFM indentation experiments on soft spherical particles

So far, the contact models presented focus on the contact of two curved half-spaces in contact. In consequence, the applied stresses and strains vanish at a certain distance from the surface, as already introduced by Hertz. However, taking a look at a classical Newtonian free body diagram, an acting force on an object would translate to a movement of the object if it is not blocked on the opposing side. If the object is physically clamped and can not slip away the applied force will be counteracted by an elastic restoring force partially from the load side and partially from the substrate side, where the translational movement is hindered. With that in mind, one should consider two contact mechanics locations, at the

indenter and at the substrate side with its respective contact geometries and interactions potentials. The researches of Glaubitz et al. investigated these issues with respect to AFM indentation experiments on soft hydrogel particles.[85] They developed a theoretical approach based on the contact mechanics models presented above and tested the potential influence on the accuracy of E-modul determination.

The geometrical situation at consideration is a three-body problem, depicted in Figure 12, with four different kinds of forces acting and balancing each other. As the headline of the chapter suggests the focus lies on an AFM probe acting on a soft sphere located on a solid substrate. Therefore, the elastic modulus of the indenter and substrate (E_1 and E_3) is assumed to be way higher than from the sample sphere E_2. While indenting, the AFM technique is only able to record the overall performed deformation δ, while here one should consider the combination of top deformation δ_{12} and a bottom deformation δ_{32}^*. The contact mechanics involved between body 1 and 2 is assumed to be Hertzian (c.f. chapter III.2.1) and between body 2 and 3 following JKR (c.f. chapter III.2.2). The latter opens the argument that a very soft, adhesive particle sitting on the surface may be pre-deformed ($\delta_{g\gamma}$) due to gravity force of the particles acting as a load force in the sense of JKR. This
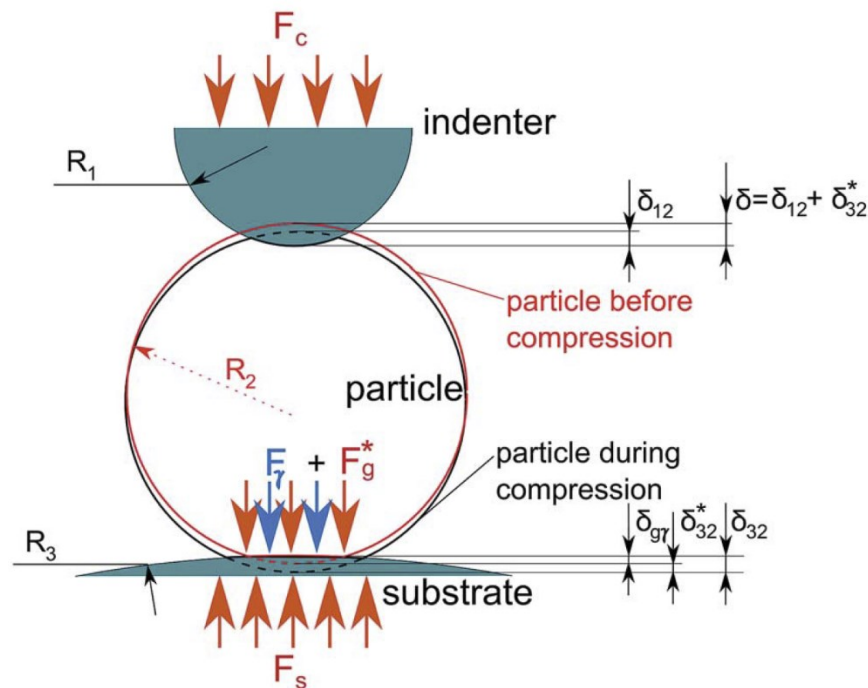
Figure 12 Schematic setup of the three-body contact problem of a particles of interested clamped between two surfaces, each with a variable radius of curvature R. Four acting forces – F_c applied external cantilever load force, F_γ adhesive interaction force, F_g force of gravity, F_s substrate force - are considered with the orientation indicated by the red and blue arrows. The following deformations δ on top and bottom are indicated on the right hand. Reprinted with permission.[85] Copyright 2014 The Royal Society of Chemistry.

possible pre deformation is not part of the recorded AFM deformation. Hence the total bottom deformation is $\delta_{32} = \delta_{g\gamma} + \delta_{32}^*$ but δ_{32}^* needs to be taken into account for AFM force curve modeling. The most general equation the authors derived including all mention parameters is

$$\delta(F_c) = \delta_{12} + \delta_{32}^* = \left(\frac{3F_c}{4E_2}\frac{1-v_2^2}{R_{12}^{0.5}}\right)^{2/3} + \tag{44}$$

$$+ \left[\frac{3(1-v_2^2)\left(F_c + F_g^* + 3\gamma\pi R_{32} + \sqrt{6\gamma\pi R_{32}(F_c + F_g^*) + (3\gamma\pi R_{32})^2}\right)}{4E_2 R_{32}^{0.5}}\right]^{2/3}$$

$$- \left[\frac{3(1-v_2^2)\left(F_g^* + 3\gamma\pi R_{32} + \sqrt{6\gamma\pi R_{32}F_g^* + (3\gamma\pi R_{32})^2}\right)}{4E_2 R_{32}^{0.5}}\right]^{2/3}$$

which they refer to as *mixed double contact model*. This rather bulky equation is constructed by first the Hertz deformation at the top (c.f. eq.15, 16), second the JKR deformation with a net force of applied and gravity force (c.f. eq.26) and third JKR with only gravity force.

To evaluate the impact of the second contact to the determination of the elastic modulus of the sample E_2 the authors calculated the relative error in modulus ΔE by comparing single Hertz contact with double Hertz contact (eq. 44 without adhesion and gravity). The relative error than only depends on the size difference between the three objects. Introducing the scaling factors α and β as $R_1 = \alpha R_2$ and $R_3 = \beta R_2$ gives

$$\Delta E = \frac{E_{single,Hertz}(\delta) - E_{double,Hertz}(\delta)}{E_{double,Hertz}(\delta)} \tag{45}$$

$$= \left(\frac{(\alpha\beta + \beta)^{1/3}}{(\alpha\beta + \beta)^{1/3} + (\alpha\beta + \alpha)^{1/3}}\right)^{1.5} - 1$$

Figure 13 gives an overview of the expected relative deviations depending on the object's geometry with some experimentally relevant geometries highlighted. The heat map shows the highest variations of up to 100% if the sample particle is sitting on a convex substrate particle with lower radius of curvature than the sample ($0 < \beta < 1$). In the context of mechanical
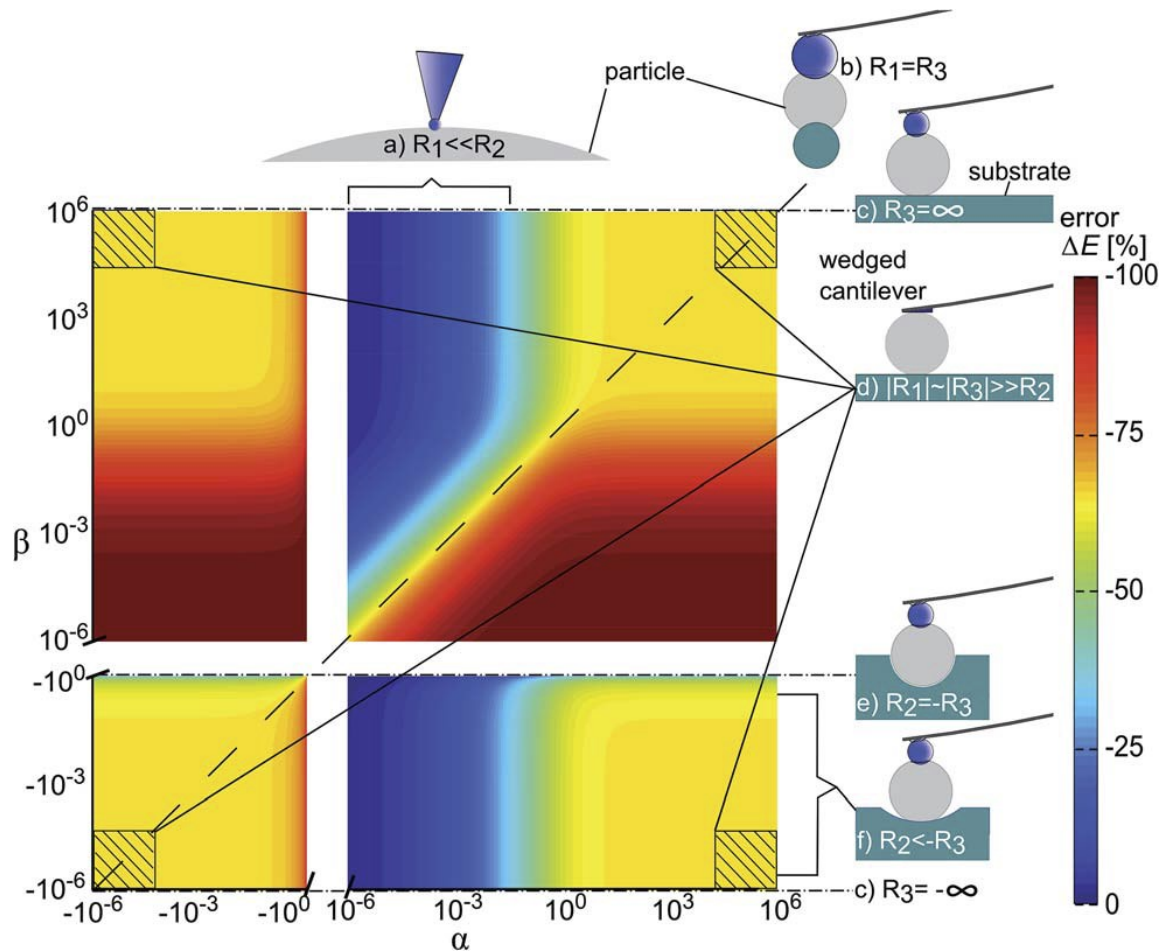
Figure 13 Heat map of the relative error in elastic modulus from single to double Hertzian contact as a function of the three radii of curvature involved. Schematic insets highlight some very prominent special cases of contact. Reproduced with permission.[85] Copyright 2014 The Royal Society of Chemistry.

characterization by AFM the most relevant scenario is depicted in Figure 13 inset c) with the spherical particle resting on a flat substrate ($R_3=\infty$). In case the indenter radius is additionally way smaller than the sample, the situation matches a sharp tip cantilever indenting a microparticle. Theoretically, the error is smallest here below 25% but one has to consider other effects like tip wear or penetration of the soft material without an elastic repulsive force. If the size of the indenter increases to one-tenth of the sample or the same size, the error quickly goes up to 30 – 65% and levels at around 70%.

Despite the shown significant possible errors, this theory is until the present date rather slowly recognized in the scientific community. Also, without doubting any of the theoretical work presented and the purely logic picture they derive the theory from, the practical validation within the paper is relatively weak. Their only argument is that the double contact fits, using more independent parameters, describes the measured force-deformation behavior of a PEG hydrogel better than the single contact one.[85] Additionally, from an experimentalist point of view, the most common materials used for substrates and,

especially in the case of soft materials, colloidal probes are glass or silica. If one considers a JKR contact on the bottom one should also consider a JKR contact at the top since both surfaces have very similar surface energies. Hence, a double JKR model should be considered, which is missing in the publication, but very easily derived from the equations at hand as:

$$\delta(F_c) = \delta_{12} + \delta_{32}^* = \tag{46}$$

$$\left[\frac{3(1-\nu_2^2)}{4E_2}\right]^{2/3}\left[\left(\frac{F_c + F_g^* + 3\gamma\pi R_{12} + \sqrt{6\gamma\pi R_{12}(F_c + F_g^*) + (3\gamma\pi R_{12})^2}}{R_{12}^{0.5}}\right)^{2/3}\right.$$

$$+ \left(\frac{F_c + F_g^* + 3\gamma\pi R_{32} + \sqrt{6\gamma\pi R_{32}(F_c + F_g^*) + (3\gamma\pi R_{32})^2}}{R_{32}^{0.5}}\right)^{2/3}$$

$$\left. - \left(\frac{F_g^* + 3\gamma\pi R_{32} + \sqrt{6\gamma\pi R_{32}F_g^* + (3\gamma\pi R_{32})^2}}{R_{32}^{0.5}}\right)^{2/3}\right]$$

III.3.   References

[63] J.-F. Gauvin, *Renaissance Quarterly* **2012**, *65*, 564.

[64] A. Bogner, P.-H. Jouneau, G. Thollet, D. Basset, C. Gauthier, *Micron* **2007**, *38*, 390.

[65] D. B. Williams, C. B. Carter, "The transmission electron microscope", in *Transmission electron microscopy*, Springer, 1996, p. 3.

[66] N. Tanaka, *Science and technology of advanced materials* **2008**, 9, 014111.

[67] G. Binnig, H. Rohrer, C. Gerber, E. Weibel, *Physical review letters* **1982**, *49*, 57.

[68] G. Binnig, C. F. Quate, C. Gerber, *Physical Review Letters* **1986**, *56*, 930.

[69] N. Jalili, K. Laxminarayana, *Mechatronics* **2004**, *14*, 907.

[70] C. P. Green, H. Lioe, J. P. Cleveland, R. Proksch, P. Mulvaney, J. E. Sader, *Review of Scientific Instruments* **2004**, *75*, 1988.

[71] H.-J. Butt, B. Cappella, M. Kappl, *Surface Science Reports* **2005**, *59*, 1.

[72] H. Hertz, *Journal für die reine und angewandte Mathematik* **1882**, 1882, 156.

[73] H. Hertz, D. E. Jones, G. A. Schott, "*Miscellaneous papers*", Macmillan and Company, 1896.

[74] G. R. Kirchhoff, "Vorlesungen über mathematische physik: mechanik", Teubner, 1876.

[75] A. D. Roberts, "Ph.D. disseration", Cambridge University, England, 1968.

[76] K. Kendall, "The stiffness of surfaces in static and sliding contact", University of Cambridge, 1969.

[77] K. L. Johnson, K. Kendall, A. D. Roberts, *Proceedings of the Royal Society of London Series a-Mathematical and Physical Sciences* **1971**, 324, 301.

[78] B. V. Derjaguin, V. M. Muller, Y. P. Toporov, *Journal of Colloid and Interface Science* **1975**, *53*, 314.

[79] J. A. Greenwood, *Tribology Letters* **2007**, *26*, 203.

[80] V. M. Muller, B. V. Derjaguin, Y. P. Toporov, *Colloids and Surfaces* **1983**, *7*, 251.

[81] B. Derjaguin, *Kolloid-Zeitschrift* **1934**, *69*, 155.

[82] E. Barthel, *Journal of Physics D: Applied Physics* **2008**, 41, 163001.

[83] D. Maugis, *Journal of Colloid and Interface Science* **1992**, 150, 243.

[84] R. W. Carpick, D. F. Ogletree, M. Salmeron, *Journal of Colloid and Interface Science* **1999**, *211*, 395.

[85] M. Glaubitz, N. Medvedev, D. Pussak, L. Hartmann, S. Schmidt, C. A. Helm, M. Delcea, *Soft Matter* **2014**, *10*, 6732.

IV. Synopsis

IV.1. Outline

After introducing the framework of this study with its relevance for research and applied science presented in chapter I, chapters II and III provided an overview of commonly used techniques, principles, applications and theoretical background in this broad research field.

New results on contact mechanics and adhesion of polymeric soft matter particles in aqueous environment are now presented in detail through the chapters V to VII. Chapters V and VI introduce studies I contributed significantly to on mechanical changeable hydrogel particles. A novel approach to prepare and characterize bio-inspired mussel foot proteins for high underwater adhesion surfaces is presented in chapter VII. This chapter gives a short summary of the three individual peer-reviewed studies and covering the essentials.

IV.2. Tuning the Mechanical Properties of Hydrogel Core-Shell Particles by Inwards Interweaving Self-Assembly

The role of material's mechanical properties is of key importance for interactions with cells, tissues, or in other applications, especially for soft matter like hydrogel particles. Known concepts to tune mechanical properties for hydrogels can be categorized into two strategies: on the one hand by adjusting the crosslinking density in a permanent chemical procedure or by polymerizing a second network within the first, so-called interpenetrating polymer networks. On the other hand, stimuli-responsive hydrogels can be employed, which can change their swelling degree and thus their mechanical properties. They give access to a range of different features but simultaneously potentially unfavorable cross-talk effects to the application. In this study, we followed the approach of inwards interweaving self-assembly, a precise post-treatment technique available for hydrogels. This concept was pioneered by the group of Prof. Trau with whom we cooperated and his student Mr. Pan prepared all the particles investigated. Combining poly(allylamine) in an anhydrous organic solvent with agarose hydrogel microparticles results in a diffusion-limited absorption into the hydrogel network. The sequential addition of poly(styrenesulfonic acid) triggers complexation with the absorbent, and both polymers form an inwards interwoven
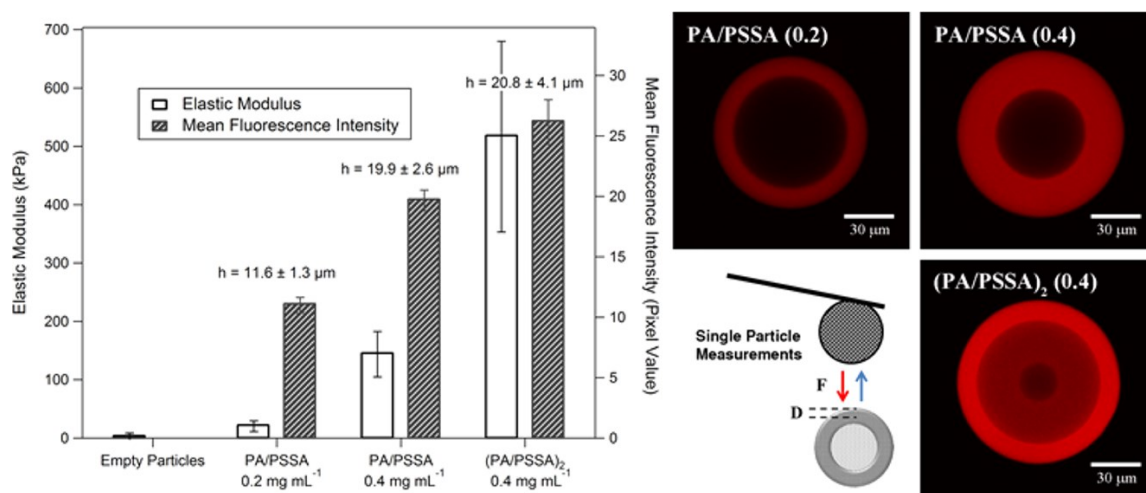
Figure 14 Survey of the results on core-shell microgel particles from inwards interweaving self-assembly. The plot to the left summarizes the correlation between elastic modulus, shell thickness, and mean fluorescence intensity, which is a measure for the polymer density. CLSM micrographs to the right demonstrate three examples of single and double-shell microgels prepared with varying incubation conditions. Reprinted with permission.[86] Copyright 2016 American Chemical Society.

self-assembled, concentric layer from the surface of the particles. Controlling the polymer concentration or incubation time allows accurate handling of the shell thickness from some μm up to complete fill-up in a single modification step. The goal of this work was to analyze the correlation between shell thickness, density, and the number of layers with changes in mechanical characteristics. Colloidal probe atomic force spectroscopy measurements were performed to access the effective elastic modulus of such core-shell particles with high sensitivity. For single shelled microparticles the compliance could be tuned from 10 to 190 kPa by varying the shell thickness between 10 and 24 μm. This reduction in compliance can be anticipated to be accompanied by an increase in polymer density within the shell. Utilizing fluorescently labeled adsorbents, we confirmed this correlation through quantitative fluorescence measurements. Both the effective elastic modulus and the density can be further increased by addition of a second shell layer within the first following the same concept. This demonstrates the positive correlation between these two quantities for our core-shell particles. Since the employed self-assembly approach is not limited to PA/PSSA, more functional groups can be incorporated from poly(ethylene imine), poly(acrylic acid), and others. Further, the presented work may be used as a blueprint for hydrogel systems opening new possibilities in the field of mechanobiology with rationally designable diffusivity or stiffness-dependent cellular uptake studies.

IV.3. Core-Shell Microgels with Switchable Elasticity at Constant Interfacial Interaction

Hydrogel particles, with designed and tunable mechanical properties, as presented in chapter V, are valuable platforms in many research activities. However, they lack stimulus responsiveness. Besides, the application of chemically different shell-forming polymers alters the initial interaction properties of the original hydrogel. Addressing these limitations, we designed and characterized core-shell microgels able to switch their elasticity while keeping the interfacial interaction potential unaffected.
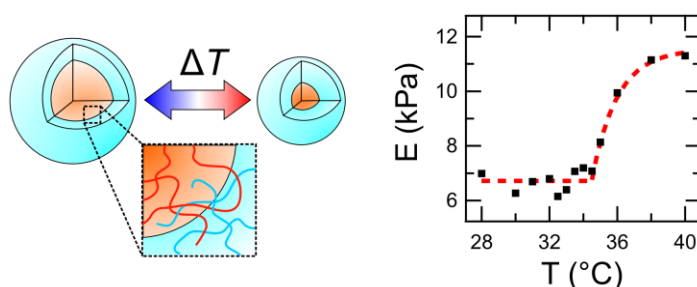
Figure 15   The conceptual picture of temperature-responsive core-shell microgel particles is presented on the left, highlighting the entanglements of both polymer networks at their interface. A typical elastic modulus versus temperature profile of these core-shell particles shows the switchability of them. Reprinted with permission.[87] Copyright 2016 American Chemical Society.

Prof. Fery and I developed the concept of such core-shell microgels based on poly(N-isopropyl acrylamide) (pNIPAAm) which is well-known and studied for its thermo-reversible volume phase transition around 32°C. Above this temperature, the solvent quality of water is poor, forcing a deswelling and densification of the polymer network. This is reflected in a change of the mechanical and adhesion properties towards other objects. With our core-shell approach, we aim to transfer the mechanical response to a *per se* passive shell, which additionally should mask the change in hydrophilicity. With that in mind, my cooperation partners of the Seiffert group synthesized a tailored UV-cross-linkable poly(acrylamide) (pAAm) which is chemically very similar to pNIPAAm. Controlling the delay between core encapsulation and photo-crosslinking of the shell should allow some diffusion of pAAm within the core network. The interpenetration of both polymers at their interface is postulated to transmit the mechanical response to the shell.

Experimentally such microgels were realized by my cooperation partners of the Seiffert group in two separated droplet microfluidic experiments. Plain NIPAAm droplets with narrow size distribution were prepared in a single flow-focusing cross-junction and crosslinked with *N,N'*-methylenebis(acrylamide). These microgel particles, after

purification, were then injected in a second droplet microfluidic devices with a double flow-focusing cross-junction geometry. At the first junction, the particles are surrounded by an aqueous solution of pAAm. At the second junction core-shell droplets are created into paraffin oil followed by photo-crosslinking of the shell on-chip. With this setup, we prepared two batches of core-shell particles, one with thin and soft shell (B1) and the other with thick and stiffer shell (B2).

I characterized both batches as well as plain particles of both materials with simultaneous temperature-dependent optical light microscopy and colloidal probe atomic force spectroscopy. Size determination of core and core-shell radii revealed for both batches the responsive behavior of pNIPAAm core. However, the deswelling of the encapsulated cores is reduced compared to the unconstrained plain ones. Differences for the batches were observed in the overall size of the particles. While B1 particles shrink in volume, the total radius of B2 stays unaffected. Further, the absence of a void within the particles at higher temperatures is an indication for the proposed interconnection of core and shell leading to stretching of the shell. The surface elastic properties of the core-shell particles followed a similar temperature dependence as plain pNIPAAm particles. However, the $10 - 60\%$ increase E-modul for core-shell particles is significantly lower compared to 3 orders of magnitude changes for the plain core. The same measurements confirmed that the adhesion of the core-shell particles and the colloidal probe are practically constant with temperature.

IV.4. Bio-Inspired Adhesives – Toward synthetic mussel-foot proteins and resistant high-performance glues

After introducing a novel design of soft polymeric particles, proven to change their surface mechanical properties without affecting their adhesive interaction properties (chapters IV.3 and VI), a new focus was laid on studying underwater adhesion properties searching for high-performance glues. Motivated by the excellent ability of mussels to adhere to many types of surfaces in challenging environmental settings, we took a closer look at this mechanism and the established knowledge in literature. Here, biologists found six different peptide families on the byssal threads of mussels and studies on the adhesion performance of natural mussels indicated a positive correlation with the amount of L-3,4-dihydroxyphenylalanine (Dopa) within the peptide sequence.

We concentrated our studies on the *Mytilus californianus* foot protein (mfp) 1, which is known for a moderate concentration of Dopa but also a very repetitive decapeptide structure. Inspired by the recurring structure of the peptide, the group of Prof. Börner developed a novel polymerization strategy to generate artificial adhesive peptides as closely related to the biological process anticipated. Starting from the decapeptide structure, bearing two tyrosine amino acid groups, Dopa and Dopaquinone moieties can be generated in the presence of tyrosinase, which is almost ubiquitously found in nature. Especially the Dopaquinone is further known to react with thiols to covalently linked cysteinyldopa. Extending the decapeptide structure with cysteine results in an A_2B-like macromonomer (U_2^C) with the intrinsic ability to be enzymatically polymerized, as it might occur in nature, opening the path to potential low cost, on-demand, underwater adhesive.

To investigate the polymerization hypothesis, we also reduced the reaction complexity in a model AB-macromonomer by substituting one tyrosine with serine combined with a cysteine extension (U_1^C). In the presence of tyrosinase both monomers polymerized entirely within 10 minutes. MALDI-TOF-MS, GPC and SDS PAGE analyses of the polymers revealed for both a low molecular weight species around 30 kDa or a degree of polymerization of around 20 and additionally a high molecular weight species of ~530 kDa or 260 repetition units. In-depth characterization of the linking reaction was performed by HPLC kinetic studies on the dimerization of monofunctional model unimers. Although intermediated disulfide dimers were evident, the overall reaction balance favors the cysteinyldopa link with full conversion after 5 minutes.

Further, we analyzed the coating capabilities of both artificial peptides in QCM-D experiments. Both adsorbed continuously over 5h in buffer solution on different surfaces, forming a multilayered structure, which is a typical feature for protein adsorption processes. The QCM-D data suggested layer thicknesses in the range of 25 to 35 nm. Coating stability, as it is of high importance for mussels in nature, was tested by extensive rinsing the deposited layers with saline (599 mM NaCl) and hypersaline (4.2 M NaCl comparable with water from the Dead Sea) solutions. Thereby, only minor mass losses of 1 to 7% were observed emphasizing the resistance also to very harsh conditions. All the experiments mentioned above were conducted with almost no exception by Justus Horsch.

Finally, the adhesion performance of these coatings was examined with detailed variations of contacting time and applied contact pressure by colloidal probe atomic force spectroscopy. To enable theoretical descriptions of the measurement data of a micron

particle in contact with nm thin layer, an advanced model was derived accounting for multiple adhesions moieties being released sequentially. Work of adhesion per unit area revealed higher values for the linear AB-like polyU$_1^C$ compared to the anticipatively branched A$_2$B-like polyU$_2^C$ reaching their, on average, maximum values with 3.6 mJ m^{-2} and 0.9 mJ m^{-2}, respectively. Therefore, the linear polyU$_1^C$ exceeds adhesion performance reported for biological mfp-1 for all conditions investigated. Further, it matches the work of adhesion for commercially available adhesive proteins extracted from mussels, which are additionally specially formulated, as tested under the same conditions in reference experiments. Combining all these attributes, these artificial proteins offer a valuable platform for next-generation universal, natural glues.

IV.5.   Personal contributions

Since all presented publications in this thesis are joint work of multiple scientists, I want to highlight and clarify my personal contributions for each individual paper. My focus in all projects is located in the experimental work with AFM, the preparation of samples therefore, the corresponding data evaluation, and the discussions and exchange of ideas on how to proceed within the project. All individual contributions of the authors to an article are detailed below.

Chapter V is published in ACS Applied Materials & Interfaces with the title "**Tuning the Mechanical Properties of Hydrogel Core-Shell Particles by Inwards Interweaving Self-Assembly**" authored by Houwen M. Pan, Maximilian Seuss, Martin P. Neubauer, Dieter W. Trau, and Andreas Fery.

I guided and introduced Houwen to the technique of colloidal probe AFM force spectroscopy during his DAAD research stay at the University of Bayreuth. Further, I introduced him to the complex task of the AFM data evaluation and supported him in many discussions and the process of writing the manuscript. All synthesis and experiments were conducted by Houwen as well as most of the initial manuscript work. Martin supported us both with his experience in AFM on soft particles. Dieter and Andreas supervised the project, guided the work in many in-depth discussions, and gave valuable notes to improve and finalize the manuscript.

Chapter VI is published in ACS Applied Materials & Interfaces with the title "**Core-Shell Microgels with Switchable Elasticity at Constant Interfacial Interaction**" authored by Maximilian Seuss, Willi Schmolke, Astrid Drechsler, Andreas Fery, and Sebastian Seiffert.

I performed all the physical-chemical analytic experiments and their analysis. The manuscript was written and edited by myself based on a very early version from Willi and Sebastian. Willi performed the synthesis of the non-standard polymeric and monomeric chemicals used and their characterization. He also conducted the microfluidic experiments. Astrid supported me during the process of writing the manuscript and helped to clarify and specify the results presented in the paper. The theoretical picture developed at the end of chapter VI.3.3 was an achievement of all authors. Andreas and Sebastian supervised the project, supported both me and Willi in the practical work with precious insights and in advancing the manuscript to a high-end level.

Chapter VII is published in Angewandte Chemie International Edition and Angewandte Chemie with the title "**Polymerizing Like the Mussels Do: Towards Synthetic Mussel Foot Proteins and Resistant Glues**" authored by Justus Horsch, Patrick Wilke, Matthias Pretzler, Maximilian Seuss, Inga Melnyk, Dario Remmler, Andreas Fery, Annette Rompel, and Hans G. Börner.

I performed most of the adhesion measurements with CP-AFM and film thickness investigation of the protein coatings. I developed the extension of the theory of adhesive failure by Carpick, Ogletree, and Salmeron for multiple, sequential rip-off events and performed all data analysis involved with the adhesive properties. I supported Justus from the beginning of the writing process with plenty of notes to improve the manuscript. Justus performed most of the synthesis presented as well as the investigations of the reaction mechanism, including the polymer analysis. All QCM-D experiments were conducted and evaluated by him. Justus wrote most of the manuscript. Patrick had the original idea of the project and made the first proof of concept experiments. Matthias and Annette provided the recombinantly expressed tyrosinase used in the experiments. Inga took over the CP-AFM experiments during the revision period and performed the investigations on pH and surface chemistry dependence, which unfortunately had only a minor role in the publications. Dario supported Justus during the revisions of the manuscript and performed advanced MALDI-TOF-MS experiments. Andreas and Hans supervised the project, added valuable feedback

at all times and managed the long process of revisions till publication with their vast experience

References

[86] H. M. Pan, M. Seuss, M. P. Neubauer, D. W. Trau, A. Fery, *ACS Applied Materials & Interfaces* **2016**, *8*, 1493.

[87] M. Seuss, W. Schmolke, A. Drechsler, A. Fery, S. Seiffert, *ACS Applied Materials & Interfaces* **2016**, *8*, 16317.

V. Tuning the Mechanical Properties of Hydrogel Core-Shell Particles by Inwards Interweaving Self-Assembly

The following chapter is in its entirety based on the research article of H. M. Pan, myself and others published in *ACS Applied Materials & Interfaces*, Volume 8, Issue 2, Pages 1493 -1500 in 2016.[86] It is reprinted with permission while the copyright is with the American Chemical Society 2016. All schemes and figures are used as published as well as almost the entire text is reused. It was modified in some sections to be integrated into this thesis and expanded by content initially published in the connected Supporting Information.

V.1.   Introduction

Hydrogel particles and capsules are commonly employed in cosmetics,[88] biocatalysis,[89] agriculture,[90] and the food industry.[91] In these applications, the tailoring of gel mechanics plays a vital role in encapsulation,[92] rheology control,[93, 94] and targeted delivery.[95] More recently, the mechanical analysis of hydrogel particles has burgeoned as an area of research in mechanobiology,[96] particularly for intracellular delivery of biomolecules.[97-99] Correlation studies between the mechanical properties of hydrogel particles and cellular uptake have revealed that particle elastic modulus plays a critical role in successful particle uptake by cells.[100] Separate investigations carried out by Banquy et al. and Liu et al. have shown that hydrogel particles with elastic moduli in the ranges of 30−140 and 15−35 kPa are internalized more efficiently by RAW 264.7 macrophages[101] and HepG2 cells,[102] respectively. Both studies highlight that soft hydrogel particles with modulus on the order of tens or hundreds of kilopascals are preferentially taken up by cells. This was attributed to a lower susceptibility of softer particles to membrane wrapping during the cellular uptake process.[103] Thus, mechanical properties have become a key parameter in the systematic design of hydrogel-based delivery vectors to achieve successful targeted delivery of drugs.

Recently, we have demonstrated the formation of micrometer-thick polymeric shells and multi-density compartments within agarose particles via the inwards buildup[104] and inwards interweaving self-assembly technique.[105] Unlike layer-by-layer (LbL) polyelectrolyte self-assembly[106] or other encapsulation techniques,[107, 108] the inwards buildup and inwards interweaving self-assembly is not a self-limiting process. Therefore,

shell thicknesses up to tens of micrometers can be achieved from single-polymer incubations and accurately controlled by varying the polymer concentration or incubation period. With this method, "capsule-like" polymer−hydrogel assemblies with a thin polymeric shell (~1 μm) and hydrogel core can be prepared that are suitable as drug delivery vectors.[109] Multicompartment/-shell constructs with a larger shell-to-core ratio can also be created for the separation and compartmentalization of macromolecules.[105] Additionally, the polymeric shell can be assembled with functional polymers to incorporate hydrogel particles with application-specific functionalities. For example, a good variety of polymeric materials can be used with this approach (e.g., PA, PSSA, PEI, PAA, PLL, PGA, and PDADMAC) that are useful for fine-tuning the mechanical properties of hydrogel particles.[110-112] However, to date no study has been done on the mechanical response of hydrogel core-shell particles prepared from the inwards interweaving self-assembly technique.

Atomic force microscopy (AFM) force spectroscopy offers a valuable means of studying mechanical properties on the single-particle level. In colloidal probe-AFM (CP-AFM), a colloidal probe is used in place of a sharp tip.[113] This offers the advantage of an increased interaction area, a well-defined interaction geometry, and reduced localized axial strain, allowing for higher sensitivity and more accurate force measurements.[114, 115] The CP-AFM technique has been successfully utilized for the mechanical characterization of planar polyelectrolyte films,[116] hydrogel capsules,[117, 118] and particles.[119, 120] The sample elastic modulus is evaluated by applying either the Hertz model for full spherical particles[121] and planar substrates[122] or the Reissner model for thin spherical shells.[123, 124]

In this work, we demonstrate how the inwards interweaving self-assembly technique can be utilized as a facile approach for modifying the mechanical properties of hydrogel core-shell particles. By varying the shell thickness and/or layer number, the elastic modulus of particles can be tuned in the kilopascal range. Shell thickness was varied by controlling the concentration or incubation period of poly(allylamine) (PA) and the layer number by controlling the number of poly- (allylamine)/poly(styrenesulfonic acid) (PA/PSSA) depositions. The CP-AFM technique was used to produce high-resolution force−deformation curves which were evaluated with the Hertz model to determine the effective elastic modulus of core-shell particles. The core is agarose, and the shell is comprised of a PA/PSSA−agarose complex. The effective elastic modulus refers to the resultant modulus from both core and shell components. Furthermore, finite element

analysis of particles with different core-to-shell ratios was performed to validate the use of the Hertz model on core-shell particles. The polymeric shell density of core-shell particles was determined by fluorescence quantitative measurements of fluorescent shells. Combining CP-AFM studies and fluorescence quantitative measurements, we were able to elucidate the correlation between the elastic modulus of hydrogel core-shell particles, polymeric shell density, shell thickness, and layer number.

V.2. Experimental Section

Materials:

Fluorescein isothiocyanate (FITC), tetramethylrhodamine isothiocyanate (TRITC), disuccinimidyl suberate (DSS), sorbitan monooleate (Span 80), 1-butanol anhydrous 99.8%, dimethyl sulfoxide anhydrous 99.9% (DMSO), low gelling point agarose, and mineral oil were purchased from Sigma. Poly(allylamine) (PA; 10% solution in water; M_w = 65000 g mol^{-1}) and ADOGEN 464 were purchased from Aldrich. Poly(styrenesulfonic acid) (PSSA; 30% solution in water; M_w = 70000 g mol^{-1}) was purchased from Polysciences. Chloroform, absolute ethanol, and PBS buffer were purchased from BDH Chemicals. All materials were used as received.

Preparation of Agarose Microparticles by Mechanical Stirring:

A 2% (w/v) low-melting agarose was prepared with deionized H_2O and kept molten at a temperature of 50 °C. All other reagents and equipment used were prewarmed and kept at a temperature of 50 °C. A 200 μL aliquot of molten agarose was added to 4800 μL of mineral oil containing 0.1% Span 80 and stirred vigorously for 10 min to form agarose-in-oil emulsion droplets. The droplets were then cooled in an ice-water bath under stirring for another 10 min to allow solidification of the molten agarose droplets into agarose microparticles. The solidified agarose microparticles were further stabilized by placing them at 4 °C for 10 min.

Preparation of Poly(allylamine) and Poly(styrenesulfonic acid) in 1-Butanol:

Poly(allylamine) in 1-butanol was prepared by completely drying the purchased aqueous PA solution at 55 °C, followed by fully saturating 1-butanol with the dried PA. A 1 mL aliquot of the saturated 1-butanol was dried and weighed to determine the actual PA concentration. The solution was then diluted with 1-butanol to prepare a 1 mg mL^{-1} PA solution. This was used as a stock solution. Fluorescently labeled PA was prepared by dissolving and reacting FITC or TRITC with PA in 1-butanol at a ratio of 1:100

(fluorophore:PA monomer). Poly(styrenesulfonic acid) in 1-butanol was prepared by completely drying the PSSA solution at 55 °C and redissolving in 1-butanol to produce a concentration of 1 mg mL^{-1}. This was used as a stock solution.

Fabrication of Agarose-(PA/PSSA) Core-Shell Particles via Inwards Interweaving Self-Assembly:

To transfer the agarose particles from oil to 1-butanol, the agarose-in-oil suspension was first mixed with an equal volume of ethanol containing 0.5% ADOGEN 464. The mixture was then centrifuged, and the mineral oil and ethanol supernatant were discarded. The pellet containing the agarose particles was washed twice with 1-butanol containing 0.5% ADOGEN 464. ADOGEN 464, methyltrialkyl (C8−C10) ammonium chloride, is a cationic surfactant that was added to prevent dehydration and aggregation of agarose particles in the organic phase. A 200 μL aliquot of agarose microparticles suspended in the organic phase were incubated with 1 mL of the desired concentration of PA in 1-butanol containing 0.5% ADOGEN 464 for 30 min under gentle vortexing, followed by removal of excess polymer by two centrifugation and re-dispersion cycles. Agarose−PA core-shell particles were then produced. The particles were incubated with an excess of PSSA in 1-butanol containing 0.5% ADOGEN 464 for 30 min under gentle vortexing, followed by removal of excess polymer by two centrifugation and redispersion cycles. Agarose−(PA/PSSA) core-shell particles were then produced. Additional deposition of PA and PSSA, at the same polymer concentration and incubation time, was performed to produce agarose−(PA/PSSA)$_2$ core-shell particles. The particles were transferred from 1-butanol to PBS by washing them twice with ethanol and then with PBS/ethanol solutions of increasing PBS content (0.01×; 10%, 50%, and 90%) before resuspension in pure 0.01× PBS.

Atomic Force Microscopy Force Spectroscopy:

Prior to force spectroscopy measurements, the spring constant of tipless silicon cantilevers (CSC12 and NSC12, no Al, MikroMasch, Estonia) was determined by employing the thermal noise method.[125] Cantilevers with spring constants 0.93 and 0.26 N m^{-1} were used for measurement. The free-standing end of the cantilevers were then glued with an epoxy resin (UHU Endfest 300, UHU GmbH & Co. KG, Bühl, Germany) and attached with silica particles in the size range of 30−50 μm (Polysciences Europe GmbH,

Eppelheim, Germany) using a micromanipulator (MP-285, Sutter Instrument, Novato, CA, USA).

Force spectroscopy measurements were performed on hydrogel particles suspended in 0.01× PBS solution inside a liquid cell. The liquid cell was precleaned with ethanol and water. An inverted optical microscope (Axio Observer Z1, Zeiss, Oberkochen, Germany) was used to align the cantilever probe with the center of the hydrogel particle. The size of the particles and the thickness of their polymeric shells were also determined from the optical images using ImageJ software (Scion Corp., Frederick, MD, USA). Approach−retract force cycles were then initiated to generate force−deformation (F−D) curves. The approach and retract velocity of the cantilever was 2 μm s^{-1} for all measurements. Reference curves on hard glass substrates were obtained before and after each particle deformation to determine the inverse optical lever sensitivity (InvOLS). F−D curves were fitted with the Hertz model to generate values for the effective elastic modulus of the particle. All data were averaged values of 5−10 measurements carried out on a single hydrogel particle. Only elastic and uniform F−D curves were considered and evaluated using IGOR Pro software (WaveMetrics, Tigard, OR, USA).

Polymeric Shell Thickness and Density Studies:

Confocal laser scanning microscopy images of hydrogel core-shell particles prepared from fluorescently labeled PA were taken. The hydrogel particles ranged from 50 to 140 μm in diameter and were dispersed in 0.01×PBS. The polymeric shell thickness was measured from the confocal images using ImageJ software (Scion), and the mean fluorescence intensity was obtained concurrently from line measurements of the shell thickness. The mean fluorescence intensity corresponds to the density of the polymeric shell. Only confocal images taken under the same fluorescence settings were measured and compared.

Finite Element Analysis:

COMSOL Multiphysics (COMSOL, Burlington, MA, USA) software was used to carry out the finite element simulation. The finite element model is comprised of a rigid sphere in contact with a deformable sphere with a layered structure, simulating the elastic deformation of a hydrogel core-shell particle by a silica colloidal probe (Figure 17 G). Both materials were assumed to be elastic, homogeneous, and isotropic, and contact was assumed to be frictionless. Material properties for the model are elastic modulus $E_{probe} = 68$ GPa, $E_{gel\ shell} = 50$, 100, or 200 kPa, and $E_{gel\ core} = 5$ kPa, Poisson's ratios $\nu_{probe} = 0.19$

and $\nu_{gel} = 0.5$, sphere radius $R_{probe} = 25$ μm, and $R_{gel} = 25$ μm. Four different models were studied: A full particle and core-shell particles with core-to-shell ratios of 1:2 (8.33 μm:16.67 μm), 2:1 (16.67 μm:8.33 μm), and 5:1 (20.83 μm:4.17 μm). The deformable sphere was meshed finer at the area of contact to improve the accuracy of the solution. Deformations were imposed by applying a prescribed displacement on the rigid sphere for values between 30 and 1250 nm. Reaction forces were determined as an output parameter of the finite element simulation, and F−D curves were generated. The finite element solution was then compared with the Hertz analytical solution. F−D curves computed from finite element analysis were fitted with the Hertz model to generate values for the effective elastic modulus of the particle.

Optical and Fluorescence Microscopy:

Phase-contrast and fluorescence microscopy images were recorded using a CCD color digital camera, Retiga 4000R (QImaging, Surrey, Canada) connected to a system microscope (Olympus BX41) with a mercury arc (Olympus HBO103W/2) excitation source. Images were captured with QCapture Pro software (QImaging). Confocal laser scanning microscopy (CLSM) and corresponding bright-field images were captured using a confocal laser scanning microscope, Leica TCS SP8 (Leica Microsystems, Wetzlar, Germany).

AFM:

All force spectroscopy measurements were carried out with an AFM (MFP 3D, Asylum Research, Goleta, CA, USA), combined with a CLSM (LSM710, Zeiss) which is equipped with a 20× and a 63× oil immersion objective. All measurements were performed at room temperature.

V.3.   Results and Discussion

V.3.1. Fabrication of Hydrogel Core-Shell Particles via Inwards Interweaving Self-Assembly (PA/PSSA)

The fabrication steps of shell-thickness-tunable core-shell particles are illustrated in Figure 16. Agarose hydrogel particles were first prepared via water-in-oil emulsion and transferred into the organic solvent 1-butanol (99.8%). The following polymer assembly steps were performed entirely in anhydrous 1-butanol. The particle suspension was
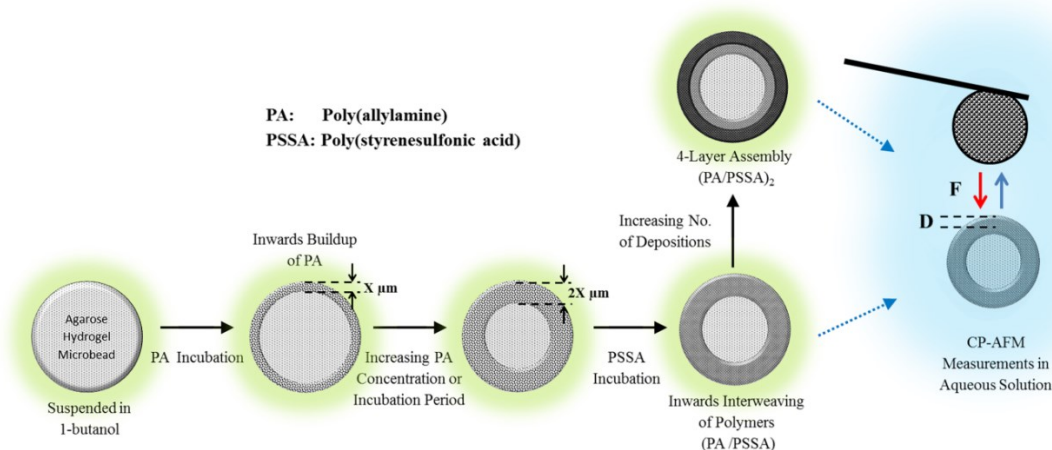
Figure 16   Schematic illustrating the fabrication of agarose-(PA/PSSA) or agarose-(PA/PSSA)$_2$ core-shell particles by inwards interweaving of PA and PSSA. The polymer assembly process was performed in anhydrous 1-butanol. Single-particle force-deformation (F–D) measurements were carried out in aqueous solution via the CP-AFM technique. All graphics represent cross-sections of agarose particles. Reprinted with permission.[86] Copyright 2016 American Chemical Society.

incubated with PA to form well defined, micrometer-thick concentric layers which assemble via inwards diffusion of the PA polymer.[104] The first PA layer was hypothesized to form weakly interacting hydrogen bonds with free -OH groups of agarose. At this stage, the use of anhydrous organic solvent plays a crucial role in stable shell formation as the addition of water will lead to the complete dissolution of the PA-agarose layer. Next, the agarose-PA core-shell particles were incubated with poly(styrenesulfonic acid) (PSSA). The concentration gradient between the polymer-filled organic solvent and the porous PA−agarose matrix also drives the inwards diffusion of PSSA into the porous matrix. This leads to the inwards interweaving of PA and PSSA layers within the hydrogel network, in which PSSA and PA interact electrostatically to form water-stable complexes. A Bronsted acid-base reaction was proposed to be responsible for the formation of stable PA-PSSA complexes, where protonation of amine groups by sulfonic acid groups occurs consecutively during interaction.[126] Unlike the conventional LbL approach, this creates in an organic solvent a "polyelectrolyte-reinforced" agarose backbone with a porous structure. As a result, the self-limiting nature of nanometer-thick poly(allylamine hydrochloride)/ poly(styrenesulfonate) (PAH/PSS) multilayer films does not apply here. Additional depositions of PA/PSSA can be performed to create a multi-density polymeric shell. The soft hydrogel core-shell particles were then transferred into aqueous solution where force spectroscopy measurements were performed to quantify their mechanical properties via the CP-AFM technique. In CP-AFM measurements, the sharp tip of the AFM cantilever is replaced by a colloidal probe. The cantilever probe was optically aligned with the center of

the hydrogel particle to ensure axisymmetric and uniform compression of the particle. Approach-retract cycles were then initiated to generate force−deformation curves.

V.3.2. Mechanics of Particle Deformation

In order to investigate the mechanical properties of our particles, the elastic modulus was determined in the small deformation regime by applying the Hertz model. Hertz theory describes the elastic compression of two isotropic spherical bodies in axisymmetric geometry, neglecting adhesion and friction:[72]

$$F = \frac{4}{3} E R^{1/2} D^{3/2} \tag{47}$$

with

$$\frac{1}{R} = \frac{1}{R_1} + \frac{1}{R_2} \tag{48}$$

$$\frac{1}{E} = \frac{1 - \nu_1{}^2}{E_1} + \frac{1 - \nu_2{}^2}{E_2} \tag{49}$$

where ν is the Poisson ratio. The Poisson ratio was assumed to be 0.5 for incompressible isotropic elastic materials. Here, E and R are the effective elastic modulus and sphere radius, respectively, given in equations 48 and 49. The indices refer to the two objects in contact, the colloidal probe and the soft hydrogel particle. In our study, a silica particle was used as a probe and considered to be nondeformable; thus, its contribution to the combined elastic modulus was negligible. The Hertz model is derived based on the F−D behavior of full and homogeneous spherical particles. Therefore, it was imperative to validate the applicability of the Hertz model for a two-component core-shell system via finite element analysis.

COMSOL Multi-physics Finite Element Methods (FEM) was used to model the elastic deformation of a full particle and core-shell particles with core-to-shell ratios of 1:2, 2:1, and 5:1. (see V.2 Finite Element Analysis) The solutions produced by FEM were compared to the Hertz analytical solution computed with the shell elastic modulus of 100 kPa. Not surprisingly, the F-D curves produced from FEM and the modulus derived from Hertz-fitting both indicated that the FEM solution approaches the Hertz analytical solution for decreasing the core-to-shell ratio as well as decreasing deformations. (Figure 17 C,D) The FEM solution for a full particle and core-shell particle of ratio 1:2 provided very
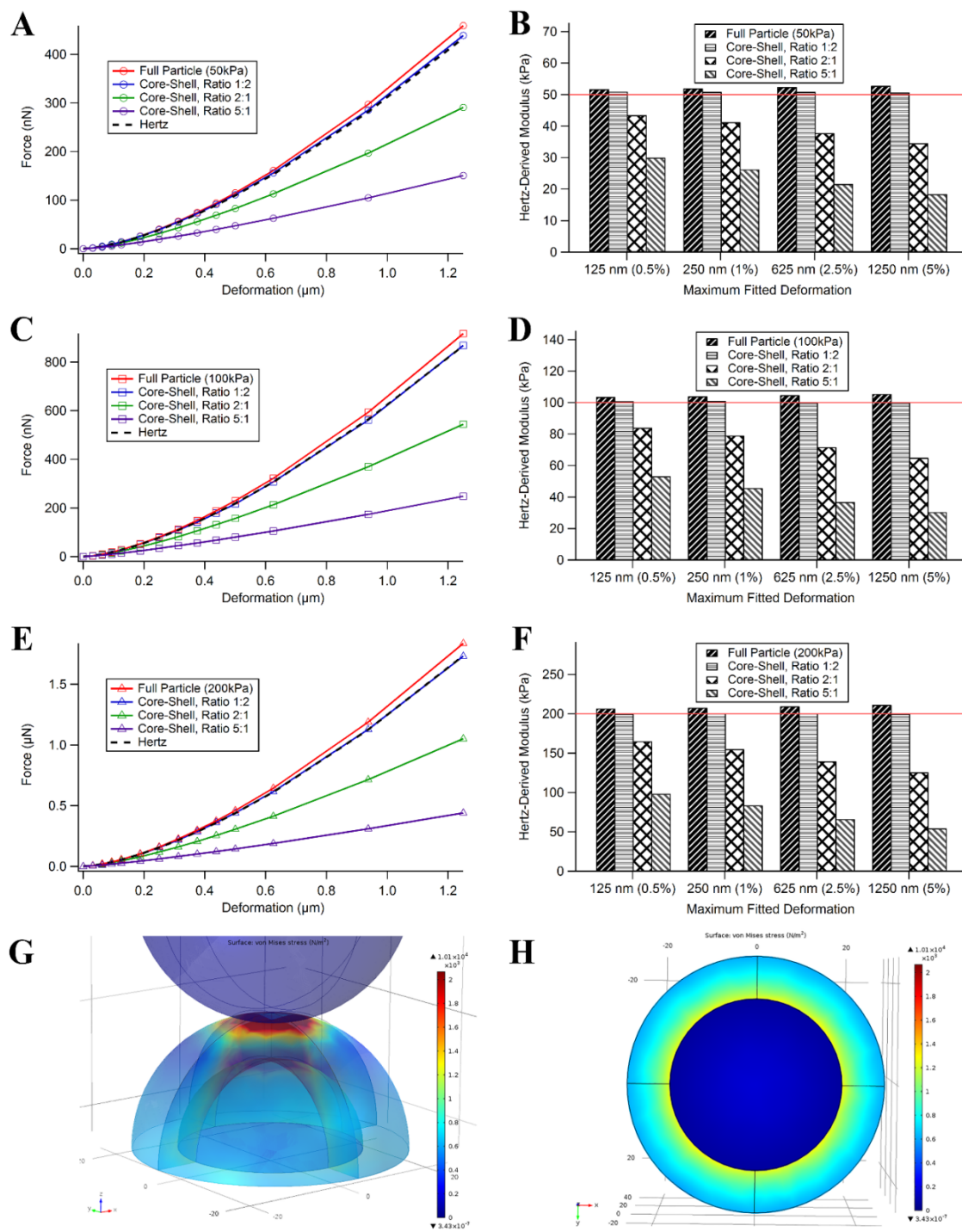
Figure 17 A), C), E) F-D curves produced from finite element analysis of a full particle and
core-shell particles of different core to shell ratios (1:2, 2:1, and 5:1). Hertz's analytical solution was included
for comparison. B), D), F) Elastic modulus derived from Hertz-fitting of F-D curves in A), C), E) as a function
of maximum deformation used for fitting. In brackets are deformation values expressed as a percentage of
particle radius. Red line represents modulus value of shell component used in simulations. Modulus values
of A), B) 50 kPa; C), D) 100 kPa; or E), F) 200 kPa were used for the shell and 5 kPa for the core. G), H)
Finite element model simulating the elastic deformation of a soft core-shell particle by a rigid silica probe.
Finite element solution produced the von Mises stress distribution of the deformed core-shell particle for a
G) 3D hemisphere and a H) 2D cross-section. The shell and core components have elastic moduli of 200 kPa
and 5 kPa, respectively. Reprinted with permission.[86] Copyright 2016 American Chemical Society.

accurate approximations (> 95%) of the analytical solution for deformations up to 1250 nm, 5% of the entire particle radius. The FEM model for core-shell particles at a ratio of 2:1 produced modulus values of 84 kPa (84%) and for a 5:1 53 kPa (53%) from Hertz-fitting of 125 nm deformations, respectively. (Figure 17 C, D) Additionally, the same finite element analysis was performed with shell elastic moduli of 200 kPa and 50 kPa. (Figure 17 A, B, E, F) Slightly better approximations of the analytical solutions were obtained for FEM solutions with a smaller difference in modulus between the core and shell components. FEM models with a much stiffer shell component experienced greater segregation in the mechanical response between the core and shell as can be observed from the von Mises stress distributions of the two components. (Figure 17 G, H) This resulted in greater deviations from a homogenous model as assumed by the Hertz analytical solution.

These are promising results considering that the experimentally relevant deformations for our CP-AFM studies were between 100 to 400 nm and most of the investigated PA/PSSA core-shell particles had a core-to-shell ratio of 2:1 or lower. These results indicated that the effective particle modulus derived from Hertz analysis of our PA/PSSA core-shell particles is a good estimate (>75%) of the modulus of the PA/PSSA polymeric shells.

In our force spectroscopy measurements, we focused only on the mechanical response of particles in the small deformation regime (<1% of particle radius and <8% of shell thickness). PA/PSSA core-shell particles of various shell thicknesses and empty agarose particles were studied for elastic deformations between 100 and 400 nm (Figure 18 A). The logarithmic force vs. logarithmic deformation curves of measured hydrogel particles had gradients that fall in the range of 1.4−1.6, close to the power-law exponent of 1.5 described by the Hertz model (Figure 18 B), demonstrating that F−D curves exhibited good fit of the Hertz model. The force response remained unchanged, and particle deformations were elastic for at least 20 cycles (Figure 18 C). This indicates that they have retained their original shell conformation after each compression event.

V.3.3. Tuning of Mechanical Properties by Varying Thickness of Polymeric Shell or Number of Polymer Layers

The inwards buildup self-assembly technique is not a self-limiting process. As a result, shell thickness can be easily increased by increasing the concentration or incubation period of PA. The entire hydrogel particle can be filled if so desired. To probe the
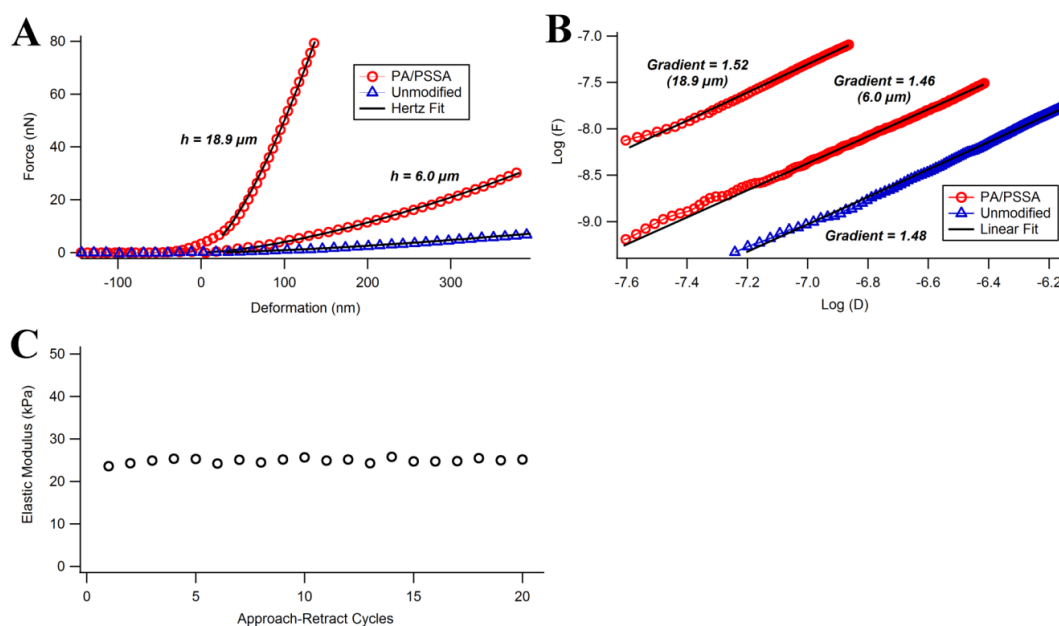
Figure 18   Representative A) F–D curves and B) Log(F)–Log(D) curves for PA/PSSA core-shell particles of different shell thicknesses (h). Solid lines represent A) analytical fits of the Hertz model (eq. 47) and B) linear fits applied to the data. C) Plot of elastic modulus over 20 approach-retract force cycles. Reprinted with permission.[86] Copyright 2016 American Chemical Society.

effectiveness of this technique in tuning mechanical properties, we studied the relationship between the elastic modulus of particles and the thickness of the polymeric shells. Hydrogel core-shell particles were prepared from two different PA concentrations (0.2 and 0.4 mg mL^{-1}) and an excess of PSSA polymer. The PSSA polymer acts as a stabilizing layer and interacts with PA to form water-stable complexes. By itself, PSSA does not form any stable interactions with agarose that contribute to shell formation, and any excess PSSA is washed away.[105] This produces hydrogel core-shell particles with a range of different shell thicknesses. The elastic modulus and mean fluorescence intensity of PA−TRITC/PSSA core-shell particles with shell thicknesses between 10 and 24 μm were then investigated via single-particle measurements using the CP-AFM technique. Results illustrated that the modulus of PA/PSSA particles increased from 10 to 190 kPa in a nonlinear manner as polymeric shell thickness increased from 10 to 24 μm (Figure 19).

The particle modulus exhibited a steeper initial increase which gradually leveled off with increasing shell thickness. The results for mean fluorescence intensity, which corresponds to the density of the polymeric shell, were consistent with the nonlinear increase of elastic modulus as shell thickness increased. Consequently, the mechanical properties of PA/PSSA core-shell particles can be directly correlated to the density of the
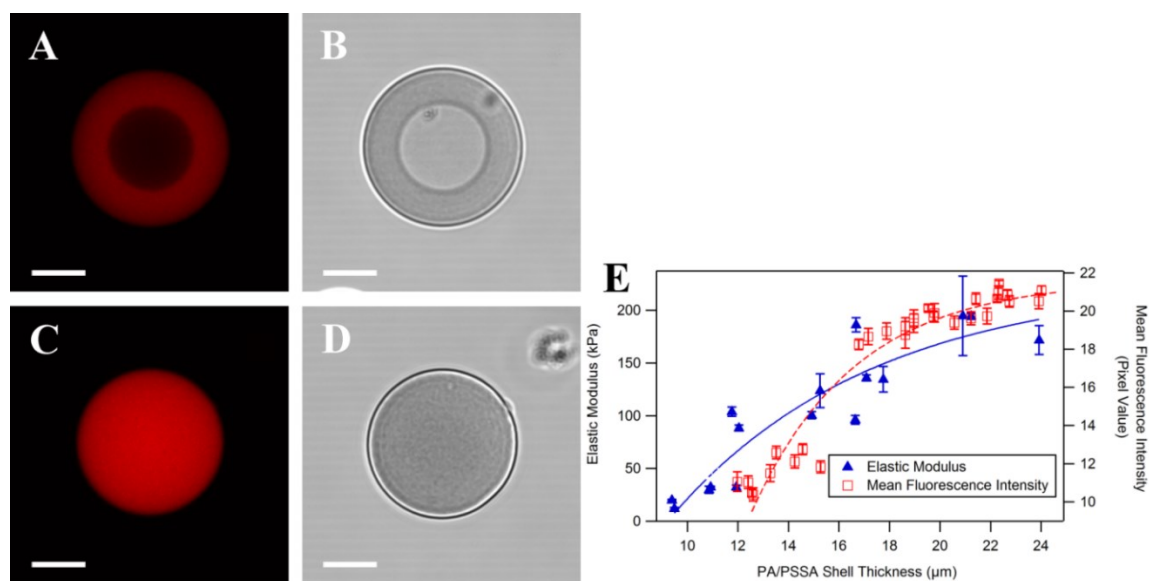
Figure 19   Confocal laser scanning microscopy and corresponding bright-field images of PA-TRITC/PSSA core-shell particles of polymeric shell thicknesses A), B) 15 μm and C), D) 26 μm (polymer filled the entire agarose core). All scale bars represent 20 μm. E) Elastic modulus and mean fluorescence intensity of PA-TRITC/PSSA particles as a function of shell thickness. Solid and dotted lines represent exponential fits applied to the data. Reprinted with permission.[86] Copyright 2016 American Chemical Society.

PA/PSSA polymeric shell. The initial deposition of PA polymer onto the porous agarose matrix led to both an increase in density and thickness of the polymeric shell (10−18 μm). However, as more PA polymer was deposited, the number of hydroxyl groups on the agarose network available for hydrogen bonding rapidly decreased. As a result, the density of the PA/PSSA polymeric shell approaches saturation, and further adsorption only led to an increase in polymeric shell thickness without much increment in density (>18 μm).

Representative plots of fluorescence intensity profiles suggested a homogeneous distribution of fluorescently labeled PA across the thickness of the polymeric shell (Figure 20). The homogeneity of the fluorescently labeled PSSA layer was also observed in a previous report.[105] This was consistent with the Hertzian deformation behavior observed in CP-AFM measurements, indicating high homogeneity of the polymeric shell in PA/PSSA particles. This seems to be counterintuitive considering that shell formation which proceeds in a surface-to-core direction[104] should produce an anisotropic, polymeric shell. This could be due to the continuous rearrangement of polymers during the organic phase polymer assembly process and the presence of transient interactions between molecules.

.
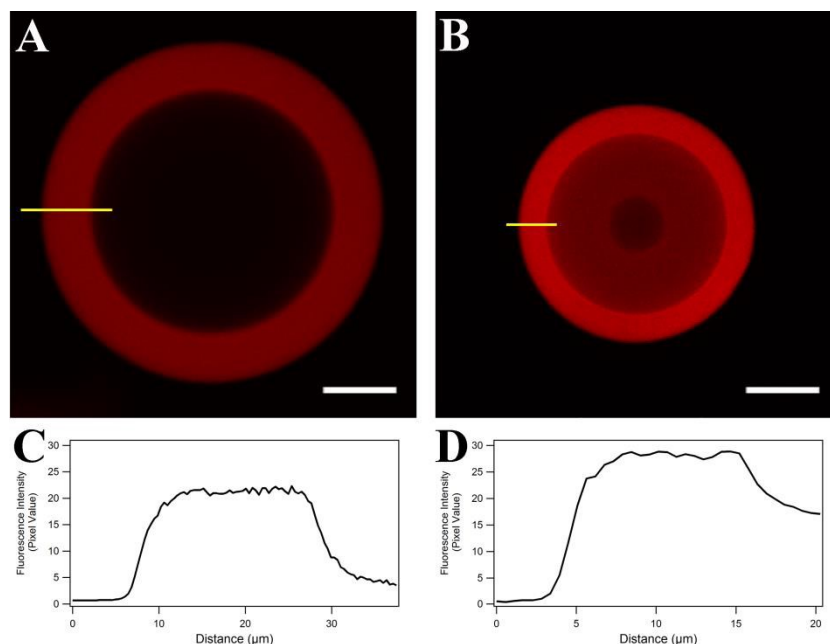
Figure 20   Confocal laser scanning microscopy images and corresponding plots of fluorescence intensity profiles obtained at the yellow line for A), C) Pa/PSSA and B), D) (PA/PSSA)$_2$ core-shell particles. PA concentration of 0.4 mg mL^{-1} and PSSA in excess were used. All scale bars represent 30 μm. Reprinted with permission.[86] Copyright 2016 American Chemical Society.

Next, the elastic modulus and polymeric shell density (mean fluorescence intensity) were compared for two-layer (PA/PSSA) and four-layer (PA/PSSA)$_2$ core-shell particles with shell thicknesses between 14 and 26 μm and particle sizes between 30 and 140 μm. Both two-layer and four-layer particles were prepared from a PA concentration of 0.4 mg mL^{-1} and an excess of PSSA. Empty agarose particles were used as experiment control. No coherent pattern can be observed between the size of particles and their elastic modulus or shell density. An increase in elastic modulus of about 300−500 kPa can be observed as layer number increased from two to four layers (Figure 21 A), much greater than that
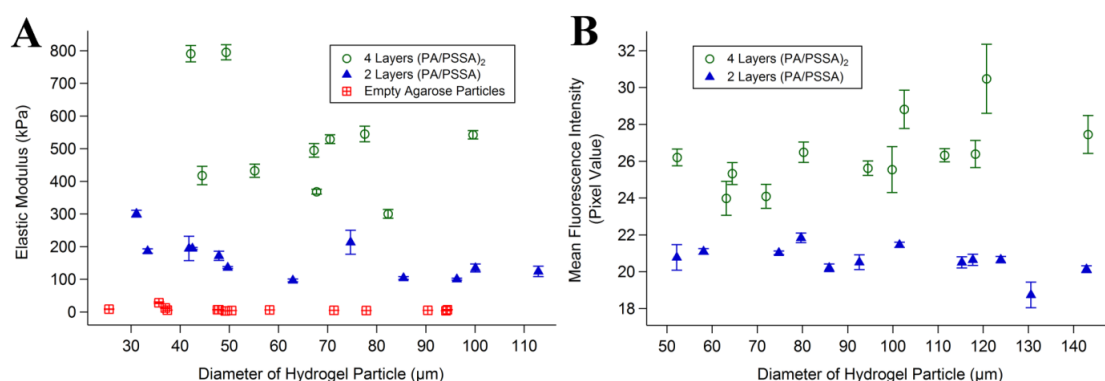
Figure 21   A) Elastic modulus and)B) mean fluorescence intensity of 2-layer (PA-TRITC/PSSA) and 4-layer (PA-TRITC/PSSA)$_2$ core-shell particles as a function of particle size. Empty agarose particles were also compared for elastic modulus measurements. Reprinted with permission.[86] Copyright 2016 American Chemical Society.
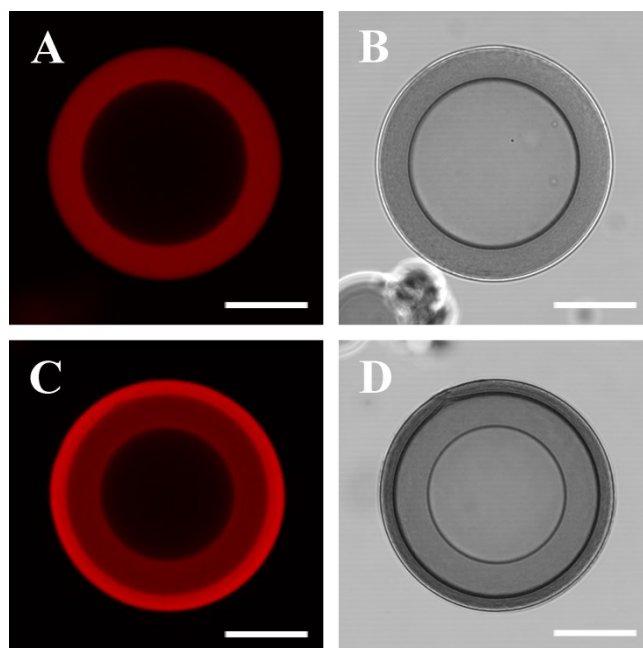
Figure 22   Confocal laser scanning microscopy and corresponding bright-field images of A), B) a 2-layer (PA-TRITC/PSSA) core-shell particle and C), D) a 4-layer (PA-TRITC/PSSA)$_2$ core-shell particle. All scale bars represent 50 μm. Reprinted with permission.[86] Copyright 2016 American Chemical Society.

observed for variations in shell thickness. This was consistent with the increase in polymeric shell density observed for four-layer core-shell particles (Figure 21 B).

Due to the interweaving of different PA/PSSA bilayers, this also creates a multi-density polymeric shell with discrete density differences (Figure 22). This unique morphology can be utilized for separation and containment of differently sized macromolecules.[105] As shown in Figure 19, polymeric shell density and elastic modulus approach a maximum after a certain increase in shell thickness. However, by assembling an additional layer of PA, the shell density and elastic modulus can be further increased without increasing overall shell thickness. This could be explained by the formation of new interactions between PA and PSSA, in addition to existing PA−agarose complexes. Moreover, this shows that the porous hydrogel matrix was not "fully packed" and it was possible to increase the polymeric shell density further.

V.3.4. Mechanical Properties of PA/PSSA and (PA/PSSA)$_2$ Core-Shell Particles

The averaged values of elastic modulus and mean fluorescence intensity of empty hydrogel (2% agarose) particles, PA/PSSA (0.2 and 0.4 mg mL^{-1}) and (PA/PSSA)$_2$ core-shell particles are summarized in Figure 23 A. The average elastic modulus of agarose
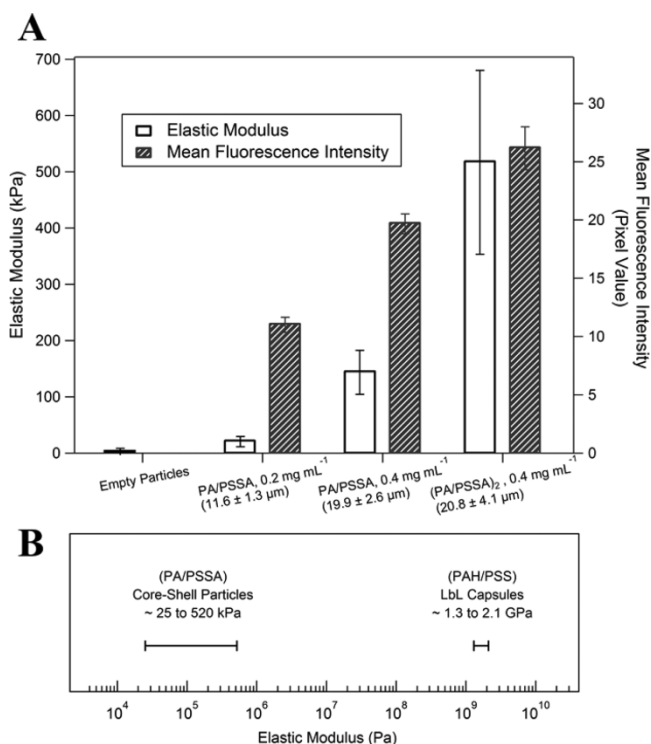
Figure 23   Averaged values for elastic modulus and mean fluorescence intensity of empty agarose particles, PA-TRITC/PSSA and (PA-TRITC/PSSA)$_2$ core-shell particles. 0.2 and 0.4 mg mL^{-1} refer to concentrations of PA-TRITC used in preparing the hydrogel core-shell particles. Numerical values in bracket refer to the thickness of polymeric shells. Reprinted with permission.[86] Copyright 2016 American Chemical Society.

particles before assembly of polymeric shells was measured to be 7.3 kPa. At a PA concentration of 0.2 mg mL^{-1} and an excess of PSSA, PA/PSSA polymeric shells with an average thickness of 11.6 ± 1.3 μm were formed. An average elastic modulus of 25 kPa was recorded for PA/PSSA core-shell particles. At a higher polymer concentration of 0.4 mg mL^{-1}, average shell thickness increased to 19.9 ± 2.6 μm and the average modulus of core-shell particles further increased to 150 kPa. Increasing the layer number to form (PA/PSSA)$_2$ core-shell particles, a significantly higher elastic modulus of 520 kPa was obtained. A positive correlation was always observed between the elastic modulus and polymeric shell density (mean fluorescence intensity) of PA/PSSA core-shell particles. Furthermore, a much higher deviation is observed for the elastic modulus and polymeric density of four-layer core-shell particles due to additional variability from the influence of shell properties of the first bilayer on the shell formation of the second bilayer. Briefly, a thicker and denser polymeric shell (first bilayer) will also act to slow down the diffusion of subsequent polymers and affect shell formation of the second bilayer. PA/PSSA core-shell particles synthesized from inwards interweaving selfassembly (~25−520 kPa) were 4−5 orders of magnitude softer than poly(allylamine hydrochloride)/poly(styrenesulfonate)

(PAH/PSS) capsules prepared from conventional LbL polyelectrolyte self-assembly (~1.3−2.1 GPa)[127, 128] (Figure 23 B). This huge variance in elastic modulus between similar materials could be explained by fundamental differences in the shell assembly process. For PAH/PSS capsules, the polymeric shell is formed from the adsorption of oppositely charged polyelectrolytes onto the surface of a sacrificial core. In contrast, for PA/PSSA core-shell particles, the polymeric shell is assembled within the porous agarose core, building onto interactions between noncharged PA and agarose. As a result, the mechanical properties of PA/PSSA core-shell particles are highly dependent on the properties of the agarose core. This was supported by previous studies showing that shell density is positively correlated to the concentration of agarose.[109]

LbL capsules are frequently used as test candidates for the study of cellular uptake.[129] However, only nanometer-thick, rigid shells are formed in LbL capsules which quickly buckle once deformation exceeds the thickness of the shell, analogous to a "ping-pong ball".[124] In contrast, the inwards interweaving self-assembly technique creates a much thicker polymeric shell with a greater shell-to-core ratio. By varying shell thickness alone, our approach allows tuning of soft hydrogel core-shell particles in the range of 10−190 kPa (Figure 19). This is particularly important in mechanobiology as previous studies have reported enhanced uptake by certain cell lines for particles with a modulus in the low-kilopascal range (<140 kPa).[101, 102] Therefore, micrometer-sized core-shell particles (3−5 μm) that are fabricated by inwards interweaving self-assembly will make an excellent particle system for the systemic investigation of stiffness-dependent cellular uptake.

V.4. Conclusion

To conclude, we have successfully shown that soft hydrogel core-shell particles can have their elastic modulus tuned in the range of 10−190 kPa by variation of shell thickness and further increased by increasing layer number. The inwards interweaving self-assembly technique is a valuable method for creating multi-density or single-density shells of tunable thickness and represents a facile approach for adjusting the mechanical properties of hydrogel core-shell particles. Micrometer-sized core-shell particles that are synthesized from this technique would potentially make an excellent model system for the systemic study of stiffness-dependent cellular uptake. We envision that the CP-AFM and quantitative fluorescence studies presented in this work will provide the first steps toward

the rational design of a compartmentalized core-shell particle for the separation of biomolecules or targeted delivery of drugs.

V.5.   References

[72] H. Hertz, *Journal für die reine und angewandte Mathematik* **1882**, 1882, 156.

[86] H. M. Pan, M. Seuss, M. P. Neubauer, D. W. Trau, A. Fery, ACS Applied Materials & Interfaces **2016**, 8, 1493.

[88] A. Noda, M. Yamaguchi, M. Aizawa, Y. Kumano, "Cosmetic containing fine soft microcapsules", Google Patents, 1992.

[89] S. Wiese, A. C. Spiess, W. Richtering, Angewandte Chemie **2013**, 125, 604.

[90] R. P. John, R. Tyagi, S. Brar, R. Surampalli, D. Prévost, Critical reviews in biotechnology **2011**, 31, 211.

[91] H. M. Shewan, J. R. Stokes, Journal of Food Engineering **2013**, 119, 781.

[92] W. C. Mak, K. Y. Cheung, D. Trau, Chemistry of Materials **2008**, 20, 5475.

[93] H. Senff, W. Richtering, Colloid and Polymer Science **2000**, 278, 830.

[94] J. Meid, F. Dierkes, J. Cui, R. Messing, A. J. Crosby, A. Schmidt, W. Richtering, Soft Matter **2012**, 8, 4254.

[95] T. R. Hoare, D. S. Kohane, Polymer **2008**, 49, 1993.

[96] M. Delcea, S. Schmidt, R. Palankar, P. A. L. Fernandes, A. Fery, H. Moehwald, A. G. Skirtach, Small **2010**, 6, 2858.

[97] A. G. Skirtach, A. Munoz Javier, O. Kreft, K. Köhler, A. Piera Alberola, H. Möhwald, W. J. Parak, G. B. Sukhorukov, Angewandte Chemie International Edition **2006**, 45, 4612.

[98] B. G. De Geest, S. De Koker, G. B. Sukhorukov, O. Kreft, W. J. Parak, A. G. Skirtach, J. Demeester, S. C. De Smedt, W. E. Hennink, Soft Matter **2009**, 5, 282.

[99] B. V. Parakhonskiy, A. M. Yashchenok, M. Konrad, A. G. Skirtach, Advances in colloid and interface science **2014**, 207, 253.

[100] R. Hartmann, M. Weidenbach, M. Neubauer, A. Fery, W. J. Parak, Angewandte Chemie International Edition **2015**, 54, 1365.

[101] X. Banquy, F. Suarez, A. Argaw, J.-M. Rabanel, P. Grutter, J.-F. Bouchard, P. Hildgen, S. Giasson, Soft Matter **2009**, 5, 3984.

[102] W. Liu, X. Zhou, Z. Mao, D. Yu, B. Wang, C. Gao, Soft Matter **2012**, 8, 9235.

[103] X. Yi, X. Shi, H. Gao, Physical review letters **2011**, 107, 098101.

[104] J. Bai, S. Beyer, W. C. Mak, R. Rajagopalan, D. Trau, Angewandte Chemie International Edition **2010**, 49, 5189.

[105] H. M. Pan, S. Beyer, Q. Zhu, D. Trau, Advanced Functional Materials **2013**, 23, 5108.

[106] G. Decher, science **1997**, 277, 1232.

[107] K. Sato, T. Nakajima, J.-i. Anzai, Journal of colloid and interface science **2012**, 387, 123.

[108] K. Landfester, A. Musyanovych, V. Mailänder, Journal of Polymer Science Part A: Polymer Chemistry **2010**, 48, 493.

[109] J. Bai, S. Beyer, T. S. Yein, D. Trau, ACS applied materials & interfaces **2011**, 3, 1665.

[110] J. Bai, S. Beyer, W. C. Mak, D. Trau, Soft Matter **2009**, 5, 4152.

[111] H. M. Pan, A. Subramanian, C. J. Ochs, J.-Y. Dewavrin, S. Beyer, D. W. Trau, RSC Advances **2014**, 4, 35163.

[112] W. C. Mak, J. Bai, X. Y. Chang, D. Trau, Langmuir **2008**, 25, 769.

[113] W. A. Ducker, T. J. Senden, R. M. Pashley, Nature **1991**, 353, 239.

[114] E. K. Dimitriadis, F. Horkay, J. Maresca, B. Kachar, R. S. Chadwick, Biophysical journal **2002**, 82, 2798.

[115] A. Fery, F. Dubreuil, H. Möhwald, New Journal of Physics **2004**, 6, 18.

[116] J. Domke, M. Radmacher, Langmuir **1998**, 14, 3320.

[117] C. Ye, I. Drachuk, R. Calabrese, H. Dai, D. L. Kaplan, V. V. Tsukruk, Langmuir **2012**, 28, 12235.

[118] M. Pretzl, M. Neubauer, M. Tekaat, C. Kunert, C. Kuttner, G. r. Leon, D. Berthier, P. Erni, L. Ouali, A. Fery, ACS applied materials & interfaces **2012**, 4, 2940.

[119] M. P. Neubauer, C. Blüm, E. Agostini, J. Engert, T. Scheibel, A. Fery, Biomaterials Science **2013**, 1, 1160.

[120] S. Schmidt, M. Zeiser, T. Hellweg, C. Duschl, A. Fery, H. Moehwald, Advanced Functional Materials **2010**, 20, 3235.

[121] B. Cappella, J. R. Wassenberg, L.-O. Heim, M. Klostermann, J. Venzmer, E. Bonaccurso, Polymer **2014**, 55, 1209.

[122] J. P. Best, S. Javed, J. J. Richardson, K. L. Cho, M. M. Kamphuis, F. Caruso, Soft Matter **2013**, 9, 4580.

[123] E. Glynos, V. Sboros, V. Koutsos, Materials Science and Engineering: B **2009**, 165, 231.

[124] A. Fery, R. Weinkamer, Polymer **2007**, 48, 7221.

[125] J. L. Hutter, J. Bechhoefer, Review of Scientific Instruments **1993**, 64, 1868.

[126] S. Beyer, J. Bai, A. M. Blocki, C. Kantak, Q. Xue, M. Raghunath, D. Trau, Soft Matter **2012**, 8, 2760.

[127] F. Dubreuil, N. Elsner, A. Fery, The European Physical Journal E **2003**, 12, 215.

[128] C. Gao, E. Donath, S. Moya, V. Dudnik, H. Möhwald, The European Physical Journal E **2001**, 5, 21.

[129] A. Muñoz Javier, O. Kreft, A. Piera Alberola, C. Kirchner, B. Zebli, A. S. Susha, E. Horn, S. Kempter, A. G. Skirtach, A. L. Rogach, Small **2006**, 2, 394.

VI.   Core-Shell Microgels with Switchable Elasticity at Constant Interfacial Interaction

The following chapter is in its entirety based on the research article of myself, W. Schmolke and others published in *ACS Applied Materials & Interfaces*, Volume 8, Issue 25, Pages 16317 - 16327 in 2016.[87] It is reprinted with permission while the copyright is with the American Chemical Society 2016. All schemes and figures are used as published as well as most of the text is reproduced. It was modified in some sections to be integrated into this thesis and expanded by content initially published in the connected Supporting Information.

VI.1.   Introduction

Thermosensitive polymers exhibit marked reversible changes of their polymer-solvent interactions at critical solution temperatures, rendering them promising for diverse applications. A particularly favorable type of thermosensitive polymer system is poly(N-isopropylacrylamide) (pNIPAAm) in water, which displays such responsivity at a lower critical solution temperature (LCST) of ~32 °C.[130, 131] As an effect of this temperature-dependent polymer-solvent interaction,[132, 133] cross-linked polymer-network hydrogels based on pNIPAAm exhibit a reversible volume phase transition from swollen to deswollen states[134-137] and a significant increase of the water contact angle[138, 139] as the temperature exceeds the LCST. This property renders pNIPAAm-based hydrogels useful for a plethora of applications, which has been particularly explored for microscopic pNIPAAm gel particles.[140-142] In these systems, the particle swelling−deswelling transition causes a change of the microgel volume fraction[143] and of the microgel interaction potential.[144, 145] The conjoint use of both these effects can serve to induce temperature-controlled transitions between pNIPAAm-based microgel glasses, suspensions, and gels,[146] thereby offering rich versatility for in situ tuning of the state of pNIPAAm microgel-based soft matter. Furthermore, when a pNIPAAm hydrogel or microgel deswells, it exhibits drastic changes in its mechanical properties such as the gel's elastic[147] or Young's modulus.[148, 149] Again, the conjoint use of both these effects can be beneficial, for example, to serve in switchable cell culture substrates that allow for temperature-controlled cell adhesion and detachment.[120, 150] However, whereas these specific applications use the conjoint change

of the coupled variables mentioned above, it is desirable to change just one of them while keeping the others constant in more general rational materials design. For example, in situ tuning the elasticity of gel substrates is desirable in view of studying its effect on attached cells[150] but this should occur without concurrently influencing the cell adhesion.[96] For this and other purposes, it is desired to use temperature to easily and reversibly change the gel's elastic or Young's modulus without conjointly changing the gel hydrophilicity.[100]

In this paper, we present a design approach for microgel particles that allow their elastic and Young's moduli to be changed by variation of temperature without exhibiting perceptible accompanying changes of their hydrophilicity and adhesion. These particles are core-shell microgels consisting of a thermosensitive pNIPAAm hydrogel core wrapped by a non-thermo-responsive polyacrylamide (pAAm) hydrogel shell, as sketched in Figure 24.
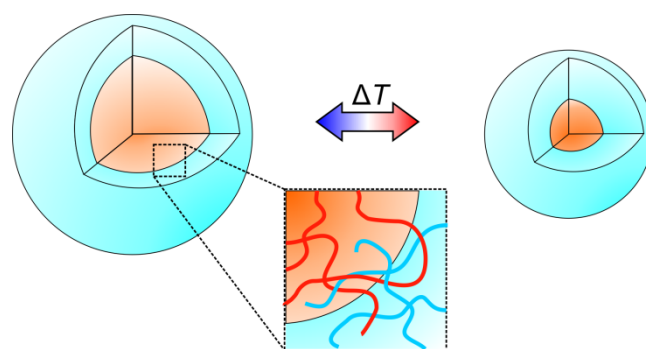
Figure 24   Volume phase transition of core-shell microgels with a thermo-responsive poly(*N*-isopropylacrylamide) pNIPAAm core and a non-thermo-responsive polyacrylamide (pAAm) shell. When the core and shell are connected and exhibit some interpenetration at their interface, temperature-dependent deswelling of the pNIPAAm core forces the pAAm shell to contract as well, thereby leading to an increase of the particles surficial Young's modulus. While this happens, however, the particles' surficial hydrophilicity does not change, because the polymer-solvent interaction of the outer pAAm material is not strongly temperature-dependent around 34 °C. Reprinted with permission.[87] Copyright 2016 American Chemical Society.

Whereas the core can be swollen and deswollen in response to changes in temperature around 34 °C; the shell is just indirectly affected by this process. Because of some interfacial polymer interpenetration and connection of the pNIPAAm core to the pAAm shell, as illustrated in Figure 24, its thermosensitive contraction can force the pAAm shell to contract as well, as also illustrated in Figure 24, thereby affecting the Young's modulus on the particle surface at elevated temperatures. This thermo-mechanical effect on the nonresponsive shell is expected to depend on the shell thickness and its polymer-network composition, which are two design criteria focused on in this study. While the gels get contracted, however, the surface interactions of the pAAm shell are unaffected by small changes in temperature. These microgels, therefore, hold good promise to be used as building blocks to assemble larger layers or aggregates[151] that allow their elasticity to be

switched within determined ranges without conjoint perceptible change of their interfacial interaction potential and adhesion energy per area.

In earlier work, similar core-shell gel particles with sizes from tens of nanometers to about one micrometer have been used to combine the response of different core and shell materials to create multiple stimuli-sensitive,[152-154] or two-step responsive materials.[155-157] Zhao et al. covered temperature-responsive pNIPAAm nanogels by a nonresponsive hydrophobic pMMA shell.[158] Richtering et al. produced colloidal core-shell microgels from temperature-responsive polymers with different LCSTs. By small-angle neutron scattering[155] and theoretical calculations,[159] they verified the interpenetration of the core and shell polymers and the resulting mutual influence of their temperature-responsive swelling. These papers also report about the influence of various parameters such as the shell thickness,[152] radial inhomogeneities of the network,[153] and the cross-linking density[156] on the particle response. To complement this existing work, the present study combines thermos-responsive pNIPAAm cores with sizes in the above-colloidal domain with a soft, nonresponsive polymer shell, taking advantageous use of the exquisite control on the particle fabrication provided by droplet-based microfluidic templating.[160]

VI.2. Experimental Section

Materials:

All chemicals were used without further purification and purchased from Sigma-Aldrich, unless stated otherwise. 1,4-dioxane and n-hexane were purchased from Roth. 1H,1H,2H,2H-perfluorooctanol was purchased from Alfa Aesar. Octadecyltrimethoxysilane was purchased from Acros Organics. The modified polyether−polysiloxane surfactant ABIL EM 90 was donated by Evonik, which we gratefully acknowledge. The perfluorinated oil Novec HFE-7500 was purchased from 3M. Acrylamide was recrystallized twice from chloroform prior to use. If not noted further, purified water from a Milli-Q water purifier with a resistance of 18.2 MΩ·cm (T = 25 °C) was used. Dialyses were done with tubes from regenerated cellulose 132703 (SpectraPor) with a molecular weight cutoff of 12−14 kg mol−1.

Equipment:

1H NMR spectra were recorded on a Bruker Advance 400 digital FT-spectrometer at 400 MHz at T = 25 °C. Chemical shifts reported in ppm are referenced to trimethylsilane (TMS) as a standard using δ(TMS) = 0 ppm. High-resolution mass spectroscopy (HRMS)

with electron-spray ionization (ESI) was carried out on an Ionspec QFT-7 from Varian Inc. Atomic force measurements were carried out on a MFP-3D atomic force microscope equipped with a BioHeater closed fluid cell with a polyethyleneimine-coated glass surface, both from Asylum Research. A MikroMasch NSC12 no Al backside coating tipless cantilever made from n-type silicon, bought from Nanoworld AG, was used. The AFM was coupled to an AxioObserver Z1 inverted optical microscope by Carl Zeiss for optical control of the cantilever placement. Samples were suspended in purified water from a Milli Q water purifier with a resistance of 18.2 M$\Omega \cdot$cm (T = 25 °C). Data analysis was done with IGOR Pro 6.3.6.4 by WaveMetrics software, which was supplemented by the 120804+1702 add-on package for AFM analysis by Asylum Research. Microgel swelling and deswelling measurements were carried out on the same BioHeater closed fluid cell from Asylum Research mentioned above. The temperature of each sample was varied from 28 to 38 °C. After equilibration for 30 min, an optical micrograph was taken at each temperature with a highresolution digital camera from Carl Zeiss. The pictures were analyzed to determine the particle sizes using ImageJ 1.49 software.

Synthesis of shell-precursor polymer and its UV-cross linkable monomer unit:

The used UV-cross linkable *N*-(2-(3,4-dimethyl-2,5-dioxo-2,5-dihydro-1H-pyrrol-1-yl)ethyl)acrylamide (DMMIAAm) co-monomer in the polyacrylamide (pAAm) shell is not commercially available and was synthesized in a four-step reaction by W. Schmolke. Since the organic chemistry behind and the pre-polymerisation is out of focus for this thesis, the reader is referred to original publication.[87]

Microfluidic Setup for Microgel Synthesis:

Microfluidic devices were manufactured using soft lithography.[161] A polydimethylsiloxane (PDMS)/cross-linker mixture (Sylgard 184 silicone elastomer kit, Dow Corning, base: curing agent = 10:1) was poured onto a silicon wafer that has been patterned with SU-8 photoresist (MicroChem Corp.) before. After curing for 1 h at 65 °C, the solidified PDMS was attached to a glass slide by plasma bonding. Two types of microfluidic devices were fabricated. The device for core-microgel formation had single cross-junction geometry with a channel height and width of 25 μm. The encapsulation device used for core-shell microgel formation had a sequential double cross-junction geometry with a channel height of 40 μm and a channel width of 50 μm. To render the devices hydrophobic, octadecyltrimethoxysilane was injected into the channels, allowed to sit for 1 min, and then removed by subsequent rinsing with 2-propanol and water.

In all microfluidic experiments, pumps used were PhD Ultra Syringe Pumps (Harvard Apparatus), operating with disposable syringes (1−5 mL, Becton Dickson) and Intramedic Clay Adams PE Tubing "PE 20" (Becton Dickinson). To monitor the droplet formation, all devices were operated on an optical microscope (Zeiss PrimoVert) connected to a digital camera (UK1155-M, ABS GmbH, Jena, Germany). All experiments were carried out at ambient temperature (23 ± 1 °C).

Microfluidic Fabrication of p(NIPAAm-co-BIS) Core Microgels:

A NIPAAm monomer solution with a concentration of 100 g L^{-1} containing 1 mol % of the cross-linker N,N′-methylenebis(acrylamide) (BIS) was emulsified by flow-focusing with fluorinated oil Novec HFE- 7500 (3M) containing 1.8 wt % of Krytox (DuPont) as a surfactant. APS and TEMED were used to initiate the polymerization. APS was premixed to the monomer solution at a concentration of 8 g L^{-1}, whereas TEMED was premixed to the Novec HFE-7500 oil phase at a concentration of 3 vol %. Flow rates were 40 μL h^{-1} and 160 μL h^{-1} for the NIPAAm−BIS solution and the oil phase, respectively. The resulting pre-microgel droplets were collected and stored overnight to ensure completion of the free radical polymerization; this long reaction time also assures even distribution of all components by diffusion within the gelling droplets. The pre-microgel suspension was covered by a thin layer of paraffin oil to suppress solvent evaporation during this process. After storage, paraffin and HFE-7500 oils were removed by depipetting, and the microgels were washed with Novec HFE-7500 containing 20 wt % of 1H,1H,2H,2H-perfluorooctanol (1×), plain Novec HFE-7500 (2×), n-hexane containing 1 wt % of the surfactant Span 80 (Sigma-Aldrich) (2×), n-hexane (2×), isopropyl alcohol (4×), 1,4 dioxane (4×), and distilled water (4×).

Microfluidic Fabrication of pNIPAAm-pAAm Core-Shell Microgels:

A p(AAm-co-DMMIAAm) solution with a concentration of 100 g L^{-1} containing 10 mmol L^{-1} of the triplet photosensitizer sodium 2,7-thioxanthonedisulfonate, prepared according to Kronfeld and Timpe,[162] was used to encapsulate the p(NIPAAm-co-BIS) core microgels. The microfluidic device and the tubing were wrapped in aluminum foil to prevent gelation of the p(AAm-co-DMMIAAm) solution by ambient light. The syringe containing the aqueous pNIPAAm microgel suspension was inserted into the syringe pump beforehand and stored overnight with the tip facing down to induce sedimentation of the microgels within the syringe. The corresponding tubing was made hydrophobic by coating with octadecyltrimethoxysilane. Core-shell pre-microgel droplets were formed, using low

viscous paraffin oil containing 2 wt % of the modified polyether−polysiloxane surfactant ABIL EM 90 as the continuous phase. Flow rates were 40 μL h^{-1} (pNIPAAm microgels), 20 μL h^{-1} (pAAm-co-DMMIAAm), and 80 μL h^{-1} (paraffin oil). Upon exiting the microfluidic device, the droplets were exposed to UV light (Blak-Ray B-100AP high-intensity UV lamp, λ = 365 nm, intensity = 100 W). After collection in a vial, the obtained microgel emulsions were washed several times with water to remove the paraffin oil.

Colloidal Probe Atomic Force Microscopy:

All AFM experiments were performed on a MFP-3D Bio from AsylumResearch, an Oxford Instruments company. For calibration of the cantilever, the inverse optical lever sensitivity (InvOLS) was determined by line fitting the repulsive part of F−D curves on a glass surface. Assuming that the glass is not deformable, a direct correlation between the cantilever deflection in nm and the measured output voltage is established. The spring constant of each cantilever (NSC 12 noAl, k = 0.1−1 N m^{-1}, MikroMasch) was calibrated prior to the attachment of the colloidal probe with the thermal noise method.[125] Glass beads with a radius of 23 and 2 μm were used as colloidal probes. Young's moduli derived from measurements with different probe sizes are quantitatively comparable since the Hertz equation takes into account the probe radius. They were glued onto the free-standing end of the cantilever with two-component epoxy glue (UHU endfest) using a micromanipulator (MP-285, Sutter Instruments) mounted on an inverted microscope (AxioVert, Zeiss).

Prior to the experiments, the glass surface of the BioCell was cleaned with isopropyl alcohol and water, and the colloidal probe cantilever was cleaned in O_2 plasma for 30 s. For the mechanical characterization of the pNIPAAm particles, the colloidal probe was not plasma cleaned but coated with a polyethyleneglycol−poly-L-lysine layer to suppress adhesive forces. About 100 μL of each sample solution was spread on the glass surface, and particles were allowed to sediment for at least 30 min before the fluid cell was completely filled with Milli-Q water. For some experiments, the glass surface was additionally coated with a polyethyleneimine layer to improve the fixation of the hydrogel particles on the glass surface. The fixation and location of the particles were controlled with an inverted optical microscope and the top-view optics of the AFM. After equilibration at a given temperature for at least 30 min, the colloidal probe was aligned centric above each hydrogel particle under optical control with the microscope. The force-set point for F−D curves was adjusted for each particle type to achieve sufficient deformation (≥500 nm) for mechanical evaluation. Furthermore, the distance range of the F−D was adjusted such that

the probe comes out of contact during retraction. For all experiments, a cantilever speed of 2 μm s^{-1} was used. To ensure axisymmetric contact between probe and sample, force maps (spatially resolved force-distance curve) were collected, giving a topographical image of the particle. From this force map, a set of about 10 F−D curves that are closest to the apex of the sample are picked for further evaluation (Figure 25). For each temperature, a set of particles was probed before the temperature was increased. Subsequent validation of the InvOLS was performed before and after each measurement.

Mechanic and Adhesion Evaluation:

All raw data measured as the movement of the z-piezo and the deflection signal of the cantilever on the segmented photodiode were processed in a homemade IgorPro procedure. First, the deflection of the cantilever in the noncontact regime was set to zero by rotating the F−D curve. The contact point between probe and sample was determined by the onset of a restoring force in the approach direction and set to zero deformation. The pure deformation of the sample was calculated by subtracting the absolute deflection of the cantilever, given by the product of measured photodetector signal and the InvOLS, from the piezo movement in contact. Finally, the deflection signal in volt of the photodetector is transformed to force by multiplication with the InvOLS and the spring constant.

The elastic modulus was determined by fitting the F−D curve up to a deformation of 500 nm by the Hertz equation (eq. 50). This deformation range includes sufficient data points for proper fitting and ensures that the underlying core layer has no direct mechanical influence. Typically, underlying layers are assumed to only influence the Young's modulus determination if the deformation is larger than 10% of the film thickness.[71] Our core-shell microgels exhibit a minimum shell thickness of 7 μm, which is significantly larger than the maximal deformation of just 0.5 μm in AFM. During the fitting, the first 50 nm of deformation were not considered because the forces associated with these small deformations are low, resulting in a high contribution to the experimental error. In addition to the visual control of the fits, only measurements with a contact exponent in F−D between 1.45 and 1.55 were considered for averaging. For each elastic modulus, an error was calculated by solving eq. 50 for E and performing error propagation in the fit range. For this purpose, the residual of the fit and measurement was used as a variable parameter. Further, constant errors for the colloidal probe radius of ±0.5 μm and 10% for the InvOLS as well as the spring constant were considered.
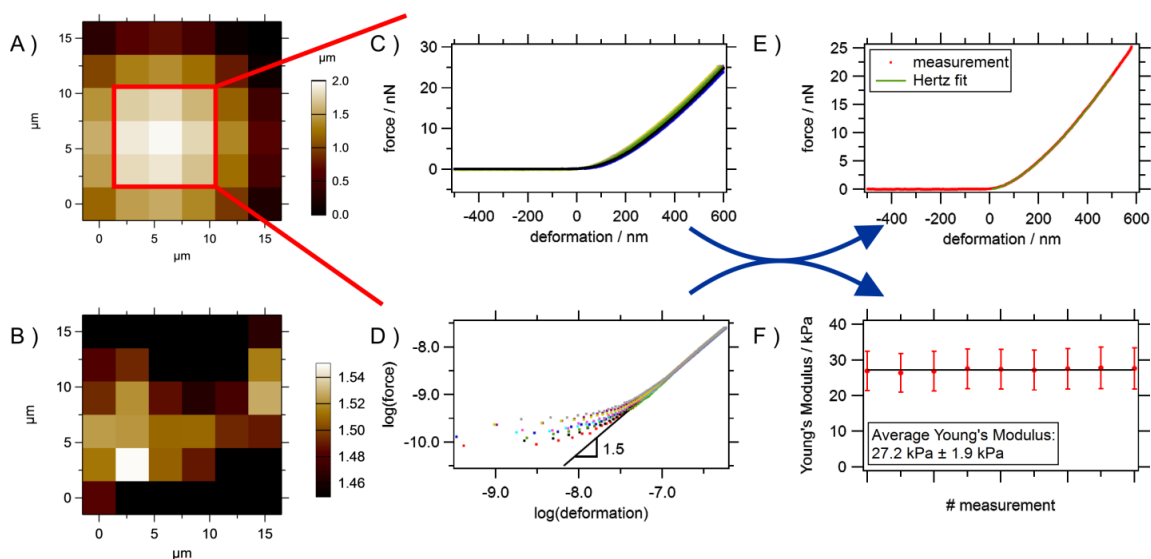
Figure 25   AFM force spectroscopy data acquisition, evaluation, and validation of axisymmetric contact of the probe and the sample. All data shown were recorded at a constant temperature of 32 °C. A) AFM height image of one core-shell microgel particle recorded as a force-map (at every pixel, a single force-deformation curve is recorded) with a colloidal probe ($R_{probe} = 1.7$ μm). Recording such force maps is essential to ensure axisymmetric contact, since bare optical alignment of the probe with an inverted optical microscope, also done here prior to recording the force map, would typically result in force–deformation curves recorded at positions 0 μm x 0 μm, 0 μm x 15 μm, or the center of the force map. Furthermore, note that the force map shown is already recorded by applying x–y piezo offsets to the cantilever to finally record the apex of the sample sphere. C) Nine force–deformation curves (approach) selected from the force-map shown in A) from the apex of the sample and the first neighbors as indicated with the red square in A). All curves are very uniform and show the typical exponential behavior in contact. D) Double logarithmic plot of the 9 force-deformation curves in contact to examine the power-law dependence. For all curves, a power-law exponent very close to 1.5, as indicated by the black line, is determined, which is characteristic for Hertzian contact of two spheres. B) Force-map image depicting the power-law exponent of every force-deformation curve recorded. The color-code is chosen between 1.45 and 1.55, indicating the range where Hertzian contact is assumed within this study. Close to the apex of the sample, almost every curve falls within the theoretical range, but away from the apex the contact exponents drop to smaller values indicating that the Hertz model should not be applicable. E) Force-deformation profile (red dots) of one of the selected curves in C) with a fit to the Hertz model in green. F) Determination of the Young's modulus by the Hertz model for the selected force-deformation curves recorded at the center of core-shell microgel particle. All nine measurements reveal uniform Young's modulus with an average value of (27.2 ± 1.9) kPa in this case. Reprinted with permission.[87] Copyright 2016 American Chemical Society.

The work of adhesion between probe and sample was determined by integrating the retraction part of force−deformation plots between zero force in contact (before minimum force) and the first point at which the baseline is reached again.

VI.3.   Results and Discussion

VI.3.1. Microfluidic Fabrication of pNIPAAm-pAAm Core-Shell Microgels

Our idea of preparing microgels with independently tunable elasticity is based on submillimeter sized gel particles with core-shell geometries. In previous work, microgels consisting of thermoresponsive polymer-gel shells that surround nonresponsive or

differently responsive polymer gel cores have been fabricated with colloidal sizes by seed-microgel precipitation polymerization[153] and with above-colloidal sizes by microgel encapsulation in droplet-based microfluidics.[160] We adopt the latter approach to form above-colloidal core-shell microgels, each consisting of a thermosensitive core surrounded by a non-thermos-sensitive shell. To realize this idea, core microgels consisting of cross-linked pNIPAAm are first made by droplet-based microfluidic templating at (23 ± 1) °C. For this purpose, we use polydimethylsiloxane (PDMS) microfluidic device with a single flow-focusing cross-junction geometry to fabricate monodisperse pre-microgel droplets of a NIPAAm solution (100 g L^{-1}) containing 1.36 g L^{-1} of N,N′-methylenebis(acrylamide) (BIS) as a cross-linker. Subsequent cross-linking copolymerization of these monomers within the droplets yields pNIPAAm microgels in the size-range of 20 µm in radius (Figure 26 A, B). After fabrication of these pNIPAAm microgels, we pack them by sedimentation and then use the resulting microgel paste in a second microfluidic step, wherein which they are encapsulated into surrounding non-thermo-sensitive polymer shells to form the anticipated core-shell particles.

To obtain a non-thermo-sensitive polymer for wrapping the thermosensitive pNIPAAm microgels, we synthesize photo-cross-linkable polyacrylamide (pAAm). This is
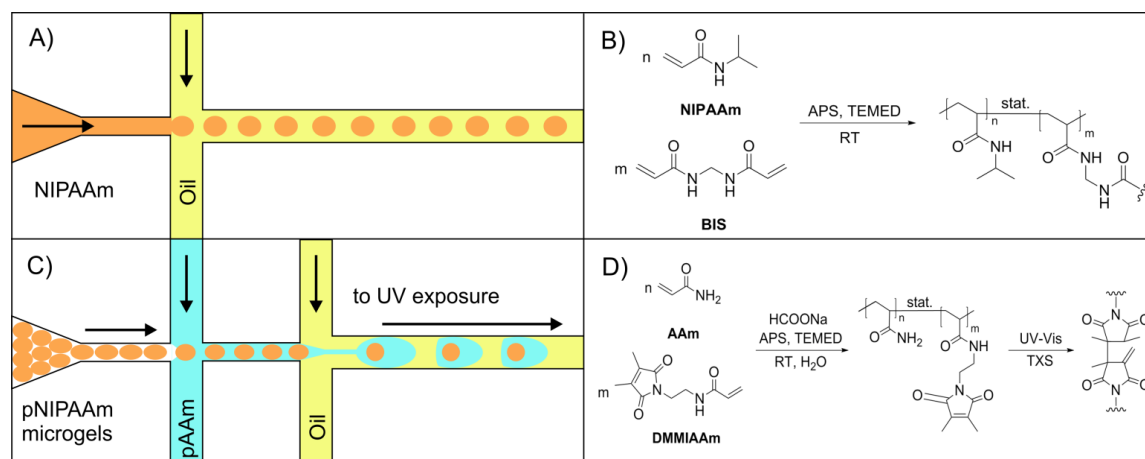
Figure 26 Preparation of core-shell microgels that each consist of thermo-responsive poly(*N*-isopropylacrylamide) (pNIPAAm) hydrogel core and a non-thermo-responsive polyacrylamide (pAAm) hydrogel shell by droplet-based microfluidics. A), B) pNIPAAm microgels are first prepared by emulsification of an aqueous solution of monomeric NIPAAm and the crosslinker BIS by an external phase of paraffin oil in a microfluidic device with a single flow-focusing cross-junction geometry. C), D) Core-shell microgels are subsequently prepared in a microfluidic device with sequential double cross-junction geometry. In the first junction, the pNIPAAm microgels from the preceding experiment are wrapped by a solution of pre-polymerized p(AAm-*co*-DMMIAAm) and the photosensitizer TXS. In the second junction, pre-core–shell microgel droplets are formed by emulsification of the resulting fluid stream with paraffin oil, which are then photo-gelled by UV irradiation.[163] Reprinted with permission.[87] Copyright 2016 American Chemical Society.

done by radical copolymerization of acrylamide with the photochemically dimerizable comonomer dimethylmaleinimidoacrylamide (DMMIAAm, 1.3 mol % rel. to AAm),[163-165] employing sodium formate as a chain transfer agent for molecular weight control.[166] The resulting polymer is then used in a consecutive microfluidic experiment conducted in a device with two sequential cross-junction channels, again at (23 ± 1) °C. In the first junction, the prefabricated pNIPAAm microgels are surrounded by a stream of a semidilute solution (100 g L^{-1}) of the photo-cross-linkable polyacrylamide, along with a triplet photosensitizer, thioxanthone-2,7-disulfonate (TXS).[163] In the second junction, this fluid stream is flow-focused by immiscible paraffin oil, thereby creating core-shell droplets, each containing a single pNIPAAm microgel. Whereas the position of the core inside the shell is not controllable in this process, the distribution of particle sizes resulting from the two consecutive microfluidic experiments are narrow and well-defined. Subsequent UV irradiation of these droplets gels their pAAm polymer shells, thereby yielding pNIPAAm−pAAm core-shell microgels (Figure 26 C, D). If this experiment is conducted such that the shell gel point is passed not before some diffusive interpenetration of the shell polymer into the core microgel, the resulting core-shell microgels are obtained with interconnected core and shell, as illustrated in Figure 24. After the microfluidic experiment, the core-shell microgels are removed from the templating emulsion and washed with water, wherein which they swell to equilibrium sizes. While the core size is determined by the first microfluidic experiment, the shell thickness can be adjusted by the flow rates as well as the microchannel geometry in the second microfluidic experiment.

VI.3.2. Optical Characterization

We focus our study on two batches of core-shell microgel particles, each prepared with the same pNIPAAm cores but with different shell thicknesses. Additionally, plain pNIPAAm microgels taken from the core microgel stock, and plain pAAm microgel particles templated from the shell-polymer solution in a microfluidic experiment as shown in Figure 26 A that is conducted at conditions as used during the second core-shell batch formation, are used as references. Images of the microgels are taken by optical microscopy during stepwise variation of the temperature from 28 to 38 °C. For this purpose, the particles are immobilized on a glass surface by sedimentation, and measurements are performed in a fluid cell with included temperature control in water. At each temperature, the microgels are equilibrated with their environment for at least 30 min. From these images, the core and shell radii of the microgels are determined. A temperature-
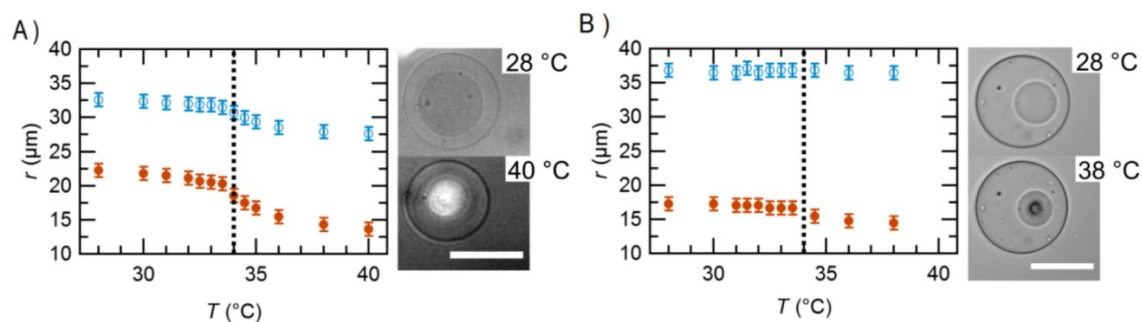
Figure 27   Temperature (*T*) dependent radii (*r*) of pNIPAAm–pAAm core-shell microgel particles in water, along with light microscopy images recorded at 20× magnification. Open blue circles represent the total particle radius, whereas full red circles represent the core radius. The lower critical solution temperature (LCST) is indicated by a dashed vertical line. Scale bars in the micrographs represent 50 μm. A) For particles from batch 1, the overall particle size decreases above the LCST, because the non-thermo-responsive shell gets dragged to follow the deswelling of the core. B) By contrast, a temperature-independent overall particle radius is observed for batch 2 although the core still deswells above the LCST. Reprinted with permission.[87] Copyright 2016 American Chemical Society.

independent average radius of (32.6 ± 1.5) μm is found for 9 plain pAAm particles. For an ensemble of 9 plain pNIPAAm particles, deswelling from an average radius of (23.2 ± 3.2) μm to (9.1 ± 1.1) μm is observed when the temperature increases from 28 to 38 °C. Out of a total of 18 core-shell particles investigated, Figure 27 A, B shows the deswelling curves for two representative microgel particles from batch 1 (A) and 2 (B), with the core radius and the total particle radius as a function of temperature. Deswelling curves of further core-shell particles and the reference particles are compiled in the Supporting Information (Figure S1) of the original publication.[87]

In batch 1, we find core-shell particles with core radii between 18 and 23 μm and a relatively thin shell between 8 and 14 μm thickness at 28 °C. As the core positions exhibit some variation and asymmetry in the ensemble of particles, we refer to the average values of the shell thickness, which are calculated from the core and shell diameters irrespective of the core position within the shell. While increasing the temperature, the typical LCST behavior of pNIPAAm is observed for the core, resulting in a decrease of its radius. For example, the particle shown in Figure 27 A exhibits such a decrease of its core radius down to 14 μm at 40 °C. The core deswelling is accompanied by a decrease of the entire particle radius by 5 μm. As a consequence of the more pronounced deswelling of the core compared to the effect on the overall particle radius, the pAAm shell gets radially stretched by ~3.5 μm; its total volume, however, reduces to 78% of its original value during this process. Similar behavior is found for all particles from this batch. The second batch of core-shell microgels contains particles with a larger total radius ranging from 35 to 37 μm and smaller core radii between 15 and 20 μm below the LCST. Consequently, the pAAm shell of the

second batch is on average twice as thick as in batch 1. Again, the typical deswelling of the pNIPAAm core is observed at increasing temperature, as shown for one representative core-shell particle in Figure 27 B. In contrast to the first batch, however, the entire particle radius does not change with temperature for all particles of this batch. Thus, the shrinking of the core in the batch-2 particles appears to be compensated by the stretching of the shell toward the particle interior. In the case of the core-shell particle shown in Figure 27 B, a shell stretching of 2.5 μm is observed.

The temperature-dependence of the size of the pNIPAAm−pAAm core-shell microgel particles indicates that the shell thickness is a relevant design parameter: although the LCST based deswelling of the core is comparable for both batches, a thin shell is more prone to follow this deswelling than a thick shell.

VI.3.3. Thermosensitive Change of the Microgel Young's Moduli

To quantify the surfacial mechanical properties of the core-shell microgels, we probe them by indentation exerted by atomic force microscopy (AFM) using the colloidal probe technique.[113] With this method, temperature-dependent changes of the microgel Young's modulus can be determined with high accuracy. After equilibration at a given temperature for at least 30 min, a silica sphere of 23 μm radius (in the case of the plain pNIPAAm particles) or 2 μm radius (in the case of the plain pAAm and the core-shell particles) fixed at the freestanding end of the cantilever is aligned centrically above the microgel particle under optical control with an inverted optical microscope. Then, approach−retract cycles are performed at a constant speed of 2 μm s^{-1} to record force−deformation (F−D) curves. In addition to optical control, axisymmetric contact of the microgel and the spherical probe is ensured by sampling a spatially resolved grid of F−D curves, resulting in a topographical image of the microgel (Figure 25). Then, the temperature is increased stepwise, and the measurements are repeated for exactly the same particles. To establish a reference system for the mechanical properties of our core-shell microgel particles, we first investigate plain pNIPAAm and plain pAAm microgel particles at varying temperatures. Figure 28 depicts representative F−D measurements on one pAAm as well as on one pNIPAAm particle at five different temperatures. The microgel stiffness is reflected by the slope of the F−D plots. It is almost temperature independent in the case of the plain pAAm particles, as indicated by very similar F−D data sets (Figure 28, dashed lines) in the investigated temperature range. By contrast, the F−D curves recorded on the plain pNIPAAm microgels become drastically steeper with
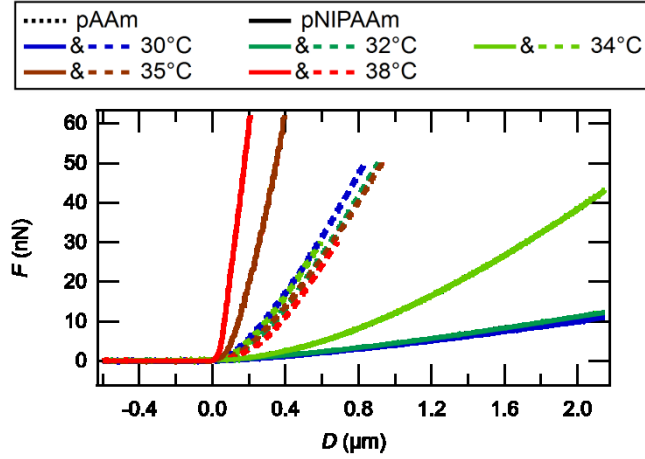
Figure 28   Temperature-dependent force (*F*) vs. deformation (*D*) measurements performed on plain pNIPAAm (solid lines) and plain pAAm (dashed lines) microgel particles as a reference. For each type, representative approach measurements in the range between 30 and 38 °C (temperature is color-coded) are shown for one particle. The stiffness of the pAAm particles is almost independent of the temperature, as indicated by their very similar behavior under load. By contrast, temperature-dependent stiffening is observed for the pNIPAAm particles while exceeding the LCST. Reprinted with permission.[87] Copyright 2016 American Chemical Society.

increasing temperature, reflecting the microgel deswelling and stiffening.[120] To quantify the mechanical properties, several theories modeling contact mechanics are available.[72, 77, 78, 83] In the field of colloidal probe force spectroscopy, the Hertz model and the Johnson−Kendall−Roberts (JKR) theory are frequently used. Both theories describe the contact formation and elastic compression of two isotropic spherical bodies under external axisymmetric load. The Hertz model neglects interparticle forces such as adhesion or friction, whereas additional stress contributions due to adhesion forces within the contact area are accounted for in the JKR theory, which transitions into the Hertz equation as adhesion vanishes. Because the measured adhesion forces between both types of homogeneous microgels and the colloid probe are small, the Hertz model is used in this study:

$$F = \frac{4}{3}ER^{1/2}D^{3/2} \tag{50}$$

with

$$\frac{1}{R} = \frac{1}{R_1} + \frac{1}{R_2} \tag{51}$$

$$\frac{1}{E} = \frac{1 - {v_1}^2}{E_1} + \frac{1 - {v_2}^2}{E_2} \tag{52}$$

In equation 50, the applied force, F, is related to the measured deformation, D, by a characteristic power of 1.5 and some effective parameters of the system, which are the

radius, R, and the elastic or Young's modulus, E, as given by equations 51 and 52. The indexes in these equations refer to the two materials in contact, and ν is the Poisson ratio, which is assumed to be 0.5 for incompressible isotropic elastic materials. In our study, we limit the mechanical characterization to the small deformation regime below 500 nm to avoid plastic effects and only probe the surficial properties of the microgels. Such small deformation is also beneficial to minimize the potential complex influence of the asymmetry of the core-shell geometries on the interaction forces. The validity of the Hertz model for each F−D experiment is assumed when its power-law dependence falls in the range between 1.45 and 1.55, according to equation 50 (Figure 25). The resulting Young's moduli for plain pAAm and pNIPAAm microgel particles and their thermoresponsive swelling−deswelling are shown in Figure 29. As expected, the Young's modulus of the plain pAAm microgel particles (Figure 29, squares) is found to be insensitive to temperature, with values in the range from 20 to 50 kPa. The scattering of the data is assumed to be an unfavorable artifact due to a broad distribution of the conversion of the photocrosslinking reaction achieved during the consecutive microfluidic experiment. In contrast, the plain pNIPAAm microgels are found to be softer, with a modulus of just around 1 kPa at low temperatures, but they stiffen up to 250 kPa at temperatures above the LCST. The variation in the apparent LCST for the three pNIPAAm particles shown in Figure 29 is probably due to temperature gradients within the setup of the liquid cell in the AFM. Besides the variation in the absolute values of the Young's modulus for both systems, their relative temperature-induced changes are characteristic for both systems. The values for plain pAAm remain constant with
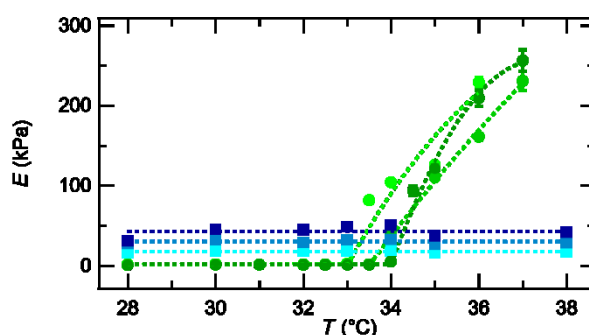
Figure 29   Temperature (*T*) dependent Young's moduli (*E*) of single plain pNIPAAm (green circles) and plain pAAm (blue squares) microgel particles recorded by colloidal probe AFM. Dashed lines are to guide the eye. Each point represents the average value of at least five F–D measurements. Values for the Young's modulus of three different particles are shown for each system. In the case of pAAm, the Young's modulus is temperature independent and in the range of 20 to 50 kPa. Contrary, at low temperatures, the Young's modulus of pNIPAAm is around 1 kPa and increases up to 250 kPa above the LCST (33–34°C). Reprinted with permission.[87] Copyright 2016 American Chemical Society.
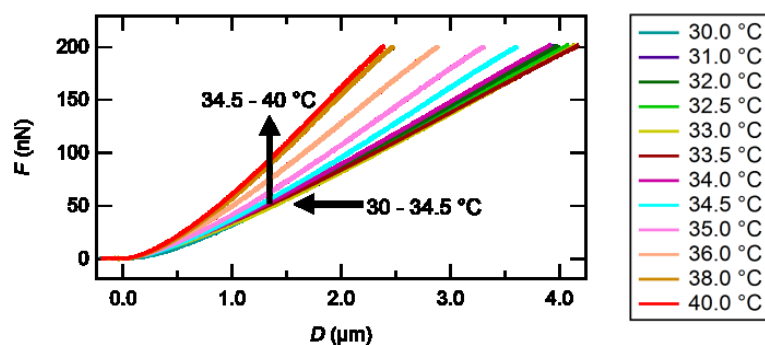
Figure 30   Force (F) vs. deformation (D) measurements conducted on one pNIPAAm–pAAm core-shell microgel particle with temperature-controlled colloidal probe AFM. Temperatures are color-coded as denoted in the legend. As indicated with the horizontal arrow, the deformability of the particle first stays constant between 30 and 34.5 °C. Upon further heating that causes deswelling of the pNIPAAm core beyond 35 °C, however, the core-shell particle gradually stiffens with increasing temperature, as highlighted by the vertical arrow. Reprinted with permission.[87] Copyright 2016 American Chemical Society.

temperature, whereas plain pNIPAAm particles stiffen by 2 orders of magnitude upon temperature increase.

After establishing the plain-microgel reference system, we focus on our core-shell microgel particles. The F−D data recorded on these microgels are nearly identical if the temperature is below the LCST of pNIPAAm, as shown in Figure 30 for one particle. This is because both hydrogel materials do not show appreciable thermal sensitivity in this temperature range. Upon exceeding the LCST, however, a change of the mechanical response is observed: in this temperature range, gradual steepening of the F−D curves is recognized while the temperature is raised to 40 °C. This is a first indication that the temperature-responsive microgel core mechanically affects the per-se non-thermo-sensitive microgel shell. Following this qualitative interpretation, quantification of these mechanical changes is desired to compare the core-shell microgel thermo-mechanical response to that of their plain hydrogel components. Classical theories such as the Hertz and JKR models, however, are derived on the assumption of homogeneous isotropic bodies. Following earlier work of finite element simulations on comparable soft core-shell particles that indicate a good estimation of the effective elastic modulus by the Hertz theory,[86] we apply equation 50 in the small deformation regime for mechanical quantification. The validity of this approach is further supported by the resulting elastic moduli in the low kPa range and the measured F−D power-law dependence (Figure 25). Elastic moduli estimated for representative core-shell particles from both batches in the small deformation regime (<500 nm) are shown in Figure 31. In this deformation regime, only the elastic contributions of the shell material are measured. At low temperatures, the Young's modulus for both particles is temperature-independent. Above the LCST of the encapsulated core,
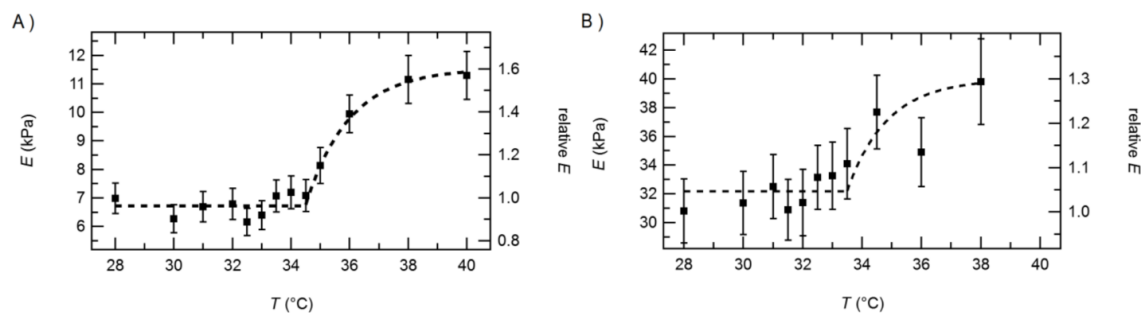
87

Figure 31 Temperature (*T*) dependent Young's moduli (*E*) of the two pNIPAAm–pAAm core-shell microgel particles shown in Figure 27 at varying temperatures. Each data point represents averaged values of at least five F–D curves, and the dashed lines are a guide to the eye. Absolute values of the Young's modulus are plotted to the left axis. Relative changes in Young's modulus are given by the right axis. Values measured on one core-shell particle of batch 1 are shown in A) and one particle of batch 2 in B), respectively. Reprinted with permission.[87] Copyright 2016 American Chemical Society.

however, a nonlinear increase of the elastic modulus of the shell is observed for both core-shell particles. Furthermore, the absolute values of representative particles below the LCST differ strongly with (6.7 ± 0.2) kPa for Figure 31A and (32.2 ± 0.4) kPa for Figure 31B. Both trends hold as well for statistical analysis of several particles (see Supporting Information Figure S3)[87]. As discussed in the context of Figure 29, the differences in the absolute Young's moduli of the pAAm shells are presumed to be due to a varying extent of photo-cross-linking achieved during the core-shell microgel preparation. In the following, we therefore focus on a discussion of the relative temperature-induced changes.

We interpret the elasto-thermal effect of the per-se nonresponsive pAAm-shell with the following conceptual picture comprising two scenarios depicted in Figure 32. In both scenarios, a redistribution of the shell polymer network is triggered by the temperature-induced shrinking of the core. Because of the interconnection between the core- and the shell network in the microgels, the deswelling core drags the shell toward the center of the core. In the first scenario (Figure 32 A), which corresponds to the situation observed for batch 1, the total particle radius reduces with temperature. As a result, the shell volume reduces, and water is squeezed out of the shell. This observation agrees with earlier experimental results and model calculations for core-shell colloidal hydrogels by Richtering et al.[155, 159] In this earlier work, it is conceived that thin swollen shells are subject to lateral contraction exerted by a collapsing core, which reduces the shell size. Although this model does not focus on mechanical changes induced by that, one can deduce from the shell-volume reduction that the polymer concentration in the shell is increased during this process. According to the Flory−Rehner theory,[167, 168] this leads to an increase of the elastic modulus of the polymer gel, which would explain the observed stiffening of
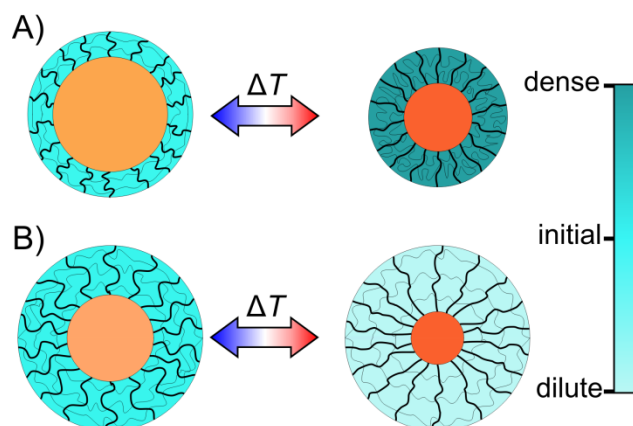
Figure 32 Schematic illustration of the changes in the pAAm shell polymer network upon deswelling of the pNIPAAm core at increasing temperature. The polymer chains in the shell are not drawn to scale, but sketched such to illustrate their radial stretching and the change of their segmental density upon core deswelling. Darker colors indicate an increased polymer concentration. In A), the deswelling of the core results in a decreasing total particle radius, release of water out of the shell network to the surrounding environment, an increasing polymer density, and radial stretching of the network. In B), by contrast, the total particle radius stays constant, the shell polymer density decreases, but still the network is radially stretched. Reprinted with permission.[87] Copyright 2016 American Chemical Society.

the particles in batch 1 of our work. The second scenario, schematically depicted in Figure 32 B, focuses on particles that do not change their total size upon core collapse, which is typical for batch 2. Here, the reasons for the observed stiffness changes are less clear. They could be induced by radial stretching of the shell polymer network toward the shrinking core. Again, this assumption is supported by earlier core-shell microgel modeling by Gernandt and Richtering.[159] Their model predicts that close to the interface of a collapsed core, the shell is predominately laterally contracted. With increasing distance from the interface, the radial stretching of the shell outweighs this lateral contraction due to decreasing mechanical stresses from the core and due to the swelling tendency of the shell. As a result, hydrogels with thicker shells - as our particles from batch 2 - mainly experience radial stretching. A possible explanation for a mechanical stiffening resulting from this stretching could be that the shell polymer segments between cross-links become more rigid due to a loss of entropy upon stretching, thereby increasing the elastic modulus.[169]

In general, the magnitude of radial stretching and lateral contraction of the shell polymer chains might be further influenced by the network constitution, which is primarily determined by parameters such as its initial cross-linking density and the spatial distribution of cross-links within the shell. We do not have direct information on these parameters on a single-particle level, but yet the general trends seem to hold.

VI.3.4. Interfacial Interaction

Plain pNIPAAm hydrogel particles exhibit conjoint changes of both their mechanical and their adhesion properties upon the thermoresponsive volume phase transition.[120] By contrast, the interfacial properties of pAAm hydrogels are supposed to be temperature-independent in the range covered in our study, which should result in constant adhesive properties. We therefore presume that the interfacial properties of our core-shell microgel particles should be constant and decoupled from their mechanical switchability shown above.

To investigate this hypothesis, we analyze the F−D curves recorded during retraction of the sphere to determine adhesion forces and energies. If present, adhesive interaction forces cause an attraction between the silica probe and the hydrogel particles, which becomes dominant when the loading force of the cantilever vanishes during retraction. Upon further retraction of the probe, the adhesive attraction between the surfaces causes them to stick together, resulting in a net negative force measured. The sphere stays in contact with the surface until the cantilever force overcomes the adhesion force, and the probe jumps out of contact.

Often, the negative force maximum is used to describe the adhesion. A more global measure of adhesion is the total energy needed to pull the probe off the surface, which is referred to as the work of adhesion. It equals the area enclosed by the negative part of the force curve and the abscissa (Figure 33 A, blue shaded area). The adhesive properties of
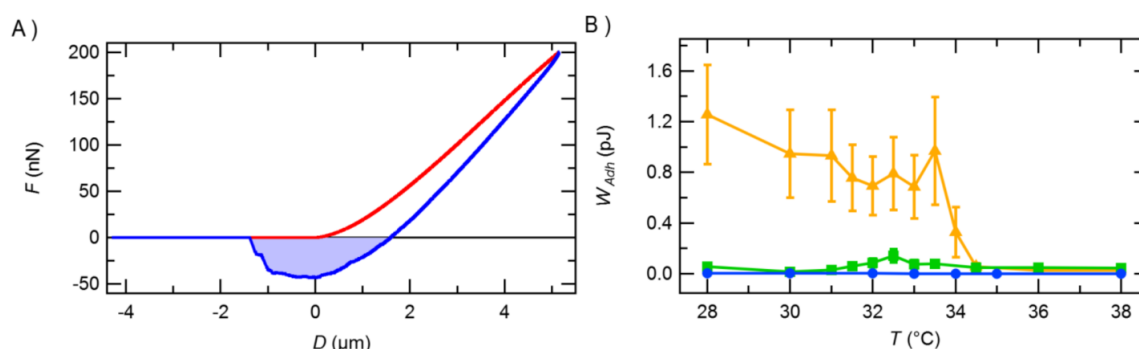
Figure 33   Adhesion properties of plain and core-shell microgels against a spherical silica probe measured by AFM. A) Force (F) vs. deformation (D) upon approach (red line) and retraction (blue line) recorded on a core-shell particle. The blue shaded area enclosed by the force curve and the abscissa represents the work of adhesion required to remove the probe from the sample. B) Work of adhesion (W_{Adh}) for plain pAAm (blue circles), plain pNIPAAm (orange triangles), and pAAm–pNIPAAm core-shell (green squares) microgels at varying temperatures (T). The data points represent the averaged values of 17 core-shell, 9 plain pAAm, and 8 plain pNIPAAm particles, while for each particle and temperature combination at least 20 F–D curves were evaluated. Reprinted with permission.[87] Copyright 2016 American Chemical Society.

the three different microgel systems as a function of temperature are presented in Figure 33 B. Starting at low temperatures, a high work of adhesion of (1.25 ± 0.39) pJ between the hydrophilic swollen plain-pNIPAAm microgel particles and the hydrophilic silica probe is measured at 28 °C. While increasing the temperature, the adhesion only slightly decreases. The imminent collapse of the hydrogel particles can be noticed as a first drop in the work of adhesion before reaching the lowest value at 38 °C. The temperature-dependent adhesion of pNIPAAm was studied by many researchers. Both decrease[170, 171] and increase[172-174] of the adhesion with increasing temperature were reported, depending on the properties of the interacting surfaces and the experimental setup.

For the plain pAAm hydrogel particles, the work of adhesion is very low, $(2.82 \pm 0.24) \times 10^{-3}$ pJ, and it is not affected by temperature variation. In contrast to the two-order-of magnitude changes of the adhesive properties of the plain pNIPAAm microgels, the work of adhesion estimated for the core-shell particles stays nearly constant at low values over the whole temperature range probed. We do not find any significant change between 28 and 38 °C with a work of adhesion of (0.56 ± 0.26) pJ and (0.44 ± 017) pJ, respectively. Thus, the adhesion behavior of the core-shell-system appears to be dominated by the shell layer and hardly affected by temperature changes.

VI.4.   Conclusion

Core-shell microgels that consist of a thermoresponsive pNIPAAm core and a nonresponsive pAAm shell exhibit tunable elastic properties. This is achieved by chemical or topological interconnection between their cores and shells, transferring the collapse of the core to a surficial stiffening of the shell at elevated temperatures. The deswelling core drags the cross-linked shell inward, thereby changing the shell volume and polymer segmental concentration, and radially stretching the shell network. For a given core size and composition, we find that the relative shell stiffening is more effective for particles with a thinner and softer shell. In the case of thicker and more rigid shells, the surficial stiffening gets attenuated but is still present. In contrast to plain-pNIPAAm microgels, these effects occur without marked changes in the outer microgel hydrophilicity, and the adhesiveness remains constant. Hence, these composite microgels exhibit an independently tunable elasticity without accompanying a change of other relevant parameters. Further correlating the impact of the core-collapse and the core interconnection properties with the

shell to the mechanical stiffening might be used to design rationally assemblies of microgel layers or aggregate-substrates with the ability to independently regulate their elasticity.

VI.5.   References

[71] H.-J. Butt, B. Cappella, M. Kappl, *Surface Science Reports* **2005**, *59*, 1.

[72] H. Hertz, *Journal für die reine und angewandte Mathematik* **1882**, 1882, 156.

[77] K. L. Johnson, K. Kendall, A. D. Roberts, *Proceedings of the Royal Society of London Series a-Mathematical and Physical Sciences* **1971**, 324, 301.

[78] B. V. Derjaguin, V. M. Muller, Y. P. Toporov, *Journal of Colloid and Interface Science* **1975**, *53*, 314.

[83] D. Maugis, Journal of Colloid and Interface Science **1992**, 150, 243.

[86] H. M. Pan, M. Seuss, M. P. Neubauer, D. W. Trau, A. Fery, *ACS Applied Materials & Interfaces* **2016**, *8*, 1493.

[87] M. Seuss, W. Schmolke, A. Drechsler, A. Fery, S. Seiffert, *ACS Applied Materials & Interfaces* **2016**, *8*, 16317.

[96] M. Delcea, S. Schmidt, R. Palankar, P. A. L. Fernandes, A. Fery, H. Moehwald, A. G. Skirtach, *Small* **2010**, *6*, 2858.

[100] R. Hartmann, M. Weidenbach, M. Neubauer, A. Fery, W. J. Parak, *Angewandte Chemie International Edition* **2015**, *54*, 1365.

[113] W. A. Ducker, T. J. Senden, R. M. Pashley, *Nature* **1991**, *353*, 239.

[120] S. Schmidt, M. Zeiser, T. Hellweg, C. Duschl, A. Fery, H. Moehwald, *Advanced Functional Materials* **2010**, *20*, 3235.

[125] J. L. Hutter, J. Bechhoefer, *Review of Scientific Instruments* **1993**, *64*, 1868.

[130] H. G. Schild, *Progress in Polymer Science* **1992**, *17*, 163.

[131] Y. Okada, F. Tanaka, *Macromolecules* **2005**, *38*, 4465.

[132] Y. H. Bae, T. Okano, S. W. Kim, *Journal of Polymer Science Part B-Polymer Physics* **1990**, *28*, 923.

[133] C. Erbil, Y. Yildiz, N. Uyanik, *Polymer International* **2000**, *49*, 795.

[134] K. Dušek, Patterso.D, *Journal of Polymer Science Part a-2-Polymer Physics* **1968**, 6, 1209.

[135] Y. Li, T. Tanaka, *Journal of Chemical Physics* **1989**, *90*, 5161.

[136] Y. Li, T. Tanaka, *Annual Review of Materials Science* **1992**, *22*, 243.

[137] S. Hirotsu, *Phase Transitions* **1994**, *47*, 183.

[138] J. Zhang, R. Pelton, Y. L. Deng, *Langmuir* **1995**, *11*, 2301.

[139] H. Kanazawa, K. Yamamoto, Y. Matsushima, N. Takai, A. Kikuchi, Y. Sakurai, T. Okano, *Analytical Chemistry* **1996**, *68*, 100.

[140] Y. Hirose, T. Amiya, Y. Hirokawa, T. Tanaka, *Macromolecules* **1987**, *20*, 1342.

[141] C. Wu, S. Q. Zhou, *Macromolecules* **1997**, *30*, 574.

[142] A. Fernandez-Barbero, A. Fernandez-Nieves, I. Grillo, E. Lopez-Cabarcos, *Physical Review E* **2002**, *66*, 051803.

[143] H. Senff, W. Richtering, *Journal of Chemical Physics* **1999**, *111*, 1705.

[144] J. Z. Wu, B. Zhou, Z. B. Hu, *Physical Review Letters* **2003**, *90*, 1.

[145] M. Stieger, J. S. Pedersen, P. Lindner, W. Richtering, *Langmuir* **2004**, *20*, 7283.

[146] G. Romeo, A. Fernandez-Nieves, H. M. Wyss, D. Acierno, D. A. Weitz, *Advanced Materials* **2010**, *22*, 3441.

[147] S. Hirotsu, *Macromolecules* **1990**, *23*, 903.

[148] S. M. Hashmi, E. R. Dufresne, *Soft Matter* **2009**, *5*, 3682.

[149] A. Burmistrova, M. Richter, M. Eisele, C. Uezuem, R. von Klitzing, *Polymers* **2011**, *3*, 1575.

[150] A. J. Engler, S. Sen, H. L. Sweeney, D. E. Discher, *Cell* **2006**, *126*, 677.

[151] E. C. Cho, J.-W. Kim, A. Fernandez-Nieves, D. A. Weitz, *Nano Letters* **2008**, *8*, 168.

[152] C. D. Jones, L. A. Lyon, *Langmuir* **2003**, *19*, 4544.

[153] C. D. Jones, L. A. Lyon, *Macromolecules* **2003**, *36*, 1988.

[154] X. Li, J. Zuo, Y. Guo, X. Yuan, *Macromolecules* **2004**, *37*, 10042.

[155] I. Berndt, J. S. Pedersen, P. Lindner, W. Richtering, *Langmuir* **2006**, *22*, 459.

[156] M. Zeiser, I. Freudensprung, T. Hellweg, *Polymer* **2012**, *53*, 6096.

[157] S. M. Lee, Y. C. Bae, *Macromolecules* **2014**, *47*, 8394.

[158] H. Zhao, H. Chen, Z. Li, W. Su, Q. Zhang, *European Polymer Journal* **2006**, *42*, 2192.

[159] J. Gernandt, G. Frenning, W. Richtering, P. Hansson, *Soft Matter* **2011**, *7*, 10327.

[160] S. Seiffert, J. Thiele, A. R. Abate, D. A. Weitz, *Journal of the American Chemical Society* **2010**, *132*, 6606.

[161] J. C. McDonald, D. C. Duffy, J. R. Anderson, D. T. Chiu, H. K. Wu, O. J. A. Schueller, G. M. Whitesides, *Electrophoresis* **2000**, *21*, 27.

[162] K. P. Kronfeld, H. J. Timpe, *Journal Fur Praktische Chemie* **1988**, *330*, 571.

[163] S. Seiffert, W. Oppermann, K. Saalwaechter, *Polymer* **2007**, *48*, 5599.

[164] L. Ling, W. D. Habicher, D. Kuckling, H. J. Adler, *Designed Monomers and Polymers* **1999**, *2*, 351.

[165] C. D. Vo, D. Kuckling, H. J. P. Adler, M. Schohoff, *Colloid and Polymer Science* **2002**, *280*, 400.

[166] M. J. Fevola, R. D. Hester, C. L. McCormick, *Journal of Polymer Science Part a: Polymer Chemistry* **2003**, *41*, 560.

[167] P. J. Flory, J. Rehner, *The Journal of Chemical Physics* **1943**, *11*, 512.

[168] E. Geissler, A. M. Hecht, *Macromolecules* **1981**, *14*, 185.

[169] A. M. Oelker, S. M. Morey, L. G. Griffith, P. T. Hammond, *Soft Matter* **2012**, *8*, 10887.

[170] N. Ishida, M. Kobayashi, *Journal of Colloid and Interface Science* **2006**, *297*, 513.

[171] M. J. N. Junk, R. Berger, U. Jonas, *Langmuir* **2010**, *26*, 7262.

[172] M. C. LeMieux, S. Peleshanko, K. D. Anderson, V. V. Tsukruk, *Langmuir* **2007**, *23*, 265.

[173] I. B. Malham, L. Bureau, *Langmuir* **2010**, *26*, 4762.

[174] E. Svetushkina, N. Puretskiy, L. Ionov, M. Stamm, A. Synytska, *Soft Matter* **2011**, *7*, 5691.

VII. Polymerizing Like the Mussels Do: Toward synthetic mussel-foot proteins and resistant high-performance glues

The following chapter is in its entirety based on the research article of J. Horsch, P. Wilke, myself and others published in *Angewandte Chemie*, Volume 130, Issue 48, Pages 15954-15958 2018 and *Angewandte Chemie International Edition*, Volume 57, Issue 28, Pages 15728-15732 2018.[175, 176] It is reprinted with permission while the copyright is with the Wiley 2018. All schemes and figures are used as published as well as most of the text is reproduced. It was modified in some sections to be integrated in this thesis and expanded by content initially published in the connected Supporting Information.

VII.1. Introduction

For decades, mussel glues have offered inspiration for a variety of bio-mimetic materials.[50, 58, 177-179] Progress in understanding the mechanisms of the concerted self-assembly process of mussel foot proteins (mfps) that constitute the adhesion system led to the recognition of L-3,4-dihydroxyphenylalanine (Dopa) as a key moiety for adhesion.[55] This triggered a rich class of Dopa-carrying polymers with remarkable property profiles.[57, 180] Dopa could either be in-built directly into polymers, leading to instant adhesives or be enzymatically generated on demand by tyrosinase processing of tyrosine-bearing precursor polymers.[181-183] Besides the contribution of Dopa to adhesion,[184-186] the role for cohesion is increasingly recognized.[187] The latter occurs either non-covalently by Fe^{3+} cross-linking of Dopa,[188] or via a set of reaction mechanisms leading to covalent Dopa cross-linking.[189] Among those is the tyrosinase-induced Michael-type addition that constitutes an exploitable pathway for the establishment of a novel polymerization process. During the formation of byssal threads, polyphenol oxidase (PPO) converts L-Dopa residues in mfps into L-Dopaquinone[190] in a process that is referred to as quinone tanning. Cross-linking occurs by nucleophilic addition of protein side-chain functionalities[56] and one of the most effective pathways involves cysteine addition to L-Dopaquinones.[191, 192] Resulting cysteinyldopa cross-links are observed in various adhesive protein systems such as Pcfp-1 of *Perna canaliculus* and Mcfp-6 footprints of *Mytilus californianus*.[193, 194]

Herein we present our study on abstracting the cysteine–dopaquinone addition from mussel adhesive systems to polymerize peptides (unimers) via tyrosinase activation. The

enzyme-activated polyaddition exploits the formation of cysteinyldopa connectivities and leads to synthetic adhesive protein analogues.

VII.2. Results and Discussion

VII.2.1. Enzyme-Catalyzed Mussel-Foot Protein Polymerization

The mfp-1 family constitutes a tough and flexible coating of the byssal threads. In *Mytilus edulis*, the Mefp-1 sequence contains a highly repetitive decamer AKPSYPPTYK (Figure 34).[195] Hence, polymerization of this consensus sequence might result in a polymer that resembles Mefp-1 in some aspects. To create a unimer capable of cysteinyldopa polymerization, AKPSYPPTYK was extended C-terminally with Cys via a tri-glycine spacer, resulting in AKPS**Y5**PPT**Y9**KGGGC (U_2^C). Owing to the presence of two tyrosines, U_2^C would produce branched or cross-linked polymers. For ease of analysis, a linear polymer was anticipated by polymerizing a unimer that contains only Tyr9 as Tyr5 was replaced by Ser5 (AKPS**S5**PPT**Y9**KGGGC, U_1^C).
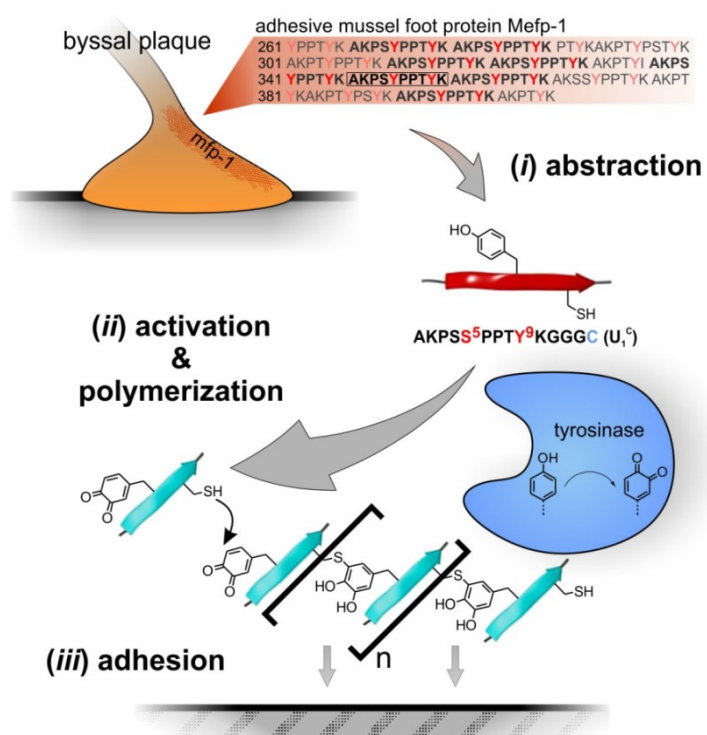
Figure 34 Principle of mussel-inspired polymerization. (*i*) An amino acid sequence is abstracted from Mefp-1 and extension with Cys leads to the unimer U_1^C. (*ii*) Polymerization of U_1^C can be triggered by enzymatic oxidation of tyrosine to Dopaquinone, which reacts with thiol moieties of Cys residues, enabling formation of cysteinyldopa linkages. (*iii*) The obtained artificial mfps exhibit strong adhesion to various substrates, making them useful for coatings or glues. Reprinted with permission.[175] Copyright 2018 Wiley-VCH.

Tyrosinase occurs almost ubiquitously throughout nature, is commercially available at low cost, and meets requirements for materials science applications.[196] To avoid batch-to-batch variations,[197] the enzymatic reactions were carried out with the active form of a recombinantly expressed tyrosinase (*Agaricus bisporus* polyphenol oxidase isoform 4, *Ab*PPO4).[196, 198] The *Ab*PPO4 belongs to the PPO family from mushrooms and proved to practically instantaneously oxidize the tyrosine residues of U_1^C and U_2^C to Dopa and Dopaquinone as confirmed by MALDI-TOF-MS indicating species with +16 Da and +14 Da mass differences compared to non-activated unimers (Supporting Information, Figures S1, S3)*. More importantly, mass spectrometry as a capable tool for polymer characterization[199] proves the rapid formation of polymerization products. MALDI-TOF-MS shows species reaching up to about 30 kDa for $polyU_1^C$ and about 25 kDa for $polyU_2^C$, which could be assigned to a degree of polymerization (DP) of up to 21 (Figure 35 b).

GPC analysis of $polyU_1^C$ revealed the formation of low- and high-molecular-weight fractions with apparent peak molecular weights of $M_{P,app.} \approx 20$ kDa and $M_{P,app.} \approx 530$ kDa, respectively. The fractions are already present after 5–10 min and correspond to $DP_{p,app.} \approx 15$ and 260, respectively. SDS PAGE confirmed the rapid formation of species with 10–25 kDa and suggests that the polymerization appears to be completed within 10 min, as no further band shifting is observed (Supporting Information, Figure S5)*. The high-molecular-weight fraction found by GPC was not resolved in SDS PAGE owing to the molecular weight cut-off of the gel. Interestingly, the analysis suggests a limitation in primary polymer growth to occur at a molecular weight of about 20–25 kDa. The higher molecular weight fraction is presumably a result of subsequent cross-linking by secondary reactions such as diDopa formation (Supporting Information, Section S5.12)*.

For $polyU_2^C$ rather related results are observed (Supporting Information, Figure S6)*. Considering the additional dispersity that is caused by branching, SDS PAGE analysis shows less defined, broader bands, which reach 100 kDa, though the main band also appears at about 20–25 kDa.

MALDI-TOF-MS/MS analysis of the U_1^C polymerization mixture confirmed that the growth mechanism is based on cysteinyldopa linkages (Supporting Information, Section S5.11)*. The U_1^C dimer species with m/z 2722.27–2726.30 was fragmented and confirmed the presence of a cysteinyldopa connectivity by showing required y and b fragmentation ions. Moreover, direct proof was provided by the molecular ions that result from the S-C_β bond cleavage of the cysteinyldopa species.

---

*see electronic supporting information for ref. [175]
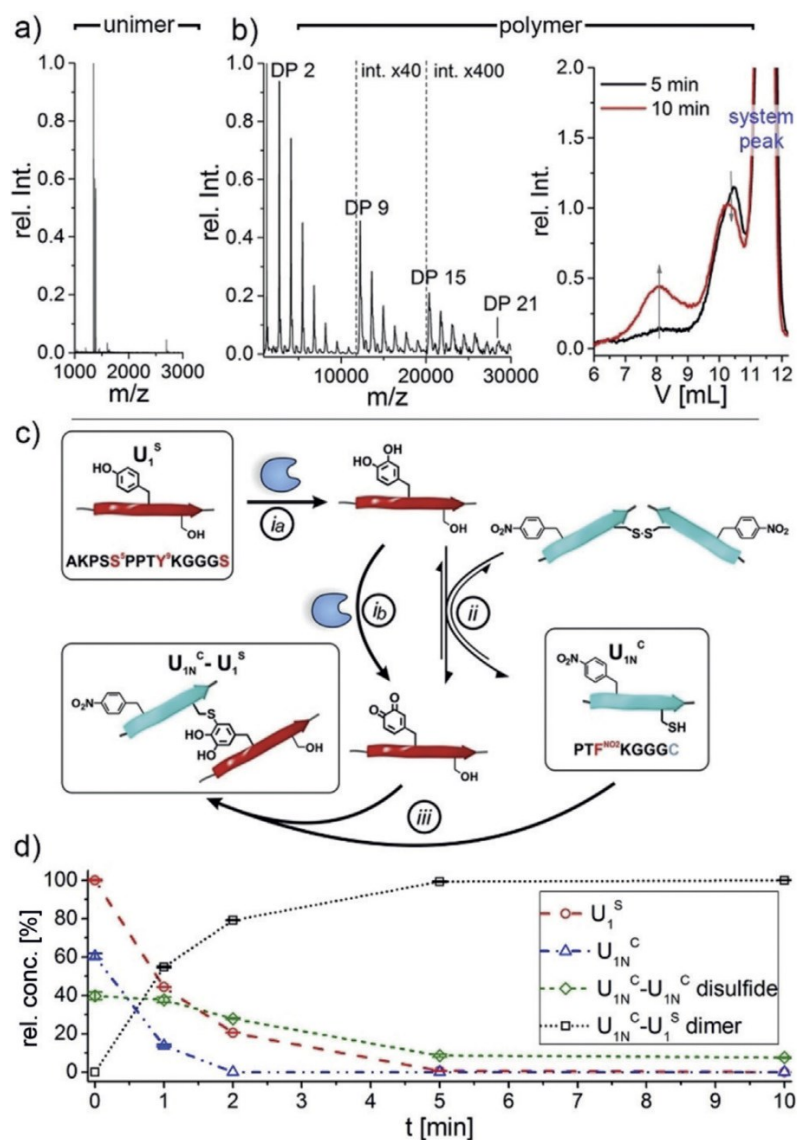
Figure 35 Enzyme-activated polymerization of U_1^C by tyrosinase to form polyU$_1^C$ (a,b) and model study revealing kinetics of tyrosinase-induced dimerization of U_1^S and U_{1N}^C (c,d). MALDI-TOF-MS of U_1^C at time zero (a) and of polyU$_1^C$ after 10 min (b, left). GPC traces of polyU$_1^C$ (b, right). c) Reaction pathway for the model dimerization shows enzymatic oxidation of tyrosine in U_1^S to Dopaquinone (i a, b), U_{1N}^C oxidation to disulfide by Dopaquinone reduction and the inverse reaction (ii) as well as U_{1N}^C-U_1^S dimer formation by cysteinyldopa linkage (iii). d) Relative concentrations of different species during model dimerization determined by HPLC kinetics. (Conditions: 0.25 mM of U_1^C and 0.26 mM U_{1N}^C (1/1.05, v/v) in pH 6.8 buffer, 50 mL^{-1} AbPPO4). Reprinted with permission.[175] Copyright 2018 Wiley-VCH.

The cross-linking reaction was investigated in a model dimerization of the monofunctional unimers AKPS**S5**PPT**Y9**KGGG**S** (U_1^S), which contains one tyrosine but no cysteine, and PTF**NO2**KGGG**C** (U_{1N}^C), which bears cysteine while tyrosine was replaced with p-nitrophenylalanine. The dimerization of U_1^S and U_{1N}^C occurs rapidly after enzymatic oxidation of U_1^S via cysteinyldopa formation. HPLC kinetics indicated the complete dimerization product formation within about 5 min, even at a marginal excess of U_{1N}^C (Figure 35 d).

* see electronic supporting information for ref. [175]

Interestingly, a secondary reaction pathway occurred, leading to the formation of the disulfide bridged symmetric dimers U_{1N}^C–U_{1N}^C. The presence of redox-active partners like Dopa/Dopaquinone is required to generate disulfides, as the control reaction of U_{1N}^C + U_1^S without tyrosinase has shown only 2.5% disulfide formation after 48 h (Supporting Information, Figure S16). Thiol oxidation to disulfide can be promoted by reduction of Dopaquinone to Dopa, as has been described for the rescue protein Mcfp-6, which restores Dopa functionalities under the oxidizing seawater conditions.[200] Considering this remarkable analogy, it is likely that the reduction of Dopaquinone leads to the formation of disulfide and Dopa (Figure 35 c, reaction *ii*). Intriguingly, the U_{1N}^C–U_{1N}^C dimer is not a dead end, since the redox potential of the reduction of disulfides by Dopa is close to that of the oxidation of thiol by Dopaquinone.[200] Thus, reaction *ii* remains reversible and U_{1N}^C can be regenerated to undergo the favored formation of cysteinyldopa linked U_{1N}^C–U_1^S dimers and drives the polymerization (reaction *iii*). Residual disulfide corresponds to the small excess of U_{1N}^C that was used to reach equivalency of effective functional groups.

The model system was further employed to illuminate potential secondary cross-linking routes. Upon enzymatic activation of U_1^S in the absence of U_{1N}^C, no polymer was detectable by SDS PAGE. This suggests the need for cysteine to enable polymerization and confirms the lower reactivity of ε-amino groups of Lys2 and Lys10 (Supporting Information, Figure S7)*. However, minor amounts of the dimerization product U_1^S–U_1^S were found after 1 h reaction time by MALDI-TOF-MS. ESI-LC-MS/MS confirmed the nature of the connectivity to be a 5,5'-diDopa linkage as directly associated fragment ions were observed (Supporting Information, Section S5.12)*. None of the y, b, c, and z ions or other fragments gave evidence for lysinyldopa links. Apparently, cysteinyldopa groups are less susceptible for further coupling reactions as no subsequent cross-linking of cysteinyldopa linked U_1^S–U_{1N}^C dimers was observed in a model reaction over 48 h. Conclusively, secondary cross-linking can occur via 5,5'-diDopa formation by unreacted Dopaquinones, which proceeds slower than producing the cysteinyldopa linkages. This evidence supports the hypothesis that the polymerization is driven by cysteinyldopa formation to generate primary polymerization products. These can further cross-link via secondary reactions to form high molecular weight fractions

VII.2.2. Coating Behavior Studied by Quartz Crystal Microbalance

One of the intriguing aspects of the polymerization is the generation of cysteinyldopa functionalities at each repeat unit, which provide catechol structures and

---

* see electronic supporting information for ref. [175]

promise high surface-binding capabilities. A quartz crystal microbalance with dissipation (QCM-D) was used to gain insights into the adsorption behavior as well as the coating stability of polyU$_1^C$ and polyU$_2^C$. Both mussel foot protein analogues show rapid adsorption from aqueous solutions onto QCM sensors, exposing either alumina or fluoropolymer surfaces (Figure 36; Supporting Information, Sections S5.13 and S5.14)[*]. Multilayer formation occurs and prevents to reach equilibrium, as it is typical for protein adsorption processes. Swelling of the polyU$_2^C$ coating on alumina is indicated by the gradual decrease in Δf during buffer rinsing (Supporting Information, Figure S30)[*]. Independent of the substrate, all of the coatings almost completely defy extensive rinsing with buffer and saline seawater equivalents (599 mM NaCl). Most impressively, the coatings withstand hypersaline conditions of 4.2M NaCl as present in water of the Dead Sea, showing negligible mass losses of 1–7%. Hence, the coating systems proved notable adhesion and robust cohesion stabilities. QCM data evaluation, applying the Voight model for viscoelastic films,[201] enables the estimation of areal mass densities of 40 ± 5 mg m^{-2} and
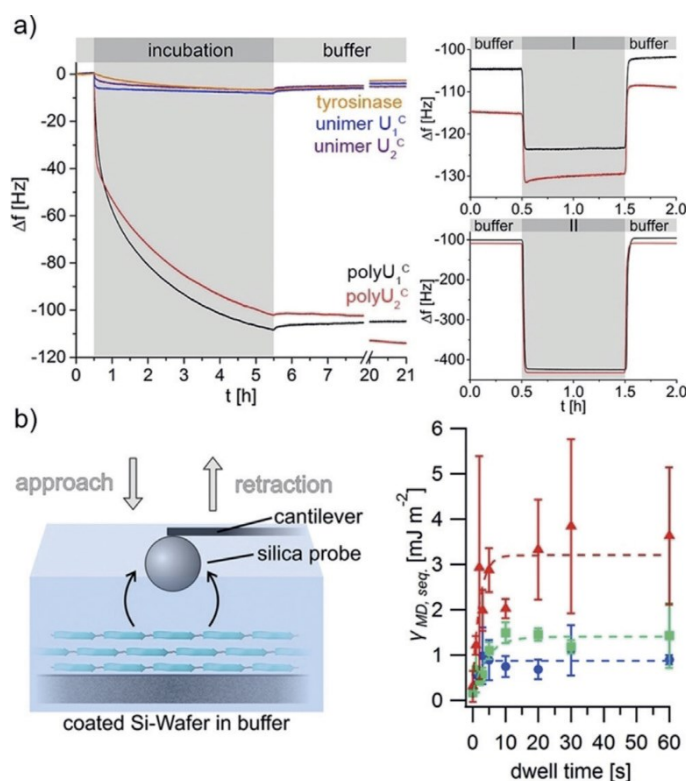
Figure 36   Adsorption (a) and adhesion (b) behavior of polyU$_1^C$ and polyU$_2^C$. a) QCM-D adsorption and desorption kinetics of mfp analogues on Al$_2$O$_3$ coated sensors (incubation step and subsequent buffer rinsing (left) and stability tests of the coatings (right) by washing with 599 mM NaCl (I) and 4.2 M hypersaline solution (II)). b) Adhesive properties of mfp analogue determined by colloidal probe AFM. Illustration of the CP-AFM contact analysis (left) and work of adhesion per unit area of polyU$_1^C$ coatings in dependence of the dwell time (right; substrates were coated for 1h (blue), for 2h (green) and 1h + post-treatment with sodium ascorbate (red); constant load force of 2 nN; lines are to guide the eye only). Reprinted with permission.[175] Copyright 2018 Wiley-VCH.

30 ± 4 mg m^{-2} with corresponding layer thicknesses of 34 ± 4 nm and 26 ± 2 nm for polyU$_1$^{C} and polyU$_2$^{C}, respectively. Using the Sauerbrey model[202] for rigid films to calculate adsorbed polymer masses leads to lower areal mass densities and thus suggests a certain viscoelasticity of the polymer films (Supporting Information, Table S4)*. This is supported by the fact that a pronounced frequency dependence in the *Δf* and *ΔD* response is visible for the coatings (Supporting Information, Figures S27, S35)*. By comparing the values of the different models it can be deduced that the polyU$_2$^{C} films give more rigid coatings, since the deviation between both models is lower than for polyU$_1$^{C} coatings. This can be rationalized by the different types of netpoints in the coatings: while polyU$_1$^{C} shows only non-covalent interchain contacts, the branched topology of polyU$_2$^{C} has instead covalent netpoints that increase network rigidity. This is consistent with covalently cross-linked Mefp-1 proteins that form more rigid coatings, that better suit the Sauerbrey regime.[203] A similar trend for coatings of polyU$_1$^{C} and polyU$_2$^{C} with respect to masses and thicknesses on alumina surfaces is evident for coatings on fluoropolymer substrates (Supporting Information, Figure S43)*. The latter are known to be highly challenging for coating, on which nonetheless marine mussels can effectively adhere well.[204] Estimated areal mass densities of 31 ± 3 mg m^{-2} and 18 ± 1 mg m^{-2} (Voight model) give theoretical layer thicknesses of 26 ± 2 nm and 15 ± 1 nm for polyU$_1$^{C} and polyU$_2$^{C}, respectively. The mass deposition kinetics onto fluoropolymer substrates are initially slightly faster than on alumina, but after 5 h of coating time, the final areal mass density is lower. This can be correlated to the priming step in the film formation process. Depending on the surface, the priming involves different contacts between peptide and substrate, which will have an influence on follow-up multilayer deposition. Ultimately, QCM-D experiments revealed that significantly different surfaces could be effectively coated, leading to stable coatings tolerant to harsh conditions. Both the cysteinyldopa connectivities and the repetitive mfp-1 consensus sequence were probably synergistically contributing to the properties, as the unimers and the enzyme alone led to negligible adsorption.

VII.2.3. Extension of the COS Theory for Multiple, Sequential Adhesive Failures

After confirming the exceptional coating behavior of the mussel foot protein analogues, the wet adhesive performance of polyU$_1$^{C} and polyU$_2$^{C} was investigated with colloidal probe atomic force microscopy (CP-AFM). From the theoretical background of CP-AFM and adhesion, as presented in chapter III.2, the Maugis model, and its

---

* see electronic supporting information for ref. [175]

approximation by COS, offers the most general description of contact between two bodies including the influence of adhesive forces. However, the model is linked to the assumption of isotropic, elastic, smooth bulk objects. Therefore, the detachment event is considered to happen at a particular contact area. Either at zero for DMT, at $\pi(3/2 \cdot \gamma \pi R^2 K^{-1})^{2/3}$ for JKR or in between but in a single event of instability. This is typically valid for "big" contact areas in the order of µm² or above. However, at lower contact areas and objects whose surfaces do not behave as bulk, multiple adhesive instabilities may occur.

We observed such multiple instabilities for our nanometer-thick mussel-inspired peptide coatings in contact with a micrometer-sized bead. One example force-deformation curve is shown in Figure 37 A with three distinct rupture events in the blue part of the curve. We attribute these sequential instabilities to the rather loss network structure of the purely adsorbed artificial peptide polymers on the silicon surface. The Maugis model, and all others presented in chapter III.2, assume a single adhesives detachment event to happen at the point of maximum adhesive interaction force, highlighted in the example curve of Figure 37 A with the central green square. Applying those models would neglect the measured adhesive interactions at higher separation, the region between the left and central square, and the work of adhesion would be underestimated.

To account for all the attractive, adhesive interactions, I proposed an extension of the COS theory, present in chapter III.2.5, which will be outlined in the following. First of all, to describe AFM measurement data with the unmodified COS theory the raw data does not provide the possibility to access the contact radius directly, as required for COS. One way to circumvent this limitation, however with a given uncertainty, is by a geometrical
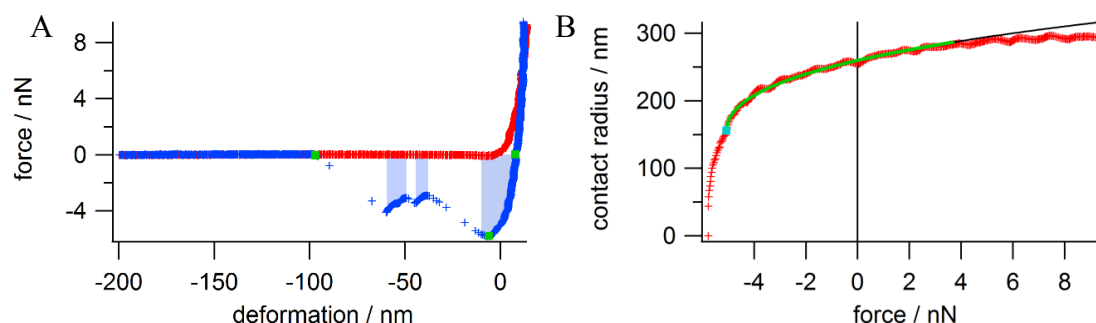
Figure 37 A) Force-deformation curve of 2.4µm radius silica sphere contacting a nm thick polypeptide layer adsorbed on a silicon wafer. Red curve refers to the approach, the blue curve to the retraction of both surfaces. Green squares mark adhesion relevant point, from right to left: point of zero external force while retracting, maximum adhesive force holding both surfaces together, jump out of contact. Blue shaded areas reflect the parts of the measurement at which both surfaces are in stable adhesive contact. B) Calculated contact radius vs force values (red) presenting the blue curve of figure A. This curve was fitted according to equation 54 in the range labeled green and an extension of the fit to higher values is shown in black. Preprinted with permission.[175] Copyright 2018 Wiley and open access under CC BY. Reprinted with permission.[175] Copyright 2018 Wiley-VCH.

approach. In case of sphere-plane contact the contact radius can be inferred from the probe radius R_{probe} and deformation δ by

$$a = \left(R_{probe}^2 - \left(R_{probe} - \delta\right)^2\right)^{0.5} \tag{53}$$

This recalculation, according to equation 53 is applied to all data points from the point of maximum adhesive force to higher, more positive deformations. Another point, which the original paper does not consider, is the general issue in AFM force measurements to determine the absolute zero in deformation, also discussed in chapter III.1. The theoretical lower limit is the DMT limit which results in equation 40 to $a(F=F_{adh})_{\alpha=0} = ((0+0)/1)^{2/3} a_0 = 0$. Allowing a variable transition parameter α gives a finite detachment contact radius of

$$a(F = F_{adh}) = \left(\frac{\alpha}{1+\alpha}\right)^{2/3}. \tag{54}$$

To account for this behavior, the recalculated contact radius is intentionally set to zero at the highest adhesion force. Applying both equations 53 and 54 gives the contact radius – force relationship depicted in Figure 37 B. The simplified assumption of zero contact radius at maximum negative force is compensated by extending the COS fitting equation 40 by equation 54 accounting for finite contact radius:

$$a = \left(\frac{\alpha + \sqrt{1 - F/F_{adh}}}{1+\alpha}\right)^{2/3} \cdot a_0 + \left(\frac{\alpha}{1+\alpha}\right)^{2/3} \cdot a_0 \tag{55}$$

Applying this fitting equation to measurement data allows for the analyses of adhesion and mechanics according to the COS equations presented in chapter III.2.5.

The proposed extension of the COS theory for multiple rip-off events is aiming to predict the work of adhesion per unit area values γ comparable to detachment processes with only one event, reflecting the total energy of separation. Therefore, the derived γ from the fitting equation 55 and equation 35 is considered in its essence as work performed normalized over a given area A_{norm}. Further, the work of adhesion without normalizing to an area can be directly extracted from the fit when retransformed to force-deformation values. The work w_{fit} equals the enclosed area of the fit with the x-axis for negative force values. With that, $A_{norm,fit}$ can be calculated by

$$A_{norm,fit} = \frac{w_{fit}}{\gamma_{MD}} \tag{56}$$

To stay as close as possible to the original concepts of Maugis and COS, we treat the multiple adhesive failures and its associated work of adhesion, all blue shaded areas in

Figure 37 A, as if it would be performed in an individual event over the same normalization area. I.e., all measured adhesive work is accumulated in the first rip-off event. This leads to the work of adhesion per unit area for sequential rip-off events $\gamma_{seq.\ rip}$

$$\gamma_{seq.rip} = \frac{W_{measur.rip\ offs}}{A_{norm,fit}}.$$ (57)

With this equation, a realistic value of work of adhesion per unit area is accessible, especially for systems showing a complex adhesive failure characteristic.

VII.2.4. Adhesive Interaction Energies Determined by CP-AFM

Introducing this new concept for extraction of adhesive interactions parameters from nm thin coatings by CP-AFM laid bases for the investigation of the mussel inspired polymers. PolyU$_1{}^C$ and polyU$_2{}^C$ were adsorbed onto passivated silicon wafers for 1 h and 2 h, respectively. Adhesive interactions of the coatings were quantified in force vs. distance measurements with a spherical silica probe of 2.4 µm radius. The probe was approached to the coated substrates, varying the maximum load (2–50 nN) and resting dwell times (0–60 s; Supporting Information, Figure S48)*. With increasing dwell times, the adhesion of the probe increases in a non-linear fashion for the entire sample set (Supporting Information, Figure S49; Figure 36 b)*. This correlates with a dynamic character of the interface in the contact area. Both coating polymers will rearrange during contact, thereby optimizing adhesive interactions with the probe. As the linear polyU$_1{}^C$ offers higher mobility, the work of adhesion at 60s dwell time reaches higher values of 1.4 mJ m^{-2}, compared to 0.5 mJ m^{-2} for the branched and less flexible polyU$_2{}^C$ (Figure 36 b (2 h); Supporting Information, Figure S49)*. The adhesion can be increased significantly to 3.6 mJ m^{-2} and 0.9 mJ m^{-2} at 60 s dwell time by applying sodium ascorbate antioxidant to the polymer coatings of polyU$_1{}^C$ and polyU$_2{}^C$. This suggests that oxidation of cysteinyldopa to quinone derivatives might occur during sample preparation and measurements, where the presence of antioxidants can regenerate the Dopa functionalities. The highest single value that was observed under such conditions reached 10.9 mJ m^{-2} for polyU$_1{}^C$ coatings at 30 s dwell time and 20 nN load. As expected, complex protein-based adhesives like the native mfps exhibit individual surface binding behavior and adaptation dynamics. For instance, silica adhesion of mfp-1, which is related to the synthetic polyU$_1{}^C$, showed only low work of adhesion of 0.1 mJ m^{-2} at pH 5.5.[205] It is remarkable that the artificial mfps provide considerably higher work of adhesion. Moreover, the specialized mfp-3 and mfp-5 that constitute the adhesion interface of mussels, reached maximum adhesive energy

values at pH 5.5 on silica of 2.99 and 2.44 mJ m^{-2} with a contact time of 60 min,[205] respectively, which are still below the average work of adhesion attained by polyU$_1^C$ after only 60 s of contact time. It also has to be noted that a complete loss of adhesive function was reported at pH 7–7.5[204] for several mfps, including mfp-1, whereas the artificial mfp analogues are able to perform at pH 6.8. Since there is only limited adhesion data for native mfps and absolute comparison is often difficult, CP-AFM reference experiments with a commercially available protein extract from *Mytilus edulis* (Cell-Tak) were performed. The control experiments were carried out under the same conditions as for polyU$_1^C$ (Supporting Information, Figure S50)*. CP-AFM revealed adhesion energies in a similar range, with an average of 3.9 mJ m^{-2} after 60 s dwell time and addition of ascorbate at 2 nN load force. Considering that Cell-Tak is an adhesive optimized for neutral pH, which consists of a mixture of mfps, wherein Mefp-1 is one component, and isolated Mefp-1 showed the lowest adhesion properties in previous studies,[206] the polyU$_1^C$ performs very well. The artificial mfp analogue seems to constitute a capable mfp-1 mimic by just relying on the consensus decapeptide of Mefp-1, but still leaves room for further improvements by sequence adaptation.

VII.3.   Conclusion

In conclusion, a novel tyrosinase-activated polymerization route to mussel foot protein (mfp) analogues was introduced. Polymerization of peptide-based unimers could be achieved using cysteinyldopa linking of an analogue of the Mefp-1 consensus decapeptide. Within a few minutes, polymers with an apparent molecular weight of up to 530 kDa are generated. The resulting artificial mfp analogues show versatile adsorption and result in coatings having excellent resistance to harsh hypersaline conditions, as demonstrated by QCM-D measurements. The adhesive energies in thin-film CP-AFM studies on silica surfaces are superior to values reported from surface apparatus studies on isolated mfp-1 as well as on isolated gluing interface proteins (mfp-3 and mfp-5). Moreover, similar adhesive energy ranges are achieved as with a commercial mussel foot protein extract from *Mytilus edulis*, which is optimized for adhesion at neutral pH. The tyrosinase induced polymerization of peptides offers facile access to artificial mfp analogues and avoids the complexity of naturally derived proteins. Next-generation universal glues can be envisioned that perform effectively even under rigorous seawater conditions and adapt to a broad range of challenging surfaces.

---

*see electronic supporting information for ref. [175]

VII.4. Notes on pH and surface chemistry dependence of the adhesives interactions

Beyond the results presented in chapter VII.2.4 for the adhesive interaction properties of the artificial mussel proteins at neutral pH, we performed further analysis on the effect of changing pH and adsorption to other surfaces than silicon. This chapter summarizes these experiments and results, which were not included in the initial publication but may be additionally published as addendum or research note.

Investigating the pH and surface chemistry dependence, we focused on the linear polyU$_1{}^C$, which was polymerized exactly like in the original work.[176] The artificial peptides were transferred to buffered solutions at pH 3.0, 5.5 and 8.0. Coatings were prepared on pre-cleaned silicon wafer by immersion for 1h followed by the addition of sodium ascorbate to the solution, as this proved to increase the work of adhesion per unit area for coatings at neutral pH 6.8. Further, the neutral peptide solution was absorbed to aluminum oxide and mica as two additional surface examples. Adhesion experiments were performed in AFM liquid cell with respective pure pH buffer using a silica colloidal probe (radius: 2.5 µm) fixed at the free end of a tip-less cantilever (spring constant: 0.10 N/m by thermal noise method). Contact was established with constant velocity of 2µm/s till a maximum load force of either 2, 5, 10, 20 or 50 nN was reached, held constant for 0, 1, 2, 3, 5, 10, 20, 30 or 60 seconds and then retracted. To improve statistical relevance every combination of load force and resting time was repeated 3 times in the same location and at 3 different locations. The retraction part of such force-deformation measurements was analyzed according to chapter VII.2.3.

The resulting work of adhesion per unit area accounting for sequential rip-off events, $\gamma_{MD,seq}$, is presented in Figure 38. For pH values of 6.8 or lower, the average $\gamma_{MD,seq}$ increases non-linear with dwell times from ~0.3 mJ m^{-2} at 0s up to ~2.5 mJ m^{-2} at 60s. In alkaline conditions, the adhesion is significantly reduced to an overall average of 0.63 mJ m^{-2} at low contacting forces and decreased to 0.32 mJ m^{-2} at high forces. This reduction of adhesion is in accordance with the observation for natural mfp-1[204]. However, the total vanishing of adhesive function could be avoided for polyU$_1{}^C$. In neutral to acid conditions, no clear pH-dependency can be deducted from the data within the measured variations. Still, the results suggest a tendency of reduced adhesion at pH 3 compared to pH 6.8 with only two of 45 average values breaking the trend. The maximum adhesion interactions
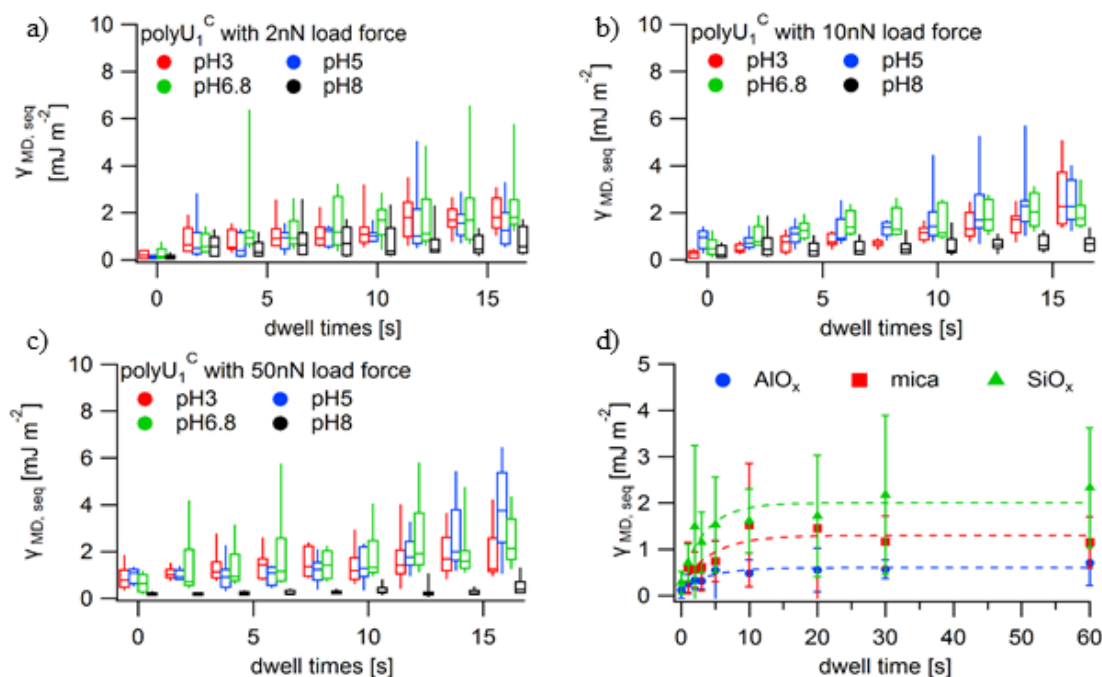
Figure 38 Statistical comparison of the pH and surface chemistry effect on the adhesion performance of polyU$_1^C$ coatings by CP-AFM. a) till c) show the correlation of work of adhesion per unit area with load force (2, 10 and 50 nN) at varying dwell in 4 buffered pH solutions. d) depicts the adhesion differences observed for three model surfaces, measured at pH 6.8.

found in single measurements were 5.1 mJ m^{-2} (pH3, 10 nN, 60s), 6.5 mJ m^{-2} (pH 5, 50 nN, 60s), 10.9 mJ m^{-2} (pH 6.8, 20 nN, 30s) and 5.3 mJ m^{-2} (pH 8, 5 nN, 5s).

To test the coating and adhesion effectivity of the artificial peptide, we further tested mica and aluminum oxid as additional model surfaces. Figure 38 d depicts the overall averaged work of adhesion per unit area values for the three test samples with a load force of 2 nN. In all cases, the adhesion gradually increases with dwell times up to 10 s after which a plateau-like behavior up to 60 s is apparent. Despite the scattering of the values, shown in Figure 38 d, with error bars representing the standard deviation, a trend may be abstracted. The adhesion plateau values observed increases from 0.6 mJ m^{-2} on aluminum oxide to 1.3 mJ m^{-2} on mica and 2.0 mJ m^{-2} on silicon oxide. A parallel to this behavior can be found in water contact angle of these surfaces. Note here that the contact angle can be influenced by various parameters, e.g., surface roughness and pre-treatment. Literature values for surfaces similarly treated as ours suggest a water contact angle on aluminum oxide in the range of 74 to 84° [207] and on mica in the range of 45 to 50°.[208] For the silicon wafer values between 10°, reported after RCA treatment, and 40°, reported after O$_2$ plasma treatment,[209] which both were done successively with our samples. One could speculate that higher hydrophilicity of the surface is beneficial for the deposition of the water-soluble

polyU$_1$^{C}, allowing for higher swelling of the coating and in turn more flexibility of adhering moieties to interact with the probe.

VII.5.   References

[50] H. Lee, B. P. Lee, P. B. Messersmith, *Nature* **2007**, *448*, 338.

[55] J. H. Waite, *Annals of the New York Academy of Science* **1999**, 875, 301.

[56] M. Yu, J. Hwang, T. J. Deming, *Journal of the American Chemical Society* **1999**, *121*, 5825.

[57] B. P. Lee, P. B. Messersmith, J. N. Israelachvili, J. H. Waite, *Annual Review of Materials Research* **2011**, *41*, 99.

[58] B. K. Ahn, S. Das, R. Linstadt, Y. Kaufman, N. R. Martinez-Rodriguez, R. Mirshafian, E. Kesselman, Y. Talmon, B. H. Lipshutz, J. N. Israelachvili, J. H. Waite, *Nature Communications* **2015**, *6*.

[175] J. Horsch, P. Wilke, M. Pretzler, M. Seuss, I. Melnyk, D. Remmler, A. Fery, A. Rompel, H. G. Börner, *Angewandte Chemie* **2018**, *130*, 15954.

[176] J. Horsch, P. Wilke, M. Pretzler, M. Seuss, I. Melnyk, D. Remmler, A. Fery, A. Rompel, H. G. Börner, *Angewandte Chemie International Edition* **2018**, *57*, 15728.

[177] P. Wilke, N. Helfricht, A. Mark, G. Papastavrou, D. Faivre, H. G. Börner, *Journal of the American Chemical Society* **2014**, *136*, 12667.

[178] Q. Wei, K. Achazi, H. Liebe, A. Schulz, P.-L. M. Noeske, I. Grunwald, R. Haag, *Angewandte Chemie International Edition* **2014**, *53*, 11650.

[179] H. Woehlk, J. Steinkoenig, C. Lang, L. Michalek, V. Trouillet, P. Krolla, A. S. Goldmann, L. Barner, J. P. Blinco, C. Barner-Kowollik, K. E. Fairfull-Smith, *Langmuir* **2018**, *34*, 3264.

[180] E. Faure, C. Falentin-Daudré, C. Jérôme, J. Lyskawa, D. Fournier, P. Woisel, C. Detrembleur, *Progress in Polymer Science* **2013**, *38*, 236.

[181] B. P. Lee, J. L. Dalsin, P. B. Messersmith, *Biomacromolecules* **2002**, *3*, 1038.

[182] P. Wilke, H. G. Börner, *ACS Macro Letters* **2012**, *1*, 871.

[183] A. Lampel, S. A. McPhee, H.-A. Park, G. G. Scott, S. Humagain, D. R. Hekstra, B. Yoo, P. W. Frederix, R. R. Abzalimov, S. G. Greenbaum, *Science* **2017**, *356*, 1064.

[184] D. S. Hwang, H. Zeng, Q. Lu, J. Israelachvili, J. H. Waite, *Soft Matter* **2012**, *8*, 5640.

[185] Q. Lu, D. S. Hwang, Y. Liu, H. Zeng, *Biomaterials* **2012**, *33*, 1903.

[186] Q. Lu, D. X. Oh, Y. Lee, Y. Jho, D. S. Hwang, H. Zeng, *Angewandte Chemie International Edition* **2013**, *52*, 3944.

[187] J. H. Waite, *Comparative Biochemistry and Physiology – Part B* **1990**, *97*, 19.

[188] M. J. Harrington, A. Masic, N. Holten-Andersen, J. H. Waite, P. Fratzl, *Science* **2010**, *328*, 216.

[189] L. M. McDowell, L. A. Burzio, J. H. Waite, J. Schaefer, *The Journal of Biological Chemistry* **1999**, *274*, 20293.

[190] L. V. Zuccarello, *Tissue Cell* **1981**, *13*, 701.

[191] T. Kato, S. Ito, K. Fujita, *Biochimica et Biophysica Acta* **1986**, *881*, 415.

[192] D. C. S. Tse, R. L. McCreery, R. N. Adams, *Journal of Medicinal Chemistry* **1976**, *19*, 37.

[193] H. Zhao, J. H. Waite, *Biochemistry* **2005**, *44*, 15915.

[194] H. Zhao, J. H. Waite, *The Journal of Biological Chemistry* **2006**, *281*, 26150.

[195] J. H. Waite, *The Journal of Biological Chemistry.* **1983**, *258*, 2911.

[196] M. Pretzler, A. Bijelic, A. Rompel, *Scientific Reports* **2017**, *7*, 1810.

[197] A. Flurkey, J. Cooksey, A. Reddy, K. Spoonmore, A. Rescigno, J. Inlow, W. H. Flurkey, *Journal of Agricultural and Food Chemistry* **2008**, *56*, 4760.

[198] S. G. Mauracher, C. Molitor, C. Michael, M. Kragl, A. Rizzi, A. Rompel, *Phytochemistry* **2014**, *99*, 14.

[199] T. S. Fischer, J. Steinkoenig, H. Woehlk, J. P. Blinco, K. Fairfull-Smith, C. Barner-Kowollik, *Polymer Chemistry* **2017**, *8*, 5269.

[200] S. C. Nicklisch, J. E. Spahn, H. Zhou, C. M. Gruian, J. H. Waite, *Biochemistry* **2016**, *55*, 2022.

[201] M. V. Voinova, M. Rodahl, M. Jonson, B. Kasemo, *Physica Scripta* **1999**, *59*, 391.

[202] G. Sauerbrey, *Zeitschrift für physik* **1959**, *155*, 206.

[203] F. Höök, B. Kasemo, T. Nylander, C. Fant, K. Sott, H. Elwing, *Analytical Chemistry* **2001**, *73*, 5796.

[204] Q. Lin, D. Gourdon, C. Sun, N. Holten-Andersen, T. H. Anderson, J. H. Waite, J. N. Israelachvili, *Proceedings oft he National Academy of Sciences of the USA* **2007**, *104*, 3782.

[205] Q. Lu, E. Danner, J. H. Waite, J. N. Israelachvili, H. Zeng, D. S. Hwang, *Journal of The Royal Society Interface* **2013**, *10*, 20120759.

[206] J. Yu, Y. Kan, M. Rapp, E. Danner, W. Wei, S. Das, D. R. Miller, Y. Chen, J. H. Waite, J. N. Israelachvili, *Proceedings oft he National Academy of Sciences of the USA* **2013**, *110*, 15680.

[207] W. Skoneczny, M. Niedźwiedź, M. Bara, *Applied Sciences* **2018**, *8*, 2251.

[208] P. B. Kowalczuk, C. Akkaya, M. Ergun, M. Janicki, O. Sahbaz, J. Drzymala, *Physicochemical Problems of Mineral Processing* **2017**, *53*.

[209] M. G. Kibria, F. Zhang, T. H. Lee, M. J. Kim, M. M. R. Howlader, *Nanotechnology* **2010**, *21*, 134011.

VIII. Further Contributions to Publications

After presenting the key publications of the thesis in chapters V to VII, I also contributed to further publications, in which my experience with AFM, optical light and laser microscopy and management of huge data packages were required. Here I want to give a short overview of these publications and my personal contribution to them in a chronological manner. I exclude the publication on microbubbles since there the results of my bachelor thesis were included.

The study on "*Two-in-One Composite Fibers With Side-by-Side Arrangement of Silk Fibroin and Poly(L-lactide) by Electrospinning*" had the device focused goal to produce composite micro-/nano-fibers of the textile industry-relevant silk fibroin while introducing a second natural polymer for increased tunability of material properties. For the fabrication, a specially developed side-by-side nozzle, separating both injection sources by a cooper foil, was used. The resulting composite fiber morphology and the internal polymer structures of the single components were characterized. Further, the mechanical properties were tested in tensile tests, and the influence of a fiber post-treatment was analyzed. My contribution to this study was to verify that each side of the fiber consists of one of the materials, confirming that they are causal for the structure. We labeled both polymer solutions with either Rhodamine B or Fluorescein sodium and found in CLSM micrographs a clear separation of both domains.

In cooperation with the chair of inorganic chemistry 1 of the University Bayreuth, I contributed to two publications entitled "*Controlled Exfoliation of Layered Silicate Heterostructures into Bilayers and Their Conversion into Giant Janus Platelets*"[210] and "*Systematic evaluation of different types of graphene oxide in respect to variations in their in-plane modulus*".[211] The first introduced a novel approach to fabricate giant inorganic plates with Janus like surface chemistry. Macroscopic layered silicates are first exfoliated into bilayer plates, their outer surfaces were modified with one polymer, the bilayers get cleaved apart in basic conditions and the new surfaces get decorated with another polymer. In the second study, a variety of graphene oxides prepared in various laboratories and following two different synthesis protocols were investigated with respect to the in-plane mechanical properties. These tests revealed that all graphene oxides have different mechanical properties which supports the argument that graphene oxides may not be thought of as a compound more as class of a
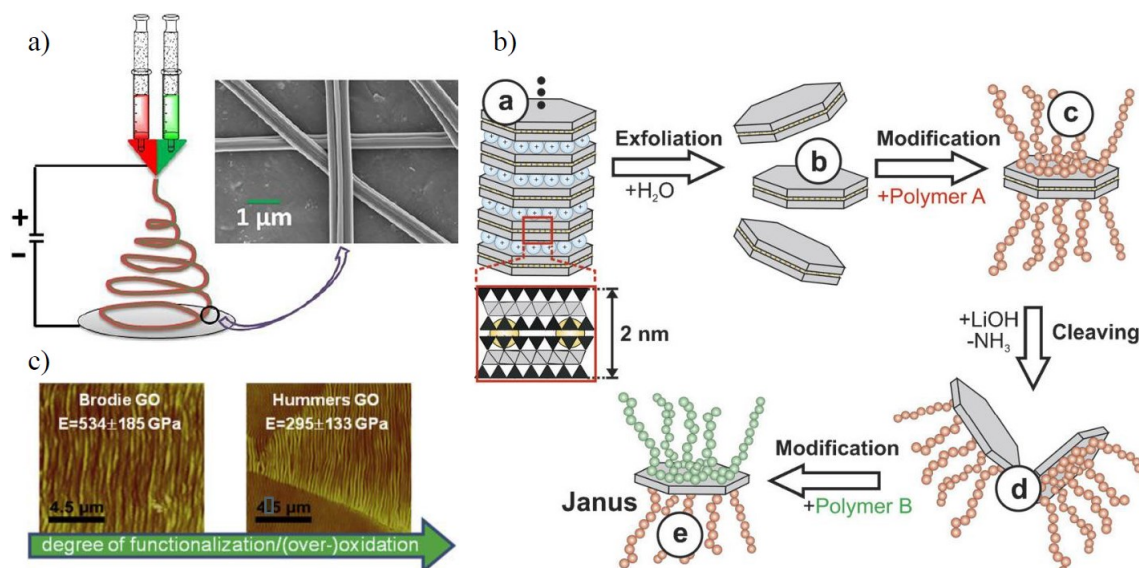
Figure 39   Selected figures from further publications. a) Scheme of the side-by-side electrospinning setup of two polymer solutions and SEM micrograph of the resulting fibers. Reprinted with permission.[212] Copyright 2015 Wiley-VCH Verlag. b) Preparation scheme for giant Janus platelets. Reprinted with permission.[210] Copyright 2016 Wiley-VCH Verlag. c) Two examples of the SIEBIMM AFM images of graphene oxide. Reprinted with permission.[211] Copyright 2017 Elsevier.

materials. In both studies, the mechanical properties of 2D – the thicknesses were in the range of a few nm compared to many µm in the lateral dimensions – inorganic materials were of interest. Here Jens Neubauer and I supported Patrick Feicht to establish the technique of *strain-induced elastic buckling instability for mechanical measurements* (SIEBIMM). I determine the elastic properties of the supporting PDMS layer by nano-indentation, and we both helped Patrick to solve depositioning problems of the samples on the substrate.

Further, we were invited to publish a trend article entitled "*Mechanically Defined Microgels by Droplet Microfluidics*".[25] The idea was to collect and present recent literature in the field with three main focuses: first to introduce the current state in droplet microfluidic chip design and experimental handling including concepts on how to manage emulsion stability of the uncrosslinked droplets by surfactants. The second chapter provides an overview of studies paying particular attention to mechanically well-defined microgels by controlling the polymer network structure using both synthetic and natural polymers, investigating how the gel morphology is affecting the mechanics and how such particles may be applied. In the last chapter analytical techniques are presented to measure their mechanical properties from classical macroscopic to microscopic approaches involving direct contact and some new
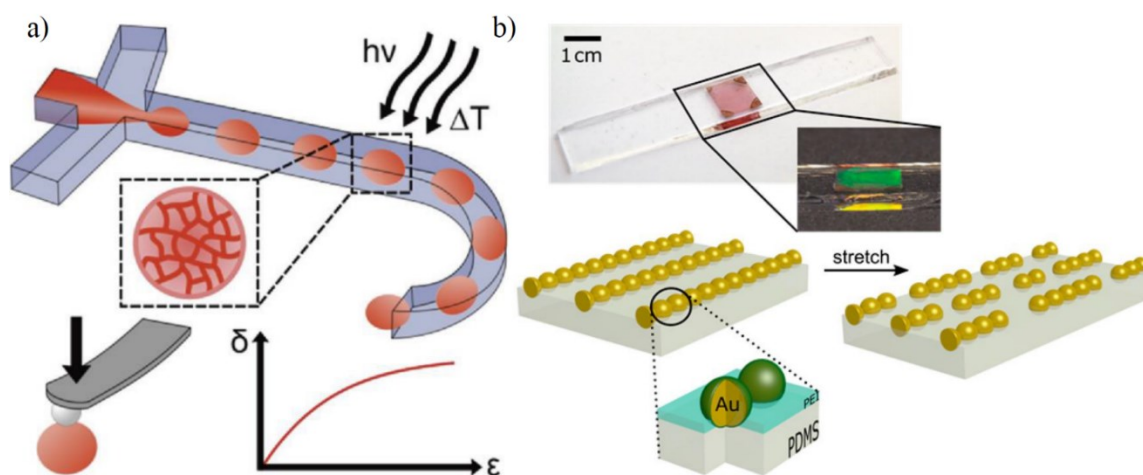
Figure 40 a) Illustration of a droplet microfluidic setup towards microgels indicating a mechanical CP-AFM test for verification of defined mechanical properties. Reprinted with permission.[25] Copyright 2016 Wiley-VCH Verlag. b) Photograph of an assembly of gold nanoparticle chains transferred onto an elastic substrate in the unstrained (top left) and strained (inset). Schemes illustrate the process of oligomer formation, highlighting the adhesion/cohesion situation on a pair of particles. Reprinted with permission.[213] Copyright 2017 American Chemical Society.

concepts based on flow deformation of microgel particles. This last chapter was my contribution to this review while especially Jens Neubauer and I spent a significant amount of time in editing the whole article.

In the last joint research project I co-authored the article "*Macroscopic Strain-Induced Transition from Quasi-infinite Gold Nanoparticle Chains to Defined Plasmonic Oligomers*".[213] Here, we introduced an approach to produce defined and oriented plasmonic oligomers constituted of spherical gold nanoparticles by breaking quasi-infinite – in the view of plasmonic coupling – particle chains by applying a macroscopic external strain. Therefore, gold nanoparticles with a very narrow size distribution were aligned in parallel lines by template-assisted self-assembly and transferred to plane, elastic PDMS substrate by wet contact printing. The transition from long chains to defined oligomers under external strain was followed by polarized UV-vis-NIR spectroscopy and *in-situ* AFM imaging. Both techniques revealed complementary results for the created oligomer sizes and statistical distribution. We established guidelines for this process based on the ratio of particle-substrate adhesion and particle-particle cohesion. They were verified by mechanical computer simulations and repeated experiments with varying adhesion-promoting layers on the elastic substrate. My contributions were the experimental design, execution, and data evaluation of the *in-situ* strain-dependent AFM images. Especially for the data evaluation, I created an algorithm and manually checked that every particle present in the image was identified correctly.

References

[25] T. Heida, J. W. Neubauer, M. Seuss, N. Hauck, J. Thiele, A. Fery, *Macromolecular Chemistry and Physics* **2017**, *218*, 1600418.

[210] M. Stöter, S. Gödrich, P. Feicht, S. Rosenfeldt, H. Thurn, J. W. Neubauer, M. Seuss, P. Lindner, H. Kalo, M. Möller, *Angewandte Chemie* **2016**, *128*, 7524.

[211] P. Feicht, R. Siegel, H. Thurn, J. W. Neubauer, M. Seuss, T. Szabó, A. V. Talyzin, C. E. Halbig, S. Eigler, D. A. Kunz, A. Fery, G. Papastavrou, J. Senker, J. Breu, *Carbon* **2017**, *114*, 700.

[212] L. Peng, S. Jiang, M. Seuß, A. Fery, G. Lang, T. Scheibel, S. Agarwal, *Macromolecular Materials and Engineering* **2016**, *301*, 48.

[213] A. M. Steiner, M. Mayer, M. Seuss, S. Nikolov, K. D. Harris, A. Alexeev, C. Kuttner, T. A. F. König, A. Fery, *ACS Nano* **2017**, *11*, 8871.

IX. Perspectives

The new concepts of inwards-interweaving self-assembly and the ingenious encapsulation of a responsive hydrogel added two tools to rationally design the contact mechanics and the adhesion of polymeric soft matter particles for application in aqueous environments. While both approaches still offer room to be further pushed to the limits or being adapted with other polymers, also new perspectives for this research area are imaginable. As mentioned in chapter II.2.1, the utilization of hydrogels in sensors is slowly advancing into industrial applications because for once of their rather long response times. Those could be reduced by exchanging the bigger macroscopic gels with the herein presented microgel particles since the underlying diffusion-limited swelling or deswelling should be much faster. However, the accompanying need for precise handling of single microgel particles and the size reduction of sensors is not realistic on a proof of concept lab level so far. One way to combine the best of both worlds cloud be the incorporation of microfluidically prepared, responsive microgel particles in a macroscopic hydrogel matrix. Such an approach was already followed by Nguyen et. al[214] covalently introducing nanogel particles in a poly(ethylene glycol) diglycidyl ether matrix, thereby enhancing its mechanical properties and stretchability. Further, could this microgel-macrogel blend strategy improve the response time following the ideas of Ida et. al.[215] They studied the effect of monomer sequence for thermoresponsive hydrogels constitute out of two different monomers, produced either by classical copolymerization or by cocrosslinking of a mixture of the involved polymers. Thereby, they observed a decrease in response time of one order of magnitude for the cocrosslinked compared to the copolymerized one. They accredited this to the possibility of drains forming within the crosslinked hydrogel, enhancing the diffusion of solvent molecules out of the gel. With that a synergy of responsive microparticles cocrosslinked into a rather soft macrogel matrix, which may also include the idea of interpenetration of the matrix within the particles as introduced in chapter VI, could result in a new generation of fast and reliable hydrogel sensors.

References

[214] N. T. Nguyen, A. H. Milani, J. Jennings, D. J. Adlam, A. J. Freemont, J. A. Hoyland, B. R. Saunders, *Nanoscale* **2019**, *11*, 7921.
[215] S. Ida, T. Kawahara, H. Kawabata, T. Ishikawa, Y. Hirokawa, *Gels* **2018**, *4*, 22.

Danksagung

Nach der Pflicht folgt bekanntlich die Kür. Da ich keine 10 Punkte in der A-Note erwarte, kann ich hoffentlich in der B-Note glänzen. Mit der Abgabe dieser Doktorarbeit geht ein großes Kapitel von ziemlich genau 11 Jahren Studium zu Ende und dementsprechend gilt es sich bei vielen Personen zu bedanken.

Andreas, dir möchte ich an erste Stelle dafür danken, dass du mich ein großes Stück des Weges begleitet, angeleitet, angespornt, gefördert und gefordert hast. Mit all den Freiräumen, die du mir gewährt hast, all den guten Ideen, die unsere Zusammenarbeit so erfolgreich gestaltet hat, und all den wertvollen Erfahrungen, die wir in Bayreuth und Dresden sammeln konnten.

Über langjährige Weggefährten sprechend, möchte ich mich auch bei allen meinen Kommilitonen/innen bedanken, die mich fortwährend unterstützt haben und das gesamte Studium unvergesslich gemacht haben! Ein besonderes Dankeschön geht an meine drei J-Buddies - Jens, Jessy und Johannes-, die PC I `ler Astrid, Christian, Christina, Fabi und Pia und natürlich auch Dominik, Thomas und Tobi für die vielen Stunden des gemeinsamen Lernens, aber auch die „Mußestunden".

Daran anschließend, möchte ich mich aller herzlichst bei der großen PC II Familie aus Bayreuth und deren Mitumsiedlern nach Dresden bedanken! Dafür, dass ihr immer mit Rat, Tat, Hilfe aber auch Zerstreuung mir zur Seite gestanden seid. Hier möchte ich namentlich nur meine Mentoren aus der Anfangszeit – Daniel, Johann, Martin und Melanie – und natürlich „Mama" Sybille nennen. All den anderen danke ich natürlich auch aus tiefstem Herzen; ihr seid nur einfach zu viele für diesen kurzen Abschnitt…

Nicht vergessen möchte ich hier all die tollen Leute, die ich in Dresden kennenlernen durfte. Die Kollegen und Mitarbeiter am IPF, meinen beiden Bürokollegen – Ivan und Ugo – und dem gesamt GRK-1865 Team.

Abschließend, gilt ein großes, dickes DANKE meiner gesamten Familie für ihre fortwährende Unterstützung, Rückhalt, Motivation und dafür, dass sie immer an mich geglaubt haben!

Ciao, servus, pfiat eich und auf bald!

Table of References

[1] P.-G. de Gennes, *Science et Vie Junior* **2007**, 13.

[2] S. R. Nagel, *Reviews of Modern Physics* **2017**, *89*, 025002.

[3] J. van der Gucht, *Frontiers in Physics* **2018**, *6*.

[4] M. de Jong, W. Chen, T. Angsten, A. Jain, R. Notestine, A. Gamst, M. Sluiter, C. Krishna Ande, S. van der Zwaag, J. J. Plata, C. Toher, S. Curtarolo, G. Ceder, K. A. Persson, M. Asta, *Scientific Data* **2015**, *2*, 150009.

[5] M. J. Majcher, T. Hoare, *Functional Biopolymers* **2018**, 1.

[6] O. Wichterle, D. Lím, *Nature* **1960**, *185*, 117.

[7] S. J. Buwalda, K. W. M. Boere, P. J. Dijkstra, J. Feijen, T. Vermonden, W. E. Hennink, *Journal of Controlled Release* **2014**, *190*, 254.

[8] M. Karg, A. Pich, T. Hellweg, T. Hoare, L. A. Lyon, J. J. Crassous, D. Suzuki, R. A. Gumerov, S. Schneider, I. I. Potemkin, W. Richtering, *Langmuir* **2019**, *35*, 6231.

[9] J. V. Alemán, A. V. Chadwick, J. He, M. Hess, K. Horie, R. G. Jones, P. Kratochvíl, I. Meisel, I. Mita, G. Moad, S. Penczek, R. F. T. Stepto, "Definitions of terms relating to the structure and processing of sols, gels, networks, and inorganic-organic hybrid materials (IUPAC Recommendations 2007)", in *Pure and Applied Chemistry*, 2007, p. 79/1801.

[10] H. Elias, "Makromoleküle–Chemische Strukturen und Synthesen", 6. edition, Wiley-VCH Verlag, Weinheim, Weinheim, 2001346.

[11] M. D. Lechner, K. Gehrke, E. H. Nordmeier, U. Guhr, "*Makromolekulare Chemie*", 5. edition, Springer, 2003.

[12] O. Virtanen, M. Brugnoni, M. Kather, A. Pich, W. Richtering, *Polymer Chemistry* **2016**, *7*, 5123.

[13] R. H. Pelton, P. Chibante, *Colloids and Surfaces* **1986**, *20*, 247.

[14] M. Kather, F. Ritter, A. Pich, *Chemical Engineering Journal* **2018**, *344*, 375.

[15] R. Tiwari, A. Walther, *Polymer Chemistry* **2015**, *6*, 5550.

[16] A. Melle, A. Balaceanu, M. Kather, Y. Wu, E. Gau, W. Sun, X. Huang, X. Shi, M. Karperien, A. Pich, *Journal of Materials Chemistry B* **2016**, *4*, 5127.

[17] A. C. Brown, S. E. Stabenfeldt, B. Ahn, R. T. Hannan, K. S. Dhada, E. S. Herman, V. Stefanelli, N. Guzzetta, A. Alexeev, W. A. Lam, L. A. Lyon, T. H. Barker, *Nature Materials* **2014**, *13*, 1108.

[18] Q. Zhang, L. Zha, J. Ma, B. Liang, *Journal of Colloid and Interface Science* **2009**, *330*, 330.

[19] L. Shang, Y. Cheng, Y. Zhao, *Chemical Reviews* **2017**, *117*, 7964.

[20] R. Seemann, M. Brinkmann, T. Pfohl, S. Herminghaus, *Reports on progress in physics* **2011**, 75, 016601.

[21] J. Zhang, S. Yan, D. Yuan, G. Alici, N.-T. Nguyen, M. Ebrahimi Warkiani, W. Li, *Lab on a Chip* **2016**, *16*, 10.

[22] S. C. Hur, T. Z. Brinckerhoff, C. M. Walthers, J. C. Y. Dunn, D. Di Carlo, *PLOS ONE* **2012**, *7*, e46550.

[23] S. With, M. Trebbin, C. B. A. Bartz, C. Neuber, M. Dulle, S. Yu, S. V. Roth, H.-W. Schmidt, S. Förster, *Langmuir* **2014**, *30*, 12494.

[24] O. Otto, P. Rosendahl, A. Mietke, S. Golfier, C. Herold, D. Klaue, S. Girardo, S. Pagliara, A. Ekpenyong, A. Jacobi, *Nature methods* **2015**, *12*, 199.

[25] T. Heida, J. W. Neubauer, M. Seuss, N. Hauck, J. Thiele, A. Fery, *Macromolecular Chemistry and Physics* **2017**, *218*, 1600418.

[26] A. S. Utada, A. Fernandez-Nieves, H. A. Stone, D. A. Weitz, *Physical Review Letters* **2007**, *99*, 094502.

[27] P. Guillot, A. Colin, *Physical Review E* **2005**, *72*, 066301.

[28] S. L. Anna, H. C. Mayer, *Physics of Fluids* **2006**, *18*, 121512.

[29] G. F. Christopher, S. L. Anna, *Journal of Physics D: Applied Physics* **2007**, *40*, R319.

[30] M. De Menech, P. Garstecki, F. Jousse, H. A. Stone, *Journal of Fluid Mechanics* **2008**, *595*, 141.

[31] S.-Y. Teh, R. Lin, L.-H. Hung, A. P. Lee, *Lab on a Chip* **2008**, *8*, 198.

[32] S. Hardt, K. Drese, V. Hessel, F. Schönfeld, "Passive micro mixers for applications in the micro reactor and µTAS field", in *ASME 2004 2nd International Conference on Microchannels and Minichannels*, American Society of Mechanical Engineers, 200445.

[33] H. Song, J. D. Tice, R. F. Ismagilov, *Angewandte Chemie International Edition* **2003**, *42*, 768.

[34] G. Gerlach, M. Guenther, G. Suchaneck, J. Sorber, K. F. Arndt, A. Richter, *Macromolecular Symposia* **2004**, *210*, 403.

[35] G. Gerlach, M. Guenther, J. Sorber, G. Suchaneck, K.-F. Arndt, A. Richter, *Sensors and Actuators B: Chemical* **2005**, *111*, 555.

[36] J. Erfkamp, M. Guenther, G. Gerlach, *Journal of Sensors and Sensor Systems* **2018**, *7*, 219.

[37] K. Deng, C. Bellmann, Y. Fu, M. Rohn, M. Guenther, G. Gerlach, *Sensors and Actuators B: Chemical* **2018**, *255*, 3495.

[38] X. Jia, T. Zhang, J. Wang, K. Wang, H. Tan, Y. Hu, L. Zhang, J. Zhu, *Langmuir* **2018**, *34*, 3987.

[39] S. Jia, Z. Tang, Y. Guan, Y. Zhang, *ACS Applied Materials & Interfaces* **2018**, *10*, 14254.

[40] L. Ionov, *Materials Today* **2014**, *17*, 494.

[41] P. Frank, D. Gräfe, C. Probst, S. Haefner, M. Elstner, D. Appelhans, D. Kohlheyer, B. Voit, A. Richter, *Advanced Functional Materials* **2017**, *27*, 1700430.

[42] S. Maeda, Y. Hara, T. Sakai, R. Yoshida, S. Hashimoto, *Advanced Materials* **2007**, *19*, 3480.

[43] R. M. Erb, J. S. Sander, R. Grisch, A. R. Studart, *Nature Communications* **2013**, *4*, 1712.

[44] E. Palleau, D. Morales, M. D. Dickey, O. D. Velev, *Nature Communications* **2013**, *4*, 2257.

[45] F. Schneider, *Angewandte Chemie* **1986**, *98*, 941.

[46] A. N. Zaikin, A. M. Zhabotinsky, *Nature* **1970**, *225*, 535.

[47] K. Ito, S. Sakuma, Y. Yokoyama, F. Arai, *ROBOMECH Journal* **2014**, *1*, 5.

[48] K. F. Arndt, D. Kuckling, A. Richter, *Polymers for Advanced Technologies* **2000**, *11*, 496.

[49] G. Isapour, M. Lattuada, *Advanced Materials* **2018**, *30*, 1707069.

[50] H. Lee, B. P. Lee, P. B. Messersmith, *Nature* **2007**, *448*, 338.

[51] Q. Zhao, D. W. Lee, B. K. Ahn, S. Seo, Y. Kaufman, J. N. Israelachvili, J. H. Waite, *Nature Materials* **2016**, *15*, 407.

[52] F. Fu, L. Shang, Z. Chen, Y. Yu, Y. Zhao, *Science Robotics* **2018**, *3*.

[53] L. F. Boesel, C. Greiner, E. Arzt, A. del Campo, *Advanced Materials* **2010**, *22*, 2125.

[54] G. Huber, H. Mantz, R. Spolenak, K. Mecke, K. Jacobs, S. N. Gorb, E. Arzt, *Proceedings of the National Academy of Sciences of the United States of America* **2005**, *102*, 16293.

[55] J. H. Waite, *Annals of the New York Academy of Science* **1999**, 875, 301.

[56] M. Yu, J. Hwang, T. J. Deming, *Journal of the American Chemical Society.* **1999**, *121*, 5825.

[57] B. P. Lee, P. B. Messersmith, J. N. Israelachvili, J. H. Waite, *Annual Review of Materials Research* **2011**, *41*, 99.

[58] B. K. Ahn, S. Das, R. Linstadt, Y. Kaufman, N. R. Martinez-Rodriguez, R. Mirshafian, E. Kesselman, Y. Talmon, B. H. Lipshutz, J. N. Israelachvili, J. H. Waite, *Nature Communications* **2015**, *6*.

[59] H. Zhao, C. Sun, R. J. Stewart, J. H. Waite, *Journal of Biological Chemistry* **2005**, *280*, 42938.

[60] C. S. Wang, R. J. Stewart, *Biomacromolecules* **2013**, *14*, 1607.

[61] C. S. Wang, R. J. Stewart, *The Journal of Experimental Biology* **2012**, *215*, 351.

[62] E. Spruijt, "*Strength, structure and stability of polyelectrolyte complex coacervates*", PhD thesis, Wageningen University, The Netherlands, 2012.

[63] J.-F. Gauvin, *Renaissance Quarterly* **2012**, *65*, 564.

[64] A. Bogner, P.-H. Jouneau, G. Thollet, D. Basset, C. Gauthier, *Micron* **2007**, *38*, 390.

[65] D. B. Williams, C. B. Carter, "The transmission electron microscope", in *Transmission electron microscopy*, Springer, 1996, p. 3.

[66] N. Tanaka, *Science and technology of advanced materials* **2008**, 9, 014111.

[67] G. Binnig, H. Rohrer, C. Gerber, E. Weibel, *Physical review letters* **1982**, *49*, 57.

[68] G. Binnig, C. F. Quate, C. Gerber, *Physical Review Letters* **1986**, *56*, 930.

[69] N. Jalili, K. Laxminarayana, *Mechatronics* **2004**, *14*, 907.

[70] C. P. Green, H. Lioe, J. P. Cleveland, R. Proksch, P. Mulvaney, J. E. Sader, *Review of Scientific Instruments* **2004**, *75*, 1988.

[71] H.-J. Butt, B. Cappella, M. Kappl, *Surface Science Reports* **2005**, *59*, 1.

[72] H. Hertz, *Journal für die reine und angewandte Mathematik* **1882**, 1882, 156.

[73] H. Hertz, D. E. Jones, G. A. Schott, "*Miscellaneous papers*", Macmillan and Company, 1896.

[74] G. R. Kirchhoff, "Vorlesungen über mathematische physik: mechanik", Teubner, 1876.

[75] A. D. Roberts, "Ph.D. disseration", Cambridge University, England, 1968.

[76] K. Kendall, "The stiffness of surfaces in static and sliding contact", University of Cambridge, 1969.

[77] K. L. Johnson, K. Kendall, A. D. Roberts, *Proceedings of the Royal Society of London Series a-Mathematical and Physical Sciences* **1971**, 324, 301.

[78] B. V. Derjaguin, V. M. Muller, Y. P. Toporov, *Journal of Colloid and Interface Science* **1975**, *53*, 314.

[79] J. A. Greenwood, *Tribology Letters* **2007**, *26*, 203.

[80] V. M. Muller, B. V. Derjaguin, Y. P. Toporov, *Colloids and Surfaces* **1983**, *7*, 251.

[81] B. Derjaguin, *Kolloid-Zeitschrift* **1934**, *69*, 155.

[82] E. Barthel, *Journal of Physics D: Applied Physics* **2008**, 41, 163001.

[83] D. Maugis, *Journal of Colloid and Interface Science* **1992**, 150, 243.

[84] R. W. Carpick, D. F. Ogletree, M. Salmeron, *Journal of Colloid and Interface Science* **1999**, *211*, 395.

[85] M. Glaubitz, N. Medvedev, D. Pussak, L. Hartmann, S. Schmidt, C. A. Helm, M. Delcea, *Soft Matter* **2014**, *10*, 6732.

[86] H. M. Pan, M. Seuss, M. P. Neubauer, D. W. Trau, A. Fery, *ACS Applied Materials & Interfaces* **2016**, *8*, 1493.

[87] M. Seuss, W. Schmolke, A. Drechsler, A. Fery, S. Seiffert, *ACS Applied Materials & Interfaces* **2016**, *8*, 16317.

[88] A. Noda, M. Yamaguchi, M. Aizawa, Y. Kumano, "Cosmetic containing fine soft microcapsules", Google Patents, 1992.

[89] S. Wiese, A. C. Spiess, W. Richtering, *Angewandte Chemie* **2013**, *125*, 604.

[90] R. P. John, R. Tyagi, S. Brar, R. Surampalli, D. Prévost, *Critical reviews in biotechnology* **2011**, *31*, 211.

[91] H. M. Shewan, J. R. Stokes, *Journal of Food Engineering* **2013**, *119*, 781.

[92] W. C. Mak, K. Y. Cheung, D. Trau, *Chemistry of Materials* **2008**, *20*, 5475.

[93] H. Senff, W. Richtering, *Colloid and Polymer Science* **2000**, *278*, 830.

[94] J. Meid, F. Dierkes, J. Cui, R. Messing, A. J. Crosby, A. Schmidt, W. Richtering, *Soft Matter* **2012**, *8*, 4254.

[95] T. R. Hoare, D. S. Kohane, *Polymer* **2008**, *49*, 1993.

[96] M. Delcea, S. Schmidt, R. Palankar, P. A. L. Fernandes, A. Fery, H. Moehwald, A. G. Skirtach, *Small* **2010**, *6*, 2858.

[97] A. G. Skirtach, A. Munoz Javier, O. Kreft, K. Köhler, A. Piera Alberola, H. Möhwald, W. J. Parak, G. B. Sukhorukov, *Angewandte Chemie International Edition* **2006**, *45*, 4612.

[98] B. G. De Geest, S. De Koker, G. B. Sukhorukov, O. Kreft, W. J. Parak, A. G. Skirtach, J. Demeester, S. C. De Smedt, W. E. Hennink, *Soft Matter* **2009**, *5*, 282.

[99] B. V. Parakhonskiy, A. M. Yashchenok, M. Konrad, A. G. Skirtach, *Advances in colloid and interface science* **2014**, *207*, 253.

[100] R. Hartmann, M. Weidenbach, M. Neubauer, A. Fery, W. J. Parak, *Angewandte Chemie International Edition* **2015**, *54*, 1365.

[101] X. Banquy, F. Suarez, A. Argaw, J.-M. Rabanel, P. Grutter, J.-F. Bouchard, P. Hildgen, S. Giasson, *Soft Matter* **2009**, *5*, 3984.

[102] W. Liu, X. Zhou, Z. Mao, D. Yu, B. Wang, C. Gao, *Soft Matter* **2012**, *8*, 9235.

[103] X. Yi, X. Shi, H. Gao, *Physical review letters* **2011**, *107*, 098101.

[104] J. Bai, S. Beyer, W. C. Mak, R. Rajagopalan, D. Trau, *Angewandte Chemie International Edition* **2010**, *49*, 5189.

[105] H. M. Pan, S. Beyer, Q. Zhu, D. Trau, *Advanced Functional Materials* **2013**, *23*, 5108.

[106] G. Decher, *science* **1997**, *277*, 1232.

[107] K. Sato, T. Nakajima, J.-i. Anzai, *Journal of colloid and interface science* **2012**, *387*, 123.

[108] K. Landfester, A. Musyanovych, V. Mailänder, *Journal of Polymer Science Part A: Polymer Chemistry* **2010**, *48*, 493.

[109] J. Bai, S. Beyer, T. S. Yein, D. Trau, *ACS applied materials & interfaces* **2011**, *3*, 1665.

[110] J. Bai, S. Beyer, W. C. Mak, D. Trau, *Soft Matter* **2009**, *5*, 4152.

[111] H. M. Pan, A. Subramanian, C. J. Ochs, J.-Y. Dewavrin, S. Beyer, D. W. Trau, *RSC Advances* **2014**, *4*, 35163.

[112] W. C. Mak, J. Bai, X. Y. Chang, D. Trau, *Langmuir* **2008**, *25*, 769.

[113] W. A. Ducker, T. J. Senden, R. M. Pashley, *Nature* **1991**, *353*, 239.

[114] E. K. Dimitriadis, F. Horkay, J. Maresca, B. Kachar, R. S. Chadwick, *Biophysical journal* **2002**, *82*, 2798.

[115] A. Fery, F. Dubreuil, H. Möhwald, *New Journal of Physics* **2004**, *6*, 18.

[116] J. Domke, M. Radmacher, *Langmuir* **1998**, *14*, 3320.

[117] C. Ye, I. Drachuk, R. Calabrese, H. Dai, D. L. Kaplan, V. V. Tsukruk, *Langmuir* **2012**, *28*, 12235.

[118] M. Pretzl, M. Neubauer, M. Tekaat, C. Kunert, C. Kuttner, G. r. Leon, D. Berthier, P. Erni, L. Ouali, A. Fery, *ACS applied materials & interfaces* **2012**, *4*, 2940.

[119] M. P. Neubauer, C. Blüm, E. Agostini, J. Engert, T. Scheibel, A. Fery, *Biomaterials Science* **2013**, *1*, 1160.

[120] S. Schmidt, M. Zeiser, T. Hellweg, C. Duschl, A. Fery, H. Moehwald, *Advanced Functional Materials* **2010**, *20*, 3235.

[121] B. Cappella, J. R. Wassenberg, L.-O. Heim, M. Klostermann, J. Venzmer, E. Bonaccurso, *Polymer* **2014**, *55*, 1209.

[122] J. P. Best, S. Javed, J. J. Richardson, K. L. Cho, M. M. Kamphuis, F. Caruso, *Soft Matter* **2013**, *9*, 4580.

[123] E. Glynos, V. Sboros, V. Koutsos, *Materials Science and Engineering: B* **2009**, *165*, 231.

[124] A. Fery, R. Weinkamer, *Polymer* **2007**, *48*, 7221.

[125] J. L. Hutter, J. Bechhoefer, *Review of Scientific Instruments* **1993**, *64*, 1868.

[126] S. Beyer, J. Bai, A. M. Blocki, C. Kantak, Q. Xue, M. Raghunath, D. Trau, *Soft Matter* **2012**, *8*, 2760.

[127] F. Dubreuil, N. Elsner, A. Fery, *The European Physical Journal E* **2003**, *12*, 215.

[128] C. Gao, E. Donath, S. Moya, V. Dudnik, H. Möhwald, *The European Physical Journal E* **2001**, *5*, 21.

[129] A. Muñoz Javier, O. Kreft, A. Piera Alberola, C. Kirchner, B. Zebli, A. S. Susha, E. Horn, S. Kempter, A. G. Skirtach, A. L. Rogach, *Small* **2006**, *2*, 394.

[130] H. G. Schild, *Progress in Polymer Science* **1992**, *17*, 163.

[131] Y. Okada, F. Tanaka, *Macromolecules* **2005**, *38*, 4465.

[132] Y. H. Bae, T. Okano, S. W. Kim, *Journal of Polymer Science Part B-Polymer Physics* **1990**, *28*, 923.

[133] C. Erbil, Y. Yildiz, N. Uyanik, *Polymer International* **2000**, *49*, 795.

[134] K. Dušek, Patterso.D, *Journal of Polymer Science Part a-2-Polymer Physics* **1968**, *6*, 1209.

[135] Y. Li, T. Tanaka, *Journal of Chemical Physics* **1989**, *90*, 5161.

[136] Y. Li, T. Tanaka, *Annual Review of Materials Science* **1992**, *22*, 243.

[137] S. Hirotsu, *Phase Transitions* **1994**, *47*, 183.

[138] J. Zhang, R. Pelton, Y. L. Deng, *Langmuir* **1995**, *11*, 2301.

[139] H. Kanazawa, K. Yamamoto, Y. Matsushima, N. Takai, A. Kikuchi, Y. Sakurai, T. Okano, *Analytical Chemistry* **1996**, *68*, 100.

[140] Y. Hirose, T. Amiya, Y. Hirokawa, T. Tanaka, *Macromolecules* **1987**, *20*, 1342.

[141] C. Wu, S. Q. Zhou, *Macromolecules* **1997**, *30*, 574.

[142] A. Fernandez-Barbero, A. Fernandez-Nieves, I. Grillo, E. Lopez-Cabarcos, *Physical Review E* **2002**, *66*, 051803.

[143] H. Senff, W. Richtering, *Journal of Chemical Physics* **1999**, *111*, 1705.

[144] J. Z. Wu, B. Zhou, Z. B. Hu, *Physical Review Letters* **2003**, *90*, 1.

[145] M. Stieger, J. S. Pedersen, P. Lindner, W. Richtering, *Langmuir* **2004**, *20*, 7283.

[146] G. Romeo, A. Fernandez-Nieves, H. M. Wyss, D. Acierno, D. A. Weitz, *Advanced Materials* **2010**, *22*, 3441.

[147] S. Hirotsu, *Macromolecules* **1990**, *23*, 903.

[148] S. M. Hashmi, E. R. Dufresne, *Soft Matter* **2009**, *5*, 3682.

[149] A. Burmistrova, M. Richter, M. Eisele, C. Uezuem, R. von Klitzing, *Polymers* **2011**, *3*, 1575.

[150] A. J. Engler, S. Sen, H. L. Sweeney, D. E. Discher, *Cell* **2006**, *126*, 677.

[151] E. C. Cho, J.-W. Kim, A. Fernandez-Nieves, D. A. Weitz, *Nano Letters* **2008**, *8*, 168.

[152] C. D. Jones, L. A. Lyon, *Langmuir* **2003**, *19*, 4544.

[153] C. D. Jones, L. A. Lyon, *Macromolecules* **2003**, *36*, 1988.

[154] X. Li, J. Zuo, Y. Guo, X. Yuan, *Macromolecules* **2004**, *37*, 10042.

[155] I. Berndt, J. S. Pedersen, P. Lindner, W. Richtering, *Langmuir* **2006**, *22*, 459.

[156] M. Zeiser, I. Freudensprung, T. Hellweg, *Polymer* **2012**, *53*, 6096.

[157] S. M. Lee, Y. C. Bae, *Macromolecules* **2014**, *47*, 8394.

[158] H. Zhao, H. Chen, Z. Li, W. Su, Q. Zhang, *European Polymer Journal* **2006**, *42*, 2192.

[159] J. Gernandt, G. Frenning, W. Richtering, P. Hansson, *Soft Matter* **2011**, *7*, 10327.

[160] S. Seiffert, J. Thiele, A. R. Abate, D. A. Weitz, *Journal of the American Chemical Society* **2010**, *132*, 6606.

[161] J. C. McDonald, D. C. Duffy, J. R. Anderson, D. T. Chiu, H. K. Wu, O. J. A. Schueller, G. M. Whitesides, *Electrophoresis* **2000**, *21*, 27.

[162] K. P. Kronfeld, H. J. Timpe, *Journal Fur Praktische Chemie* **1988**, *330*, 571.

[163] S. Seiffert, W. Oppermann, K. Saalwaechter, *Polymer* **2007**, *48*, 5599.

[164] L. Ling, W. D. Habicher, D. Kuckling, H. J. Adler, *Designed Monomers and Polymers* **1999**, *2*, 351.

[165] C. D. Vo, D. Kuckling, H. J. P. Adler, M. Schohoff, *Colloid and Polymer Science* **2002**, *280*, 400.

[166] M. J. Fevola, R. D. Hester, C. L. McCormick, *Journal of Polymer Science Part a: Polymer Chemistry* **2003**, *41*, 560.

[167] P. J. Flory, J. Rehner, *The Journal of Chemical Physics* **1943**, *11*, 512.

[168] E. Geissler, A. M. Hecht, *Macromolecules* **1981**, *14*, 185.

[169] A. M. Oelker, S. M. Morey, L. G. Griffith, P. T. Hammond, *Soft Matter* **2012**, *8*, 10887.

[170] N. Ishida, M. Kobayashi, *Journal of Colloid and Interface Science* **2006**, *297*, 513.

[171] M. J. N. Junk, R. Berger, U. Jonas, *Langmuir* **2010**, *26*, 7262.

[172] M. C. LeMieux, S. Peleshanko, K. D. Anderson, V. V. Tsukruk, *Langmuir* **2007**, *23*, 265.

[173] I. B. Malham, L. Bureau, *Langmuir* **2010**, *26*, 4762.

[174] E. Svetushkina, N. Puretskiy, L. Ionov, M. Stamm, A. Synytska, *Soft Matter* **2011**, *7*, 5691.

[175] J. Horsch, P. Wilke, M. Pretzler, M. Seuss, I. Melnyk, D. Remmler, A. Fery, A. Rompel, H. G. Börner, *Angewandte Chemie* **2018**, *130*, 15954.

[176] J. Horsch, P. Wilke, M. Pretzler, M. Seuss, I. Melnyk, D. Remmler, A. Fery, A. Rompel, H. G. Börner, *Angewandte Chemie International Edition* **2018**, *57*, 15728.

[177] P. Wilke, N. Helfricht, A. Mark, G. Papastavrou, D. Faivre, H. G. Börner, *Journal of the American Chemical Society* **2014**, *136*, 12667.

[178] Q. Wei, K. Achazi, H. Liebe, A. Schulz, P.-L. M. Noeske, I. Grunwald, R. Haag, *Angewandte Chemie International Edition* **2014**, *53*, 11650.

[179] H. Woehlk, J. Steinkoenig, C. Lang, L. Michalek, V. Trouillet, P. Krolla, A. S. Goldmann, L. Barner, J. P. Blinco, C. Barner-Kowollik, K. E. Fairfull-Smith, *Langmuir* **2018**, *34*, 3264.

[180] E. Faure, C. Falentin-Daudré, C. Jérôme, J. Lyskawa, D. Fournier, P. Woisel, C. Detrembleur, *Progress in Polymer Science.* **2013**, *38*, 236.

[181] B. P. Lee, J. L. Dalsin, P. B. Messersmith, *Biomacromolecules* **2002**, *3*, 1038.

[182] P. Wilke, H. G. Börner, *ACS Macro Letters* **2012**, *1*, 871.

[183] A. Lampel, S. A. McPhee, H.-A. Park, G. G. Scott, S. Humagain, D. R. Hekstra, B. Yoo, P. W. Frederix, R. R. Abzalimov, S. G. Greenbaum, *Science* **2017**, *356*, 1064.

[184] D. S. Hwang, H. Zeng, Q. Lu, J. Israelachvili, J. H. Waite, *Soft Matter* **2012**, *8*, 5640.

[185] Q. Lu, D. S. Hwang, Y. Liu, H. Zeng, *Biomaterials* **2012**, *33*, 1903.

[186] Q. Lu, D. X. Oh, Y. Lee, Y. Jho, D. S. Hwang, H. Zeng, *Angewandte Chemie International Edition* **2013**, *52*, 3944.

[187] J. H. Waite, *Comparative Biochemistry and Physiology – Part B* **1990**, *97*, 19.

[188] M. J. Harrington, A. Masic, N. Holten-Andersen, J. H. Waite, P. Fratzl, *Science* **2010**, *328*, 216.

[189] L. M. McDowell, L. A. Burzio, J. H. Waite, J. Schaefer, *The Journal of Biological Chemistry* **1999**, *274*, 20293.

[190] L. V. Zuccarello, *Tissue Cell* **1981**, *13*, 701.

[191] T. Kato, S. Ito, K. Fujita, *Biochimica et Biophysica Acta* **1986**, *881*, 415.

[192] D. C. S. Tse, R. L. McCreery, R. N. Adams, *Journal of Medicinal Chemistry* **1976**, *19*, 37.

[193] H. Zhao, J. H. Waite, *Biochemistry* **2005**, *44*, 15915.

[194] H. Zhao, J. H. Waite, *The Journal of Biological Chemistry* **2006**, *281*, 26150.

[195] J. H. Waite, *The Journal of Biological Chemistry* **1983**, *258*, 2911.

[196] M. Pretzler, A. Bijelic, A. Rompel, *Scientific Reports* **2017**, *7*, 1810.

[197] A. Flurkey, J. Cooksey, A. Reddy, K. Spoonmore, A. Rescigno, J. Inlow, W. H. Flurkey, *Journal of Agricultural and Food Chemistry* **2008**, *56*, 4760.

[198] S. G. Mauracher, C. Molitor, C. Michael, M. Kragl, A. Rizzi, A. Rompel, *Phytochemistry* **2014**, *99*, 14.

[199] T. S. Fischer, J. Steinkoenig, H. Woehlk, J. P. Blinco, K. Fairfull-Smith, C. Barner-Kowollik, *Polymer Chemistry* **2017**, *8*, 5269.

[200] S. C. Nicklisch, J. E. Spahn, H. Zhou, C. M. Gruian, J. H. Waite, *Biochemistry* **2016**, *55*, 2022.

[201] M. V. Voinova, M. Rodahl, M. Jonson, B. Kasemo, *Physica Scripta* **1999**, *59*, 391.

[202] G. Sauerbrey, *Zeitschrift für physik* **1959**, *155*, 206.

[203] F. Höök, B. Kasemo, T. Nylander, C. Fant, K. Sott, H. Elwing, *Analytical Chemistry* **2001**, *73*, 5796.

[204] Q. Lin, D. Gourdon, C. Sun, N. Holten-Andersen, T. H. Anderson, J. H. Waite, J. N. Israelachvili, *Proceedings oft he National Academy of Sciences of the USA* **2007**, *104*, 3782.

[205] Q. Lu, E. Danner, J. H. Waite, J. N. Israelachvili, H. Zeng, D. S. Hwang, *Journal of The Royal Society Interface* **2013**, *10*, 20120759.

[206] J. Yu, Y. Kan, M. Rapp, E. Danner, W. Wei, S. Das, D. R. Miller, Y. Chen, J. H. Waite, J. N. Israelachvili, *Proceedings oft he National Academy of Sciences of the USA* **2013**, *110*, 15680.

[207] W. Skoneczny, M. Niedźwiedź, M. Bara, *Applied Sciences* **2018**, *8*, 2251.

[208] P. B. Kowalczuk, C. Akkaya, M. Ergun, M. Janicki, O. Sahbaz, J. Drzymala, *Physicochemical Problems of Mineral Processing* **2017**, *53*.

[209] M. G. Kibria, F. Zhang, T. H. Lee, M. J. Kim, M. M. R. Howlader, *Nanotechnology* **2010**, *21*, 134011.

[210] M. Stöter, S. Gödrich, P. Feicht, S. Rosenfeldt, H. Thurn, J. W. Neubauer, M. Seuss, P. Lindner, H. Kalo, M. Möller, *Angewandte Chemie* **2016**, *128*, 7524.

[211] P. Feicht, R. Siegel, H. Thurn, J. W. Neubauer, M. Seuss, T. Szabó, A. V. Talyzin, C. E. Halbig, S. Eigler, D. A. Kunz, A. Fery, G. Papastavrou, J. Senker, J. Breu, *Carbon* **2017**, *114*, 700.

[212] L. Peng, S. Jiang, M. Seuß, A. Fery, G. Lang, T. Scheibel, S. Agarwal, *Macromolecular Materials and Engineering* **2016**, *301*, 48.

[213] A. M. Steiner, M. Mayer, M. Seuss, S. Nikolov, K. D. Harris, A. Alexeev, C. Kuttner, T. A. F. König, A. Fery, *ACS Nano* **2017**, *11*, 8871.

[214] N. T. Nguyen, A. H. Milani, J. Jennings, D. J. Adlam, A. J. Freemont, J. A. Hoyland, B. R. Saunders, *Nanoscale* **2019**, *11*, 7921.

[215] S. Ida, T. Kawahara, H. Kawabata, T. Ishikawa, Y. Hirokawa, *Gels* **2018**, *4*, 22.

Erklärung & Versicherung

Hiermit versichere ich, dass ich die vorliegende Arbeit ohne unzulässige Hilfe Dritter und ohne Benutzung anderer als der angegebenen Hilfsmittel angefertigt habe; die aus fremden Quellen direkt oder indirekt übernommenen Gedanken sind als solche kenntlich gemacht. Die Arbeit wurde bisher weder im Inland noch im Ausland in gleicher oder ähnlicher Form einer anderen Prüfungsbehörde vorgelegt.

Die vorliegende Arbeit wurde von September 2015 bis August 2019 am Leibniz-Institut für Polymerforschung Dresden e.V. unter der Betreuung von Prof. Dr. Andreas Fery (Betreuender Hochschullehrer) durchgeführt.

Dresden, den

Maximilian Seuß